On the Study of Surrogate-based Optimization Methods in Aircraft Conceptual Design

by

Martin Sohst
B.Sc., Technical University of Munich, 2015
M.Sc., Technical University of Munich, 2018

A Dissertation Submitted in Partial Fulfillment of the
Requirements for the Degree of

DOCTOR OF PHILOSOPHY

in the Department of Mechanical Engineering

© Martin Sohst, 2022
University of Victoria

All rights reserved. This dissertation may not be reproduced in whole or in part, by photocopying or other means, without the permission of the author.

On the Study of Surrogate-based Optimization Methods in Aircraft Conceptual Design

by

Martin Sohst
B.Sc., Technical University of Munich, 2015
M.Sc., Technical University of Munich, 2018

Supervisory Committee

Dr. A. Suleman, Co-Supervisor
(Department of Mechanical Engineering)

Dr. C. Crawford, Co-Supervisor
(Department of Mechanical Engineering)

Dr. A. Babul, Outside Member
(Department of Physics and Astronomy)

ABSTRACT

The goal of "greener" aviation is one of the main challenges in aircraft design. The target of Europeans "Flightpath 2050" and IATA is to reduced the net aviation CO_2 emission by 75% relative to 2000 and 50% relative to 2005, respectively. Novel unconventional aircraft claim to increase the efficiency and reduce the environmental impact. Designs differing from the conventional tube-low-wing concept are investigated regarding their performance benefit. The employment of a high aspect ratio wing is an effective way to increase the aerodynamic efficiency.

However, the long and slender wing structure is more flexible and thus more prone to aeroelastic effects. Critical phenomena, such as flutter and limit-cycle oscillation are more likely to drive the design. Therefore it is important to assess the interdependence of aerodynamic and structural forces. The effects of the wings flexibility can affect the design and off-design performance, possibly jeopardizing the intended efficiency benefit.

To evaluate the different disciplines involved in aircraft design, a multi-disciplinary design optimization environment offers the required tools. While computationally demanding, the obtained solution is more efficient if the disciplines are assessed simultaneously. Equipped with low- and high-fidelity assessments, aircraft performance can be predicted at the preliminary design stage, while mitigating some computational expenses.

To further reduce the computational burden, adaptive surrogate modelling approaches can be employed, requiring less computational evaluations while efficiently guiding the optimization process towards improved designs. Considering surrogate models for expensive physics based objective and constraint functions bears the disadvantage of more uncertainty in the models. Thus, a new technique is proposed to utilizing the probability of feasibility for the constraints in combination with a transformed normalized objective function to address the uncertainty consideration. The approach is assessed via mathematical test functions and an engineering application and compared against established methods. The results suggests an applicability of the method, with further improvements to be examined. Limitations are revealed regarding local optima and convergence. Further, the degree of maturity does not yet suffice for industrial applications.

In a multi-disciplinary design optimization of a high aspect ratio wing aircraft and a strut braced wing aircraft a more classical EGO approach was therefore the choice

of approach. The configurations were optimized towards a multi-objective, blending manufacturing and operational costs. Towards cost efficient evaluations, investigations were performed to incorporate high-fidelity assessments, yet limiting their number by reducing active constraints. Driven by aero-structural and aeroelastic constraints, the novel designs could improve the performance satisfactory.

Table of Contents

List of Tables

List of Figures

Nomenclature

The following list describes several abbreviations and symbols that are used within the body of the document. Parameter and symbols appearing once or in a limited context are not listed here and described in the respective paragraphs and context.

Abbreviations

AoA	Angle of attack
AR	Aspect ratio
CFD	Computational fluid dynamics
DLM	Doublet lattice method
DoE	Design of Experiments
DS	Dive speed
DV	Design variable
EBM	Equivalent beam model
FM	Flutter margin
FS	Flutter speed
FSI	Fluid-structure interaction
HARW	High aspect ratio wing
HF	High-fidelity
L/D	Lift-over-drag ratio
LF	Low-fidelity
MAC	Mean aerodynamic chord
MDA	Multi-disciplinary design analysis
MDO	Multi-disciplinary design optimization
MTOW	Maximum take-off weight
MTOM	Maximum take-off mass
OFPF	Objective function probability of feasibility
PFCON	Probability of feasibility constraint

PM	Panel method
RANS	Reynolds-averaged Navier-Stokes
SBO	Surrogate-based optimization
SBW	Strut-braced wing
SF	Safety factor
UTB	Upper trust bound
XDSM	Extended design structure matrix

Symbols

C_D	Drag coefficient
C_L	Lift coefficient
C_p	Pressure coefficient
$E[I]$	Expected Improvement
f	Generic function
$\hat{f}$	Generic function surrogate
g	Generic inequality constraint
$\hat{g}$	Generic inequality constraint surrogate
$P[F]$	Probability of Feasibility
$P[I]$	Probability of Improvement
y	Function response
$\hat{y}$	Predicted function response

ACKNOWLEDGEMENTS

First and foremost, I would like to thank my supervisor, Professor Suleman for his invaluable advice and continued support throughout this work. I would also like to thank Dr. Curran Crawford for his assistance and insights.

This thesis research was performed under the NSERC Collaborative Research and Development MIDAS project in partnership with Bombardier Aerospace. The insights and knowledge shared by Graham Potter and Sid Banerjee during our frequent discussions are acknowledged.

My special thanks goes to Dr. José Lobo Do Vale and Dr. Frederico Afonso for their guidance, thoughtful comments, patience, immense knowledge and encouraging words.

To the committee members, I want to express my gratitude for their time and effort to evaluate my work.

I thank my fellow colleagues and friends at CfAR for the stimulating discussions and for all the fun we have had in the last four years.

Last but not least, I would like to thank my family: my parents and my sister for supporting me spiritually throughout writing this thesis and my life in general.

DEDICATION

To my loving parents!

Chapter 1

Introduction

Despite the drop in air traffic due to the Covid-19 pandemic, passengers and cargo transportation by air is expected not only to recover but also increase within the next decades [1]. A recovery of the aviation industry after the grounding of aircraft is already visible in the statistical data, for instance the domestic flight passengers in the U.S., as seen in Fig. 1.1.

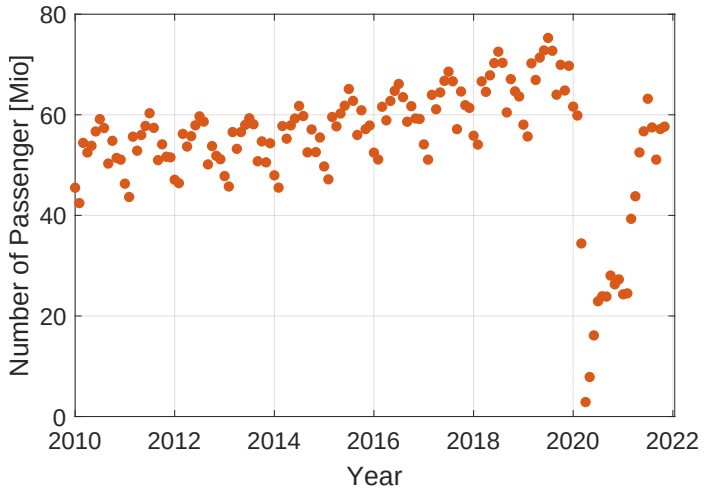

Figure 1.1: Monthly number of passengers on domestic flights within the U.S. according to TSA[1,2]

Studies from 2011 predicted an increase in the passenger volume within the next decades [2; 3] and it is anticipated that air traffic will likely grow in this direction. Therefore, air travel and transportation will have an ongoing influential role in the

[1] `https://www.transtats.bts.gov/Data_Elements.aspx?Data=1`, accessed: Dec. 1^{st} 2021
[2] `https://www.tsa.gov/coronavirus/passenger-throughput`, accessed: Dec. 1^{st} 2021

global community.

This increase in air traffic poses a challenge, as at the same time a declared goal is the "zero net emission" policy to reduce emissions in the fight against climate change. To reduce the carbon footprint of aviation, the demand for greener more environmental friendly aircraft increases. To comply with regulations to fulfill the goal of emission reduction, aircraft manufacturers endeavor to develop ways of increasing the efficiency of aircraft. Accomplishing this goal the improvement of different disciplines is necessary. Those are, for instance, efficiency improvement of propulsion systems [4; 5; 6; 7], with considerations of electrification [8] and distributed propulsion [9; 10; 11]. The implementation of advanced flight traffic control [12; 13], mission and trajectory optimization [14; 15; 16], efficient turnaround times [17; 18] can improve on-ground efficiency. The use of advanced materials for weight reduction [19; 20; 21], or improvement of aerodynamic efficiency [22; 23] support the in-flight performance improvement. However, developing aircraft and integrating those different disciplines is a complex matter.

To tackle the challenge of a drastic increase in efficiency, novel configurations are being proposed and investigated. To achieve more sustainable aviation, these novel designs are required since conventional concepts are optimized and have reached a state where further improvement is expensive to accomplish and steep rise in efficiency is not expected [22]. Some advanced concepts improve the aerodynamic efficiency with the use of higher wing aspect ratios, for instance High Aspect Ratio Wing (HARW), Strut-Braced Wing (SBW) or joined wing aircraft. The longer and slenderer wings reduce the induced drag and therefore increase aerodynamic efficiency. Non-planar wing designs increase the aspect ratio of the wing, while at the same time maintain the wing span to comply with regulatory constraints like airport size or vehicle categorization. Blended wing bodies or flying wing concepts break with the conventional tube-wing design, incorporating a blend of the fuselage and the lifting system. With their lift generating bodies they reduce the lift requirements for the wings, reducing the vortex strength at the wing tip and consequently the induced drag. Furthermore, the integration of other advanced systems promises further increase in efficiency, for instance boundary layer ingestion [24], morphing wings [25; 26], or laminar flow airfoils [22; 27].

An issue with elongated wings is their aeroelastic behaviour, as the response has more influence and aircraft are more prone to experiencing aeroelastic phenomena. The mutual interaction between aerodynamics and the structure of flexible wings

plays an important role for HARW. Aeroelastic issues of static or dynamic nature, such as divergence or flutter, occur at lower speeds compared to equally sized lower aspect ratio wings [28; 29]. Furthermore, the flexibility of high aspect ratio wings might influence the performance of the aircraft within the flight envelope. Longer wings entail an increased root bending moment, requiring reinforcements of the wing root structure, neutralizing the benefit of the aerodynamic gain by increasing the weight. Another aspect of very flexible wings is their deformation behaviour. High displacements can cause geometric non-linear effects, influencing the performance in a more distinct way, making it necessary to consider it early on in the design process. The change in natural frequencies due to the displacements can effect the dynamic behaviour of the aircraft. Better understanding and knowledge about aerodynamic and structural phenomena and interaction allows for further optimization of aircraft. Thus, it is of paramount importance when designing novel configurations to account for all main disciplines and their coupling (including aeroelasticity) in a multidisciplinary design optimization approach. However, the need for more complex models raise the computational costs, hence iterations in the preliminary design stage become more costly and prolong the process. Considering the diverse disciplines requires the employment of advanced tools and processes.

For handling the increasing complexity of aircraft and their optimization, a multidisciplinary design optimization (MDO) environment offers the tools to integrate the different disciplines involved [30]. To couple the aero-structural problem a fluid-structure-interaction (FSI) tool can be employed to solve the multi-disciplinary problem. The deformation of a loaded structure and the corresponding shape are obtained together with the aerodynamic coefficients. The computational tools for each discipline can be combined with different fidelities to obtain the desired level of precision in the available time frame. Aerodynamic models range from fast and simple lifting line methods to 3-dimensional (3D) panel methods up to Reynold-Averaged Navier-Stokes (RANS) flow solutions. Further, optimizing designs at early stages with higher detail is desirable, to prevent costly adjustments at later stages in the design process. However, the use of high-fidelity tools is associated with high computational expenses. Therefore, efficient optimization methods play a key role in preliminary aircraft design.

Thus, ways are sought of to efficiently manage the expensive evaluations in an effort to find an improved, satisfying or optimal solution. A widely applied approach is the use of surrogate models, also called meta- or response surface models. Instead of evaluating the expensive real function, a prior built mathematical model is used

to estimate the response. A surrogate is less costly to evaluate but able to provide a similar insight into the overall behavior. As a surrogate is based on a limited number of evaluated inputs, an error between the predicted and real function is present. Continuously updating the model and rebuilding it can support a more precise model. This adaptive behaviour is desirable especially in design areas of interest where an optimal solution is likely to be found. Costly procedure of MDO can be tackled with a surrogate based optimization (SBO), where mathematical models are used to reduce the number of costly evaluations.

Covering the different aspects of this work, a comprehensive literature review is presented next. It includes the topics of novel aircraft design, aeroelastic considerations for aircraft with long and slender wings, and SBO considering MDO.

1.1 Novel Aircraft Configurations

To achieve more sustainable aviation, novel and unconventional design are necessary as over the last decades conventional concepts were optimized and reached a state where further improvement is expensive to accomplish and steep rise is not expected [22].

The design of conventional passengers aircraft as constructed nowadays dates back to the 1950s where the concept of passenger jet aircraft were introduced through de Havilland Comet, Boeing 707, and Douglas DC-8. To deal with the challenges of developing environmentally friendly aircraft, the existing designs should be modified. In the following decades further developments led to more comfortable and faster jetliners. The increasing demand for cheaper flights and lower cost of operation accentuated the critical role of efficient aircraft to airlines. Thus, the demand for lower fuel consumption, less emissions and in overall a more sustainable operation is perpetual. Furthermore, Schmidt et al. [17] discuss the additional challenges that future sustainable aircraft configurations might face in terms of operation and facilities, which should also adapt. In the following section, an overview of various designs is given, with some of their respective benefits and challenges.

High Aspect Ratio Wing Aircraft

The increase of the wing aspect ratio reduces the induced drag [31]. Consequently, a higher lift to drag ratio for the same aircraft weight is achieved and therefore a

reduction in fuel consumption. Aircraft that rely on low drag for energy efficiency or long endurance employ this benefit. This includes gliders as well as medium- or long-endurance high-altitude aircraft, so called MALE and HALE [32; 33], respectively, for reconnaissance or surveillance. Also, HARWs become a trend in aircraft design for commercial airliner [34; 35]. For instance, recent aircraft from Airbus (A350) and Boeing (B787) have a higher wing aspect-ratio than their predecessors. Likewise, there is an interest in increasing the aspect ratio of medium haul and regional jets for better fuel efficiency, for example the DHC-8 or ATR 72. Fig. 1.2 shows an exemplary conventional aircraft with a larger aspect ratio compared to operating aircraft.

Figure 1.2: A high aspect ratio wing aircraft with an elongated main wing

Due to the increase in aerodynamic efficiency, novel "green" aircraft are likely to incorporate long and slender wings. Research of aerodynamic shape optimizations to extend the aspect ratio show a high potential for efficiency improvement [36].

However, the increase in flexibility poses new challenges as aeroelastic phenomena need to be considered and are harder to predict in a cost efficient way. Deformations at design and off-design flight conditions influence the performance. Further, aeroelastic phenomena dependent on airspeed are a challenge and ongoing field of research. Namely those that may arise from the dynamic interaction between airflow and structure, for instance divergence, flutter or limited cycle oscillation. Low subsonic aircraft are less prone to be influenced by aeroelastic effects in a negative way. Yet, structural issues due to the flexibility may occur at a lower airspeed than in a conventional design once the wing's structure is projected to be the lightest possible. The slender structure causes higher root bending moment, requiring reinforcements for stress alleviation. In turn, the necessary structural mass increases, antagonizing the aerodynamic benefit [37]. Furthermore, effects of nonlinear nature might occur for flexible wings under

larger deformations [32; 38; 39; 40].

Thus, a considerable effort is being dedicated to analyze the aeroelastic behavior, specially at transonic conditions [41], as modern commercial transport aircraft operate in this flight regime. The optimization of HARWs accounting for these issues is an ongoing objective in aircraft design [42].

The use of wing tip devices (such as winglets) increase the aspect ratio, while at the same time respecting limitations in span. Other solution sought of are hinged wing tips to reduce the induced drag, with additional gust load alleviation [43; 44; 45].

Strut- and Truss-braced Wing Concepts

A configuration that experiences a recent revival in research is the Strut- or Truss-braced wing aircraft (SBW/TBW). The former is characterized by a strut, connecting the wing at a location along the span with the fuselage. The TBW is distinguished by additional jury struts, that additionally link the wing and the strut for added structural stiffness. Equipped with this (usually) non-lifting support structure for the wing, it is categorized as a joined wing concept [46].

The strut alleviates the structural load and allows for a lower main wing weight with a higher span at the same time. Therefore, a main wing with an increased AR can be employed, increasing the aerodynamic efficiency of the design. However, the strut increases the wetted area, requiring a careful design of the overall concept to not jeopardizing the aerodynamic benefit of the lower induced drag. Further, the additional weight of the strut causes the whole wing structure to be heavier and as well needs to be carefully designed. A generic representation of a SBW is depicted in Fig. 1.3.

While the first idea for a transonic TBW passenger aircraft dates back to the 1950s to a concept by Pfennigers [47; 48], recent projects investigated similar designs due to its possible increase in efficiency. Cavallaro and Demasi [46] surveyed many aspects and projects of SBW and TBW in their review, including the early works from NASA, Virginia Polytech and Lockheed Martin [49; 50], and the SUGAR project by Boeing [51; 52; 53]. The anticipated gain for block fuel benefit for a novel SBW ranges from 5% to 30%. This is achieved by its predicted aerodynamic benefit as well as additional improvements related to novel aircraft, for instance improved propulsion, laminar flow control, or air traffic management.

Figure 1.3: A strut-braced wing concept with a high wing and a supporting strut structure

Based on the research of the SBW by Virginia Polytech, the concept was extended and investigated as TBW design [54; 55]. Yet, many investigations are ongoing, focusing on the aerodynamic peculiarities [56; 57], interference drag at the joint and shape of the strut [58; 59], flutter and divergence properties [60; 61], transonic corrections [58; 59], flight dynamics [62] or overall MDO [63; 57]. Still, open topics for this configuration are, for instance, more detailed studies of laminar flow wing and interference effects as well as optimization at transonic Mach numbers to contend current conventional designs.

Alternative High Aspect Ratio Wing Concepts

The use of winglets is a common way to extend the aspect ratio of wings while at the same time complying with the span restrictions. Extending a wing tip device and folding it to a C-section (as seen in Fig. 1.4(a)) leads to more complex non-planar configurations [64; 65].

(a) C-Wing design (b) Box-Wing design (c) Joined Wing design

Figure 1.4: Non-planar wing concepts to increase the effective wing aspect ratio while simultaneously respecting span limitations

The aspect ratio is further increased while span and height limits are retained. Additional interference drag can penalize the benefit and the structure is almost as heavy as for a straight wing due to the reinforcement. Hinged wing tips, as mentioned before, can be actively controlled to fold during ground operation and unfold in flight for improved performance. A similar idea is the basis for morphing wing with wing tip extension [66; 44].

Other non-planar wing concepts that increase the aspect ratio are box wings and joined wings, also named Prandtl plane [67], depicted in Figures 1.4(b) and 1.4(c). The box wing has visual similarities with a biplane, where the wing tips are connected to reduce the induced drag. A joined wing design connects the main wing with the vertical control surface.

Blended Wing Bodies and Flying Wings

Other unconventional concepts are Blended wing bodies (BWB), hybrid wing bodies and flying wings. The idea for a BWB was first investigated in the early 2000s and continued to be an object of research further on [68; 69; 70]. They can be characterized by a smooth blending between the passenger cabin or transport volume and the lifting surfaces. Due to the smooth transition and the shape of their fuselage, they have an aerodynamic advantage over conventional tube-wing aircraft as the fuselage is used a a lift generator, therefore reducing the lift portion of the wings and consequently the vortex strength at the wing tips. Fig. 1.5 shows exemplary designs of a blended wing body (1.5(a)) and a flying wing (1.5(b)).

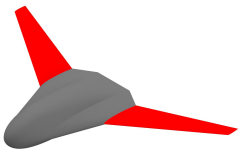

(a) Blended Wing Body with wide lifting fuselage

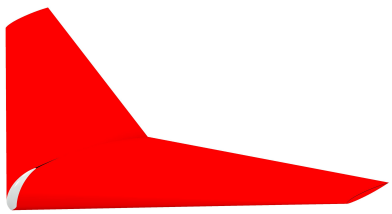

(b) Flying wing design without a dedicated fuselage and integrated transport volume

Figure 1.5: Blended Wing Body and Flying Wing design are unconventional concepts to increase aerodynamic efficiency

For the BWB concepts, the stated advantages are related to better aerodynamic efficiency, noise shielding, propulsion integration and internal volume [71; 72; 73; 74; 75]. Investigations included structural layout and analysis [76; 77; 78; 79], experimental [80; 81; 82], and computational work [83; 84]. A Comprehensive review on the current state and claimed potential is given by Okonkwo and Smith [85], and Chen et al. [86] provided a review on the progress and ongoing challenges of BWB aircraft.

The latter include aspects related to non-existent historical data, therefore lacking the availability of a general and fast conceptual design method. Further, a possible issue is seen in the public acceptance, as the layout changes drastically compared to the conventional tube-wing design. The non-cylindrical fuselage poses challenges for the structural layout, requiring additional reinforcements to withstand bending and stress. Also, the integration of subsystems leads to a larger weight for a similar sized design.

Notable Unconventional Designs

For the sake of completeness, configurations to mention are the D8 "Double Bubble" and the Flying-V concept, shown in Fig. 1.6(a) and Fig. 1.6(b), respectively.

(a) D8 "Double bubble" concept, adapted from [87]

(b) Flying-V concept, adapted from [88]

Figure 1.6: Other proposed unconventional designs with initial conducted investigations for increasing aerodynamic efficiency

The first concept was presented by Drela [87] in the context of NASA's N+3 call for novel aircraft [89] and shows a promising reduction in fuel burn throughout preliminary studies. This design consists of two fuselages wrapped in an air frame ("Double Bubble") capable of generating some lift. Additionally, it is sought of with an advanced propulsion system, enabling boundary layer ingestion technology on the rear part, with engines integrated in the fuselage. Synergistic effects of the improved

fuselage with aforementioned high aspect ratio wings advances may lead to further efficiency improvements. Investigations were conducted regarding fuel benefits [90] stability and structural design [91], noise [92] and aeroelastic behaviour [93].

The second mentioned concept, the "Flying-V", was introduced by TU Delft [88]. The two tubular fuselage compartments are arranged in a "V"-shape and act as lift generating bodies. Experimental tests regarding aerodynamic characteristics and system identification with a scaled model [94; 95] were performed as well as investigation about engine placement respecting aerodynamic advantages [96].

Similar to the BWB concepts, the challenges for such unconventional concepts are related to stability and control, public acceptance and regulations, as many aspects are in a preliminary stage. However, this kind of change is expected to be necessary to tackle the challenges in future air travel.

1.2 Aeroelasticity

Aeroelasticity is the mutual interaction between aerodynamic, elastic and inertial forces [97]. Collar classified the type of forces in a triangle as pictured in Fig. 1.7 and located aeroelastic phenomena according to the involved kind of forces. In a

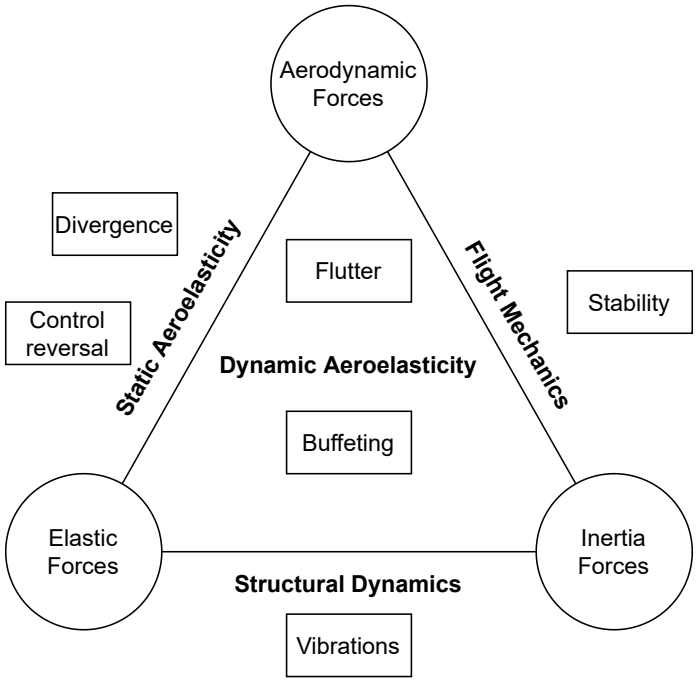

Figure 1.7: Collar's triangle of forces for aeroelasticity (adapted from [97])

broader sense aeroelasticity can be divided into two categories, steady and unsteady [98; 99; 100; 101]. The latter includes all three forces, aerodynamic, structural, and inertial, in Collar's triangle, while the former is the interaction between aerodynamics and structure. The different aeroelastic phenomena can then be located around the triangle.

1.2.1 Steady Aeroelasticity

In static aeroelasticity, the interaction occurs between aerodynamic and elastic forces. Aerodynamic forces along the wing cause a deformation of the structure, which in turn changes the shape of the wing and therefore the aerodynamic forces. Two main static aeroelastic issues can be identified, divergence and control reversal [99; 101].

Divergence is a static instability that eventually results in structural failure of the wing. Fig. 1.8(a) visualizes this case. The Aerodynamic force due to the airspeed generates a moment around the elastic axis, being opposed by a restoring elastic force of the wing structure. With increasing speed and therefore increasing aerodynamic force, the elastic moment is too small, which leads to further deformation and the structural failure of the wing. The speed at which this phenomenon occurs is the divergence speed. It is dependent on geometric factors like wing sweep, distance of elastic axis and aerodynamic center.

The aeroelastic response of the wing (twist) actuating a control surface causes a counter moment of the wing, reducing the effectiveness, as seen in the graph in Fig. 1.8(b). This will reach a point, speed dependent, when the control surface has no actual effect anymore and therefore jeopardizes the maneuverability of the aircraft. The speed at which the effectiveness reaches zero is the control reversal speed.

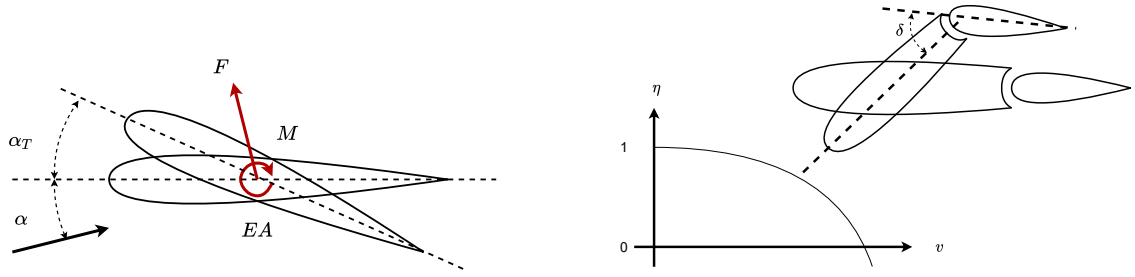

(a) Divergence

(b) Speed (v) dependent control effectiveness (η)

Figure 1.8: Steady aeroelastic phenomena

1.2.2 Unsteady Aeroelasticity

Dynamic aeroelasticity is the interaction between all three types of forces in Collar's triangle, where aerodynamics, elasticity and inertia are involved. Important phenomena are flutter, buffeting, limit cycle oscillation and flexible aeroelastic response.

Buffeting describes the effect of flow-induced vibrations, qualified as a global instability and caused by interactions of boundary layer separation and shock motion [102; 103]. The phenomenon plays a role for aeronautical and aerospace design and in the scope of recent research to better understand and model it [41]. In aircraft, it appears on the wing as well as the fuselage, where it can be felt by passengers as bothersome vibrations but can also cause catastrophic separation [104], namely shock buffet.

LCO is closely related to flutter and usually appers as a response to a disturbance beyond the flutter speed [100; 99]. In the non-linear case it can appear below the flutter boundary if the dirsturbance is large enough [99]. With linear aerodynamics, a predicted LCO is related to the flutter speed with an infinite amplitude at the latter. If a strongly non-linear behaviour is present and the LCO amplitude is dependent on the speed, non-linear aerodynamics are necessery to resolve the phenomenon [105; 106]

Flutter is one of the most important aeroelastic phenomena in aircraft design. There are different kinds of flutter, of which the one of most interest is the coalescence of two or more elastic or rigid body mode shapes [100]. During this self-exited oscillation, the structure extracts energy from the airflow around it and increases the oscillations until the structure breaks. An infamous example is the Tacoma bridge, which was collapsing shortly after its construction during strong winds. Its eigenfrequency was close to the wind gust frequency, resulting in self-excited flutter and the eventual destruction of the bridge [107]. In aircraft, there are as well some incidents caused by flutter phenomena, with the most recent one being NASA's Helios 2 HALE aircraft, which encountered strong winds during a mission that lead to structural failure of the flexible wings [108]. Different types of flutter can occur, with the most typical bending-torsion coupling, where a phase shift between the two modes increases the oscillation of a wing. Another type is the coupling between an elastic and a rigid body mode, for instance the short period. This so called body freedom flutter happens more often for flexible aircraft and such with high short period frequencies [109]. The safety and investigation of flutter for novel designs is an ongoing topic and of great interest. The use of computational models to estimate and predict the flutter behaviour of

novel aircraft continues to be researched [93; 42; 110]. A recent state of the art review regarding flutter, flutter suppression and related phenomena was done by Livne [109] and shows the continually importance of the topic.

1.2.3 Flexibility of Elongated Structures

Aircraft with long and slender wings are more flexible and, hence, more prone to aeroelastic phenomena. Considering the flexible response at design and off-design flight conditions is essential to obtain the aerodynamic shape and predict the performance to not jeopardizing the intended operation goals. It is therefore one of the key aspect in this work to investigate the influence of aeroelastic responses towards aircraft performance and optimization of novel aircraft designs.

The occurrence of high displacements in the wing can further lead to geometric non-linear behaviour, further influencing the performance of the aircraft. Initially being an issue for HALE aircraft, novel configurations with high aspect ratio wings can be possibly affected by this kind of non-linearities. To prevent an unwanted behavior and redesign in a later design phase, it is worth to consider non-linear aeroelastic effects in early design stages [111; 112; 29]. However, non-linearities make it more challenging, namely in terms of computational cost [42], as iterative numerical processes are necessary to determine the deformed shape. Nevertheless, non-linear aeroelasticity is seen as an important step towards novel aircraft design [113] and with the advance of computational resources available for affordable workstations, it will help understanding the phenomena and make it accessible in early design stages.

1.2.4 Computational Aeroelasticity

To obtain the aeroelastic solution of a flexible structure exposed to a flight condition a FSI evaluation can be utilized. FSI is a way to couple aerodynamic forces and structural displacements to computationally model and assess aeroelastic responses [114] and obtain aerodynamic coefficients of the deformed structure.

For a preliminary design study, fast evaluations and a broad exploration of the design space is desirable. Therefore, the computational cost of assessments plays an important role in the optimization process. Low-fidelity tools are used for fast computation with lower precision whereas high-fidelity tools are employed to obtain responses of necessary accuracy. Fig. 1.9 illustrates the difference in fidelity levels for aerodynamic assessments and shows the respective increase in computational

costs. Low-fidelity models are based on linear potential theory, where viscosity and

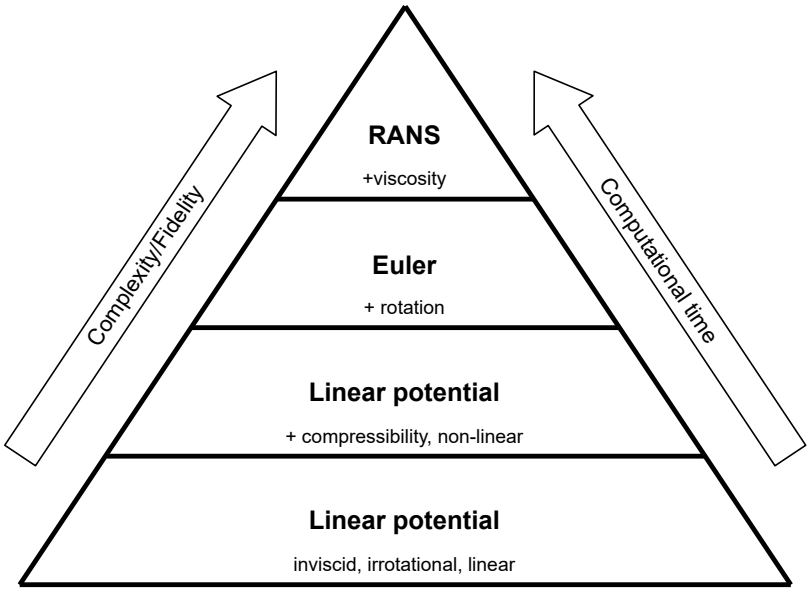

Figure 1.9: Levels of fidelity for fluid models (adapted from [115])

rotation are disregarded [116] and the wing is modelled as a lifting line or flat plate. Medium-fidelity linear potential models are capable of 3 dimensional modelling and the consideration of non-linearity and compressibility [117]. High-fidelity models can resolve more flow dynamics, with Euler considering rotations and Reynolds-Averaged Navier-Stokes (RANS) equation being able to model viscosity [118]. For structural assessments the same is valid for fidelity of tools. Computational structural dynamics (CSD)

However, the computational time for solving a RANS based system is orders of magnitudes higher than for a low-fidelity linear potential method. Dependent on the available computational power and the required accuracy, one has to find an adequate methodology out of the available tools.

To obtain an estimation for the flutter boundary, a calculation in the time domain [119] or in the frequency domain [120] can be performed. The p-k method is a method to assess the flutter speed in the frequency domain [121] and implemented into NASTRAN [122], a commonly used tool for dynamic and static analysis in the industry and academia. The doublet lattice method (DLM) used in NASTRAN is based on a linear aerodynamic model. To assess non-linear aerodynamics, one can correct the obtained pressure solution, as is done for experimental and computational models computed in the transonic speed regime [123].

1.3 Multi-disciplinary Design Optimization

To incorporate the various disciplines and aspects mentioned before, a multi-disciplinary design analysis and optimization (MDAO) environment provides the necessary tools [37]. Two or more disciplines, in aircraft design often aerodynamics and structure [124; 125; 126; 127], are coupled and optimized towards a common goal. The solution, aiming at maximizing an objective while respecting relevant constraints, is more efficient due to the integration of the different disciplines. Furthermore, it is desirable that the analysis methodology incorporates all important disciplines while predicting the important performance metrics with sufficient accuracy, in order to be able to effectively compare different designs [128; 124; 129]. In aeroelastic optimization, for instance, the considered flexiblility effects can drive the MDAO problem and tailor the wing shape and structure accordingly [130; 131; 132], while suppressing undesirable aeroelastic phenomena such as flutter [133; 134; 135; 136; 137; 138; 139; 140]. Therefore, the aforementioned FSI tools play an essential role in obtaining the deformed shape of a flexible structure [141; 14] and capturing the aeroelastic phenomena [114].

MDO applications have a wide range in engineering design, from mechatronic systems [142], electrical machines [143] energy systems [144], building in civil engineering [145], automotive design [146; 147], wind energy systems [148; 149] or aerospace design. For the latter, the applications range from sub-systems [26; 150] to full aircraft design [37; 42; 23] and continue to play an essential role in optimization for novel appliations [151].

Different architectures are available and can be used to solve the numerical optimization problem [30]. If a decomposition of the problem is possible, a distributed MDO can be employed. This allows for parallelization, making it computationally more efficient if the computational tools are available. In a monolithic architecture the problem is highly integrated and needs to be solved for all disciplines at the same time.

Fig. 1.10(a) visualizes an exemplary process for a multi-disciplinary problem, where the two interacting disciplines are dependent on each other and solved sequentially. One challenge for an MDO process can be the computational expenses of the single discipline tools used. While it is desirable to obtain information of high fidelity at an early stage in the design process, the computational time to do so prevents the extensive use of costly evaluations. Even though the employment of MDO tools is more efficient to obtain an improved solution [30], it is still a challenge.

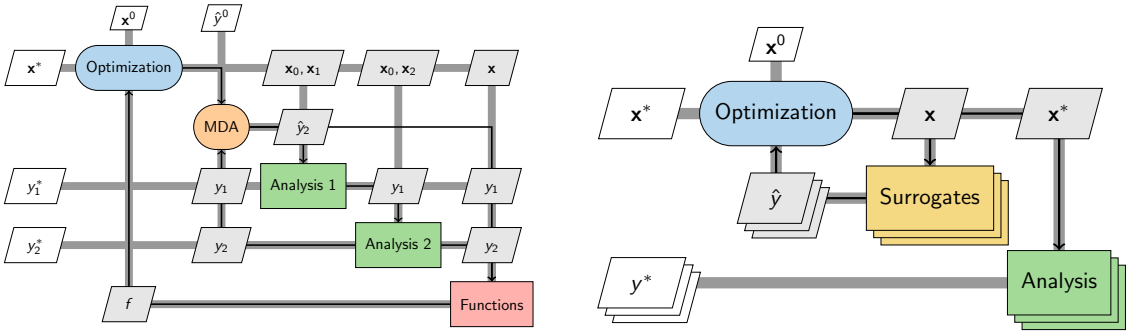

(a) Integration of solvers for different disciplines (for instance aerodynamic and structure)

(b) Use of surrogate models in a MDO environment

Figure 1.10: Architectures and integration of different disciplines to solve MDO problems (adapted from [30])

One solution is the use of surrogate models, where simplified data-fit models are used instead of the physics based evaluations. They can be incorporated into a MDO process to accelerate the procedure [84]. In Fig. 1.10(b) an optimization process is shown using surrogate models for the disciplines, which can be employed if the real functions are expensive to evaluate. When discussing the presented MDO in this work, it is shown in the same manner as the charts in Fig. 1.10 to help understanding the flow of the process.

The availability of tools of different fidelities, as mentioned beforehand for aerodynamic assessment tools, can help accelerating the process of evaluating computationally expensive calculations, such as in aerodynamic shape optimization [152; 153] or structural optimization [154]. These types of analysis, particularly high-fidelity CFD, can be time consuming and/or require significant computational resources to perform, which renders them inadequate for a typical gradient based or Genetic Algorithm (GA) [155] MDO procedure, where an extensive number of evaluations is required. Resorting to adjoint methods also requires significant setup time [30; 155; 156; 157].

[Following, the use of surrogate, or meta-models, is further discussed and explored.]

1.4 Surrogate-based Optimization

The evaluation of computational tools with high fidelity, such as computational fluid dynamics or computational solid mechanics, can be expensive, which is a challenge

in any optimization process, as computational resources are often limited [155]. A surrogate model serves the purpose to approximate the response of such expensive physics model evaluations and being used as a replacement[158; 159; 160], which for instance is necessary in an optimization process [161]. This approach can reduce the number of expensive function evaluations, if, for gradient-based optimization, additional function evaluations to compute sensitivities by means of finite differences would be required and the simulation code is not prepared to provide sensitivities by means of the adjoint method [126; 157]. It is also an alternative to non-gradient based methods, like a genetic algorithm, as they are computationally expensive. Surrogate models are also called meta-models, black-box models or response surface models in the literature [162; 155] and proofed themselves useful in combination with multi-search methods for solving high dimensional and multi-modality optimization problems [163]. Applications of surrogate-based optimization in the aeronautic field over the past decades are vast [161; 164; 155], especially when involving expensive CFD simulations of, for instance, airfoils [165; 166; 167; 168] or wings [165; 169; 14; 170] such as those required for Aerodynamic Shape Optimization.

1.4.1 Conventional Process of a Surrogate-based Optimization

The process of a surrogate based optimization (SBO) is visualized in Fig. 1.11. The procedure starts with the evaluation of the physics based model responses at a number of sample points to obtain an initial set of data. A surrogate model is built using the information of the sample points and their respective response. The optimizer searches within the surrogate model design space to obtain a minimum or maximum, depending on the objective. As the surrogate is cheap to evaluate, one can employ global (e.g. GA) or local optimizer (e.g. gradient-based, if the first derivative is continuous). When a new point is found based on its predicted value, the real response is evaluated.

As a new design (infill point) is determined based on the prediction of the surrogate, it is evaluated with the real functions to ensure the response and specify the differences between the predicted and the real value. If the discrepancies are large, one can deduce that the built surrogate lacks accuracy and needs to be improved by feeding more data and rebuilding the model. Depending on the purpose of the surrogate, precision is sought in areas of interest, henceforth accuracy can be an objective in local regions

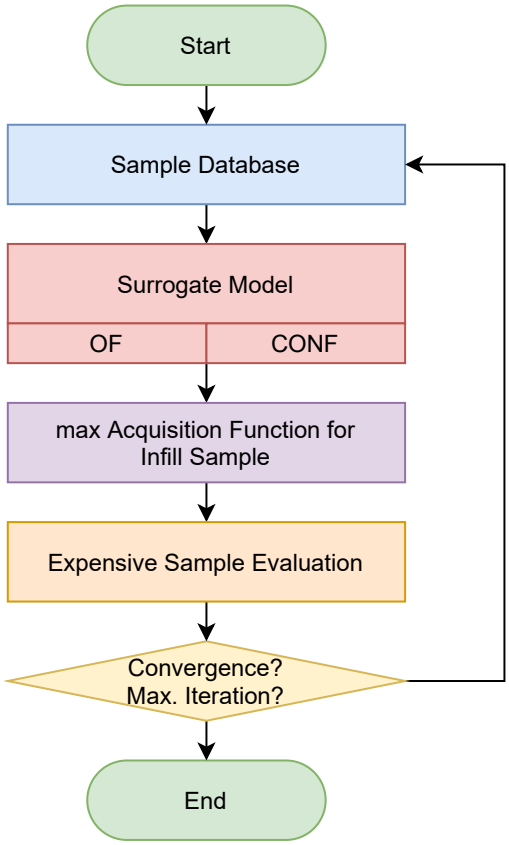

Figure 1.11: Overview of the surrogate modelling process

only. If the found design fulfills a termination criterion, the computational time is exhausted or a different convergence criterion is reached, the process is finished and the new sample point is the desired design. In the case the process is not terminated, the new sample point is added to the existing data base, and the process repeats with updated surrogates. The decision if the surrogates are built only once, in each iteration or with a specific frequency differentiates if an adaptive sampling strategy is used. In doing so, the process is accelerated, yet rebuilding the surrogate model each iteration can be computationally expensive [171].

1.4.2 Initial Sampling Process

Usually, a design of experiment is the base for a surrogate model, where the response of computer simulations are evaluated and taken for the generation of the mathematical model. A shortcoming of this strategy is the number of samples required for the surrogate model to accurately represent the response, which exponentially grows with

the number of design variables in the optimization, which is referred to as curse of dimensionality [162]. Requirements are posed for an initial sample to be used in surrogate based optimization. For one, it should be space filling, meaning that with the initial evaluations one wants to gain an idea about the design space and have an approximation about the global trend. Further, a small number of initial designs is desirable, as this is the purpose in the first place, a reduction of expensive evaluations. However, large Design of Experiments (DoE) are often required to build an accurate surrogate model [161], thus presenting a disadvantage in SBO. With the initial evaluations it is not guaranteed that the model is accurate, since at unsampled locations the difference between the real physics and the prediction can be large.

A way to encounter this issue is the sampling throughout the optimization process. In this adaptive sampling method new samples are added constantly and therefore help to improve the accuracy of the model on a local and global scale [155]. Therefore, the initial sampling can be kept small and an exploration and exploitation is performed during the process. Application of adaptive SBO in aerospace is a commonly used approach and actively conducted [166; 170; 172; 173]

To generate the initial data base, one can use different approaches. A randomly chosen sample, as shown in Fig. 1.12(a) is one option, to obtain the data to built the surrogate [174], yet it contains the risk that some regions are sampled sparsely, while other regions are sampled densely. Therefore, general trends can be unnoticed and information about whole regions is unavailable or inaccurate.

A full factorial sampling [174] places a mesh over the design area to apprehend the combination effects of the design variables on the objective. An example is visualized in Fig. 1.12(b). However, with increasing dimension of the design space, this approach becomes expensive, as all combinations of the design variables are covered. An associated sampling method is a fractional-factorial design [174], where only a portion of the full factorial samples is used, based on some selection criteria, and to reduce the cost.

To establish an initial data set that provides sufficient insight in the global behaviour of the function yet not being too extensive, a Latin-Hypercube sample can be chosen [175]. Each sample in the data set is the only one in its hyperplane, as shown in Fig. 1.12(c) for the two-dimensional case. Therefore it has a random distribution with space-filling properties and a limited number of evaluations.

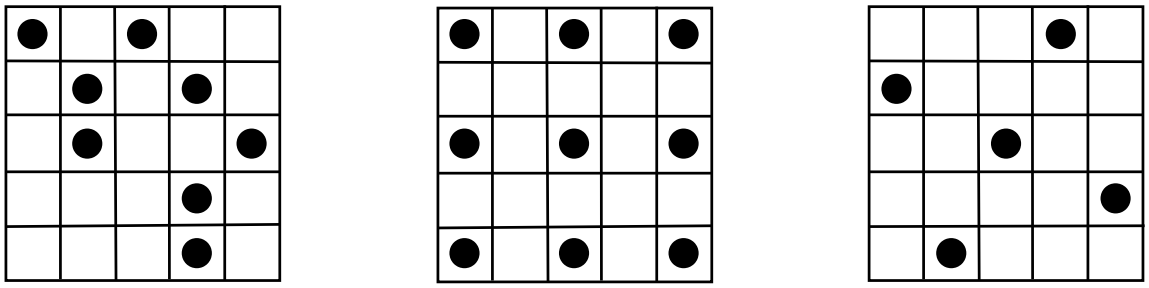

(a) Random sampling

(b) Full factorial sampling

(c) Latin Hypercube sampling

Figure 1.12: Sample plans for a DoE to built a 2D surrogate model

1.4.3 Types of Surrogate Models

With the existing data base the type of surrogate model can be chosen to built the mathematical approximation of the real function.

Polynomial regression is a common way to obtain the general trend of a response [176] and the cheapest surrogate to use for regressing data [155]. Low-order polynomials are suitable for obtaining a general trend and easy to built, usually with least square methods. However, their prediction capability for nonlinear or multi-modal functions is limited. Further, while high-order polynomials are capable of fitting data more closely locally, they are prone to instabilities [155]. Finding a suitable order for a polynomial regression can be done, for instance, via a cross-validation fit with a least square method [162]. Here, the error between prediction and real response is numerically minimized to fit the polynomial curve, while test points are excluded from the model.

Radial basis functions (RBF) use the spatial distribution of the sampled response in the data set and a linear combination of basis functions to interpolate a new point x^*, see e.g. Mackman et al. [168]. The Euclidean norm between a new sample site and all existing points in the data set provides the spatial dependency. Different basis functions are used to built the surrogate, including, but not limited to, linear, cubic and thin plate splines [162]. Furthermore, with more complex parameter estimations for the approximation, Gaussian or multiquadric basis functions offer more freedom but are more expensive to build [162]. Besides their use in engineering applications [177], such as aerodynamics [178], they are also used as interpolation methods for neural networks [162] or mesh morphing [179; 180].

Kriging, a subset of Gaussian process regression, is a stochastic interpolation method to approximate functions based on spatial correlation. It was mathematically

formulated by Matheron [181] and named after Krige, a South-African mining engineer. The approach was adapted into the design and analysis of computer experiments with the work of Sacks et al. [182]. Kriging as best linear unbiased predictor (BLUP) is closely related to Bayesian optimization methods [182]. Since then it has been expanded and developed with works of Jones and Schonlau [183],Jones [184] and more recently for engineering by Forrester et al. [162]. A prediction is the linear combination of the weighted sum of the samples used for generating the model. The spatial correlation prescribes a stronger relationship between close samples, with decaying strength for samples further away. It can approximate multimodal and non-linear functions and is characterized as the best unbiased predictor [182]. Extensions of Kriging allowed for enhanced modelling, for instance using gradient information, named Gradient Enhanced Kriging [185; 186], to enhance the initial model. Regression Kriging [187; 162] was developed for estimations if noisy data is present to reduce the risk of overfitting. Also, Kriging with partial least squares [188; 172] is used for high dimensional problems to reduce computational burden on the parameter estimation. Furthermore, as a stochastic approach, Gaussian processes allow an estimation of the error in the model, a generation of a confidence interval. This enables additional possibilities in the optimization processes, where this information can be used to efficiently improve the model locally or globally and therefore enhance the optimization process. The application of Gaussian process regression and Kriging in aerospace engineering are manifold, including aerodynamic [170; 189; 167], structural [16] and aeroelastic [190; 191] optimization, aircraft design [192], propulsion [193] or mission analysis [14].

Another way to approximate functions is the use of support vector regression [194; 195]. Based on data classification with support vector machines, it can be used for predictions when an underlying statistical error is expected, as for instance in physical experiments or discrete computations with errors due to meshing. A specified margin ϵ is introduced with which an error in the sample data is accepted that will not affect the prediction at a new point. Its application in aerospace engineering ranges from aerodynamic [196; 197] and aeroelastic optimization [198] to MDO of aircraft in conceptual design [199].

Machine learning techniques such as Deep Neural Networks [200; 163; 201], Generative Adversarial Networks (GAN) [202; 203; 204] and Deep Belief Network (DBN) [205] are another type of surrogate. For aeronautical applications they are employed, for instance, for airfoil optimization [200; 163; 202; 204; 205; 201] and wings [203; 205; 201].

Usually they require a large training data base and therefore are not suitable for every application.

To further reduce the computational burden of expensive evaluations the use of multi-fidelity model surrogates is another alternative. The combination of different levels of fidelity allows to obtain knowledge with many inexpensive low-fidelity models joined with accurate responses of high-fidelity models [162; 206; 155]. For instance, in an optimization including aerodynamic assessments, high-fidelity CFD evaluation can be supported by lower cost methods such as panel methods, vortex lattice methods or lifting line methods. Those lower fidelity methods are orders of magnitudes cheaper to evaluate, allowing for a vast design space exploration and exploitation, while only a few CFD evaluations are used to obtain more accurate results. To merge the information, different approaches are used, including additive, multiplicative or hybrid information fusing [207; 155]. Multi-fidelity models have a range of application in aircraft design, with the use of Kriging [166; 208; 209; 210; 191; 211] as well as machine learning techniques [205; 212; 201]. Besides the merge of two surrogate models with bridge functions, Cokriging is an approach where low- and high-fidelity information is directly joined in one model [213]. Emerged in the field of geostatistics, the low-fidelity information is correlated with the high-fidelity data [155]. While the multi-fidelity approach of Co-Kriging can support an improved surrogate model, challenges are related to the hyperparameter estimation and the correlation matrix size, of which the inverse has to be determined [155]. This increase in complexity can jeopardize the progress of an adaptive surrogate sampling approach.

1.4.4 Infill points and Adaptive Sampling Techniques

With the model built, it can now be searched for a minimum in lieu for the expensive physics based model to determine a new design site for the optimization process [214]. Herein, classical optimizer can be employed, given the surrogate provides the necessary data and fulfills the requirements, for instance smoothness and continuity. This includes gradient based optimizations, such as simplex or sequential linear-quadratic programming, as well as gradient-free optimizer, like genetic algorithms or particle swarm optimization. The computational costs of a single evaluation can now be disregarded as they are usually distinctively lower.

New infill points are proposed by an acquisition function, which is based on the objective and constraint function surrogates and their responses are evaluated with

predictive tools [161]. Assuming the initial DoE has a low number of samples, limited knowledge is present in the surrogate model, which shows more of a general trend over the design space, rather than detailed insight. Thus, using the mean prediction of a surrogate model can lead to a slower or unrealized exploration of the design space. Therefore, one wants to find a balance between a global search for regions of interest (exploration), where a possible optimum can be located and a local search to exploit an optimum with the already existing information (exploitation). In stochastic approaches, like Gaussian processes and Kriging in particular, one can use an acquisition function based on the surrogate model information that can be minimized or maximized [215]. Using the confidence interval in the acquisition function emerged in the use of efficient global optimization (EGO) by Jones and Schonlau [183]. Furthermore, Jones [184] reviews different search algorithms for response surface models and presents their downfalls and advantages. Watson and Barnes [216] gave an overview of different approaches for new infill points, aiming for finding the threshold-bounded extreme, the regional extreme or minimizing surprises. They were discussed by Sasena et al. [217] and extended to the approach of minimizing the uncertainty, as well as used in other works [218; 170].

With new found infill samples and their evaluations at hand, the surrogate models are rebuilt during the optimization process, increasing the accuracy of the surrogate models [219]. This is especially observed at the initial phase, when only a few sample points are used, and the surrogate model is not expected to be a good representation of the real function [219]. This adaptive sampling approach is commonly used in surrogate based optimizations, including aeronautical applications. Da Ronch et al. [220] use a simultaneous infill sample for local and global space filling methods to increase accuracy in non-linear aerodynamic predictions. Iuliano and Pérez [159] proposed an objective-driven and error-driven adaptive infill criterion and showed its feasibility based on a 2D airfoil aerodynamic optimization. Further, expected hyper volume improvement [221] and hyper volume iteration [222] were used in aerodynamic shape optimization applications.

1.4.5 Termination Criteria of a Surrogate-based Optimization Process

Terminating the optimization process is an ongoing challenge in surrogate based optimization [223]. If the optimum would be known, a termination criterion is the

closeness to this design. This can be used to measure the performance with test functions. However, in a typical engineering problem the optimum is not known a priori, and it is desirable to reach a convergence, where consecutive infill points are located close to each other with similar response, as an asymptotic convergence. Some termination criteria are proposed, based on the improvement of a new solution [192; 223] or a worth-based criterion [183]. Though, with expensive real function evaluations this can occur to be unfeasible, and more often a termination is triggered by a maximum number of iterations [217; 218].

1.4.6 Optimization with Surrogate-based Constraints

As most engineering problems are exposed to constraints, a way of considering them in SBO is important, especially if they can also be categorized as expensive to evaluate. If response surfaces are used for the objective and the constraint functions, more uncertainties are present, as both objective and constraints, are not expected to be accurate in the initial phase. Therefore, it might be more challenging during an optimization to not only identify regions of interest for minima (local or global) but also to detect feasible regions. Using the mean prediction without considering the uncertainty of the models can misslead the optimization process and slow it down. With progress in the process more knowledge is gained about the real functions, though, to find promising sample points and acquire an efficient optimization is the problem at hand. Audet et al. [224] proposed the use of the expected violation, derived from the EGO formulation for bounded problems and applied it to mathematical problems and a simple aeronautical application. Remaining challenges were seen in larger problems and a need for advanced tests and refinements of the method. Based on EGO [183], Sasena et al. [217] considered constraint in the approach, developing the super efficient global optimization (SEGO). Following a Kriging approach for the objective and constraints, the uncertainty in the models can be used to determine infill points beneficial for both, feasible region identification and objective improvement. It was concluded that now advantage is present by favoring a penalty method over probability method for bound optima, as a challenge is the transformation of the constrained optimization into an unconstrained problem. Further, Martínez-Frutos and Herrero-Pérez [225] used a feasibility quantification approach for the constraints together with adaptive sampling based on expected hyper volume improvement. Its applicability was shown for a multi-objective optimization problem, where a pareto

front exist for equally valued solutions. Priem et al. [226, 227] proposed an upper trust bound, which relaxes the constraints based on the uncertainty in the process. With a parameter to tune the uncertainty consideration throughout the optimization process it allows for a flexible approach. However, with an inadequate choice of the parameter the optimization has the risk of searching far in the unfeasible design, encountering issues of evaluating the real functions due to physics based problems. Overall, for aeronautical applications the different approaches have been used, for instance in aerodynamic shape optimization [189; 228; 173; 222]. However, it is still a field of research to introduce constraint surrogates into an optimization process in an efficient way.

1.5 Objectives of the Work

The objectives of this work result from the involvement of a project with an external industrial partner. They include aspects regarding novel aircraft configurations with flexibility effects and the assessment in a multi-disciplinary and multi-fidelity design optimization environment. Further, surrogate based optimization is an additional feature of interest originating from the research perspective. Thus, the objectives of the work can be concisely summarized as:

- **Multi-disciplinary design optimization of novel aircraft configuration**
  A main focus of the work is the assessment and optimization of unconventional novel aircraft configuration, specifically a high aspect ratio wing designs and a strut-braced wing design. The assessment of the influence of flexibility and aeroelastic performance is of interest for designs proposed for future aviation.

- **Development of a multi-disciplinary design optimization environment**
  Integrating evaluation tools of different levels of fidelity to support a cost-efficient design optimization. Furthermore, assessments of unconventional aspects related to flexible aircraft are performed. This includes geometric non-linearities for wings of high aspect ratio. The utilization of surrogate models for costly objective and constraints is followed.

- **Reduction of computational costs in a preliminary aircraft design environment**
  To obtain substantial results allowing for qualitative and quantitative statements

for the optimization process, it is of interest to reduce the computational cost due to expensive evaluations at the preliminary design stage. Therefore, an assessment of the necessary fidelity level is performed and the use of efficient optimization methods is pursued. An a priori high- and low-fidelity assessment of a range of initial configuration supports the understanding and approach to reduce the computational time. consequentially, the necessary fidelity in the multi-disciplinary preliminary design optimization is categorized to obtain reliable and conservative data.

- **Advance and development of infill criterion for surrogate-base optimization**
  A secondary objective, emerged while progressing within the project is the demand for advances in surrogate-based optimization procedures. While relatively easy to employ and integrate in an optimization procedure, challenges are still present regarding the iterative process and the search for improved designs. Hence, as an additional objective the improvement of surrogate-based optimization was formulated. This includes the development, testing and application of a proposed methodology.

1.6 Novelties and Contributions to State of the Art

The key contributions of this dissertation consist of:

- **Probability of feasibility infill criterion**

  With a novel approach, an efficient way is proposed and tested for an infill criterion to drive a SBO towards improved feasible designs. It is able to match the performance of an established approach (upper trust bound) with similar design improvements and computational cost. Limitations are related to the convergence behaviour, as with many surrogate based optimizations.

- **Multi-disciplinary design optimization of two novel aircraft design with consideration of flexibility**

  Developing and employing a MDAO methodology, two novel designs, a HARW and a SBW were optimized regarding a multi-objective goal, considering an operational and manufacturing cost metric in a transonic flight regime. The

multi-fidelity assessment of the aerostructural behaviour allowed a more thorough investigation of flexibility influence.

- **Non-linear assessment of novel aircraft performance considering flexibility**

  A direct comparison of designs analysed with a linear and non-linear structural model was performed. As the designs considering the linear model were the results of an optimization process, additional potential and possible issues could be extracted from the evaluations. It could be shown that the linear model for the stress constraint performs conservative compared to the non-linear model. Contrary, the non-linear model offers further optimization potential, despite being computationally more expensive. For the conventional HARW design the difference was not significant and possible gain is seen less advantageous. For the SBW configuration however, the differences were more distinctive and with an increase in computational power, non-linear assessments can be worthwhile for an optimization.

1.7 Publications

As part of the research conducted, journal paper and conference presentations were published. The content was partially incorporated in the thesis context. Following a list is presented containing the names of the works and the contribution of the author.

- "Surrogate-based optimization based on the probability of feasibility" [229]; as the main author of this work, most of the content is the responsibility of the author. This includes the development of the methods and the implementation of the methodology. The discussions, written part and editing was divided between all authors.

- "On the Multi-fidelity Approach in Surrogate-based MDO of HARW aircraft" [230]; as second author to the article, the contributions are the conduction of the computational work, the discussion of the results and development of the methodology. The author was involved in the writing and visualization of the results, as well as the editing.

- "Optimization and comparison of strut-braced and high aspect ratio wing aircraft configurations including flutter analysis with geometric non-linearities"

[231]; being the first author of the article, the methodology, computations and portions of the implementation were conducted for the work. Further, the result discussions were guided and the writing and visualisation were performed. Partially, the editing was carried out.

- "Surrogate based MDO of a canard configuration aircraft" [232]; the contribution as second author was to provide the implementation of the surrogate methodology and the discussion of the surrogate based results. The involvement in the editing part included the visualization of the results and the discussion of the methodology.

- "Surrogate-based Multidisciplinary Design Optimization on an UAM-VTOL Aircraft for Energy Minimization" [233]; as third author the contributions were focused on the surrogate based implementation, optimization and discussion of the results. The adaptive sampling method was driven in particular for the optimization. In the writing and editing, the methodology was discussed and the details were explained and introduced

- "A framework for multi-fidelity multi-disciplinary kriging-based surrogate model optimization of novel aircraft configurations" [234]; as part of a NATO specialists meeting this work was performed mostly by the first two authors. The contribution of the main author was the computation and implementation of the surrogate methodology and the optimization. In the writing and editing the surrogate background was contributed, as were the visualizations of the results. In a similar conference environment, parts of the work were presented at the 2020 flutter council organized by Lockheed Martin 2020.

1.8 Thesis Layout

After the extended literature review in chapter 1 the organisation of the remainder of the thesis is as follows:

- Chapter 2 introduces the methodology and tools of the work. The models of the multi-disciplinary design analysis framework are introduced and described, including the required mathematical background. Additional models necessary for the analysis are described and all tools are brought into context towards the MDAO methodology.

- In chapter 3, the aspect of the surrogate modelling is addressed. The decision for the employed surrogate justified and the chosen approach, Kriging, is introduced together with the infill criteria based on its stochastic properties. A newly proposed approach of considering the constraints with the probability of feasibility together with a normalized objective function is described. The chapter concludes with mathematical test cases to show the applicability of the new method.

- Starting in chapter 4 with an aerodynamic shape optimization, the introduced methods are applied to engineering problems in the following chapters. A transonic airfoil is improved regarding its drag with aerodynamic and geometric constraints, wherein the proposed method to determine new infill points for the surrogate-based optimization is employed. The method is compared with alternative approaches and the results of the optimization are discussed regarding efficiency, obtained infill points, benefits and disadvantages.

- In chapter 5, the multi-disciplinary design optimization methodology is explained, with integration of different tools and a HARW and a SBW aircraft are optimized With the introduced process for a preliminary design study. It is examined to which extend low- and high-fidelity computational analysis is necessary to achieve reasonable and feasible results given the constraints of available computational power and time. It includes the consideration of flexibility in the preliminary design and identifies the challenges of doing so. The results are discussed for the optimization as well as the findings of the employment of high-fidelity CFD tools and low-fidelity aero-structural methods.

- Chapter 6 concludes the applications with a mutual comparison of the respective optimization and briefly condenses and discusses the results. The additional objective of the influence of geometric non-linearities towards the performance of designs is investigated in the second part of the chapter. The optimization outcomes of the HARW and the SBW aircraft considering the linear structural model in the aeroelastic optimization are assessed considering geometric non-linearities and conclusions are drawn regarding the feasibility and benefits.

- Chapter 7 concludes the thesis. Remarks are drawn from the findings of the current work and place them into the context of the objectives and novelties of this work. A brief outlook of possible future work completes the thesis.

Chapter 2

Multi-disciplinary Design Analysis Tools

The complexity in aircraft design requires the analysis and optimization of multiple different disciplines. Therefore, the use of tools capable of considering aeroelastic effects in novel, more flexible aircraft is inevitable. The multiple disciplines, mostly aerodynamics, structure and their mutual influence, is a challenging and computationally expensive task. However, the use of MDA tools is a key factor for further improvement on one side for the advance in existing designs as well as assessments of novel concepts. MDO with the use of MDA methods can reach a better optimum since two (or more) disciplines are optimized at the same time rather than sequentially. This chapter introduces and describes the used tools and analysis models of the MDA framework, which are integrated in the MDO methodology.

This includes the low-fidelity aerodynamic and structural implementation, based on a 3D panel method and an equivalent beam model, respectively, to evaluate the FSI problem. The integration of the high fidelity fluid-flow solver and the interaction between the tools is explained. Furthermore, a brief overview is given for the additional modules for non-structural mass point and fuel distribution. As NASTRAN is utilized for the flutter calculation, a summary is provided about the background and the models herein used.

2.1 Computational Aeroelastic Framework

For the computation of the aeroelastic solution a framework developed by the research group was used. It was created to study aircraft with flexible and morphing wings in the scope of the European project NOVEMOR[1] and continuously expanded to suit the needs of analysis and optimization of novel aircraft configurations.

The following described models were developed and only adapted where necessary to incorporate the analysed models. This includes the implementation of the design variable definition in the source code, small modifications in the geometry definition, and data transfer between the already existing tool and external sources. As those modifications to the code are not significant for the background of the tool and the methodology, they will not be explained in more detail. Following, an overview is given over the implemented models and corresponding theoretical backgrounds.

2.1.1 Aerodynamic Evaluation based on a Panel Method

In Preliminary design it is of interest to obtain fast results to explore the design space more thoroughly, even though one might need to relinquish some accuracy. Low- and medium-fidelity tools offer this capability. Therefore, the aerodynamic model of the framework used in the FSI process is based on a 3D panel method, offering accurate lift and induced drag results for subsonic speeds. The geometry is represented by a mesh consisting of small panels, as shown in Fig. 2.1. Wake panels are necessary to close the system and obtain the pressure values on the surface.

The solution is based on potential flow theory, solving an irrotational, inviscid and incompressible flow field. It is expressed with the Laplace equation in terms of the velocity potential Φ:

$$\nabla^2 \Phi = 0. \tag{2.1}$$

The solution is obtained by Green's theorem, imposing a Dirichlet boundary condition to fulfill the far field boundary conditions and the impermeability boundary condition:

$$\frac{1}{4\pi} \int_{\text{body+wake}} \mu \frac{\partial}{\partial \text{n}} \left(\frac{1}{r} \right) dS - \frac{1}{4\pi} \int_{\text{body}} \delta \left(\frac{1}{r} \right) dS = 0. \tag{2.2}$$

With source and doublets elements of constant intensity, the wake modelled as constant doublet distribution and the Kutta condition applied, one can solve the systems of

[1] `https://cordis.europa.eu/project/id/285395`, accessed: Dec. 10^{st} 2021

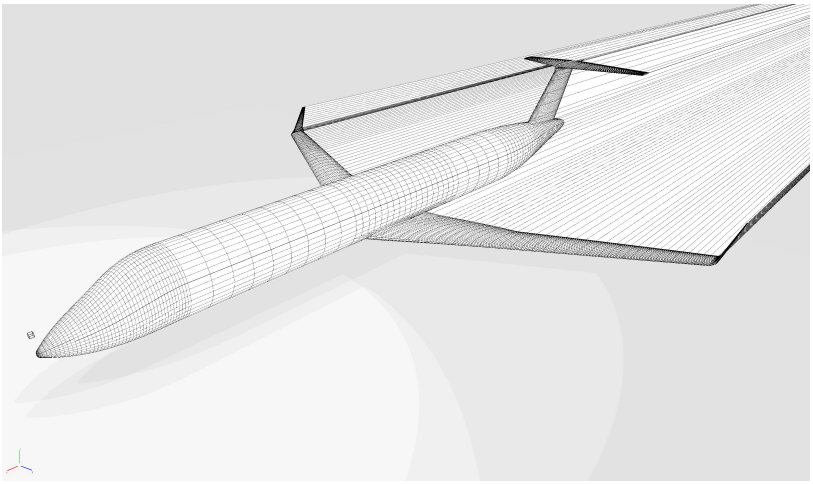

Figure 2.1: Picture of a representative Aerodynamic model in MDOGUI

equation for the velocity potentials for each panel discretizing the body. Subsequently, differentiating the doublet distribution to obtain the tangential velocity, the pressure can be gained with Bernoulli's equation for potential flow with:

$$C_{p,0} = \frac{p - p_\infty}{\frac{1}{2}\rho v_\infty^2} = 1 - \frac{v^2}{v_\infty^2} \tag{2.3}$$

where p_∞ is the free stream reference pressure, ρ the air density and v_∞ the free stream velocity. Afterwards, with the geometry of the panels the distributed lift is obtained and the integral over the whole surfuace provides the absolute lift.

The model has additional correction implemented accounting for compressiblility with the Prandtl-Glauert rule:

$$C_p = \frac{C_{p,0}}{\sqrt{1 - \mathrm{Ma}_\infty^2}}, \tag{2.4}$$

and friction drag correction C_{D_f} based on flat plate boundary layer models, calculated as:

$$C_{D_f} = C_f F \frac{S_{\mathrm{wet}}}{S_{\mathrm{ref}}}. \tag{2.5}$$

Ma_∞ in equation 2.4 is the free stream Mach number and the variables in equation 2.5 are the friction coefficient C_f, the form factor F, the wing wetted area S_{wet} and the reference area S_{ref}. More detailed descriptions of these models regarding the formulation can be found in Katz and Plotkin [117] and regarding the validation in Suleman et al. [119] and Afonso et al. [120].

Although fairly accurate to predict lift in the linear range of angles of attack (AoA), the model is not suitable to accurately predict transonic drag, shocks and shock-boundary layer interactions or separation. While some of the inaccuracies can be partially encountered by correction factors, the limitations of the method needs to be kept in mind.

2.1.2 Structural Assessment by an Equivalent Beam Model

The wing structure is represented by an equivalent 3D beam model, where the properties of a rectangular wing box per defined section are condensed in the node of the beam model [100]. Fig. 2.2 shows a representative model, with the fuselage as beam model and the wing and empennage with the wing box representation.

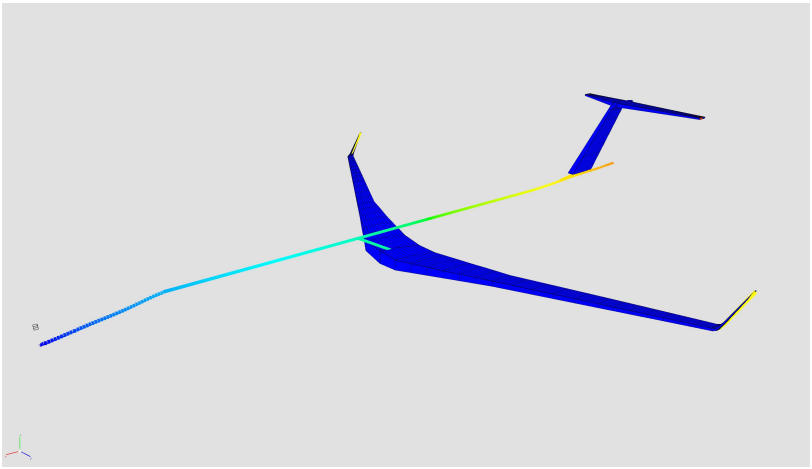

Figure 2.2: Picture of a representative structural model in MDOGUI

The low-fidelity FE model fits the wing representation of long and slender wings and allows to capture the most important structural phenomena for preliminary aircraft design. Despite offering higher accuracy, Higher-fidelity FE models require more computational cost due to the higher number of degrees of freedom [235] and are therefore not used at this stage of the design.

Besides a chord wise position of the start and end point of the wing box, similar to a front and rear spar, the upper and lower box thicknesses are defined. The inertia properties and the centroid of the box are computed via thin wall theory and the wing box parameters. With the present model, one can obtain estimations of the wing box mass as the distribution of the Von-Mises stress along the wing for the beam sections.

A short explanation should be given here with referenced work for more details for the interested reader.

Euler-Bernoulli beam theory [236] is applied, representing each beam element with two nodes with six degrees of freedom each. The assembly of four elements, a bar for tension, two beams for bending, and one torsion, provides a full description of the beam. Shape functions $[N]$ define the relation between the displacement field $\{u\}$ and the nodal displacements $\{d\}$ by:

$$\{u\} = [N]\{d\}. \tag{2.6}$$

To obtain the strain field $\{\epsilon\}$ for an element, a strain-displacement matrix $[B]$ and the nodal displacement $\{d\}$ are formulated as:

$$\{\epsilon\} = [B]\{d\}. \tag{2.7}$$

With isotropic and elastic material assumed, the stress field $\{\sigma\}$, including axial force and bending moments in three planes, can be formulated as:

$$\{\sigma\} = [D]\{\epsilon\}, \tag{2.8}$$

with the elasticity matrix $[D]$. The implemented Finite element method uses the variational method, applying the principle of virtual work to obtain the displacements in a static analysis. Given the potential energy U of the beam element as:

$$U = \frac{1}{2}\{d\}^T[K]\{d\} - \{d\}^T F, \tag{2.9}$$

With $[K]$ and $[F]$ being the stiffness matrix and the load vector of the element. After transforming from the beam coordinate system into the global coordinate system, the static equilibrium and the displacement is then:

$$\frac{\partial U}{\partial \{d\}} = 0 \rightarrow [K]\{d\} = \{F\}. \tag{2.10}$$

To solve this system of equations, the framework has different decomposition methods (LU, QR, Cholesky) implemented and chooses the most suitable on to invert the stiffness matrix.

The framework is further prepared to incorporate geometric non-linearities in

the analysis. For this cause, some modifications in the formulation are necessary, shortly described in the following part. As the stiffness matrix is now dependent on the deformed state itself, no explicit calculation is possible and an iterative method is necessary to obtain the static equilibrium state. A Newton-Raphson method is implemented in the framework to reach the equilibrium between the applied load $\{F\}$ and the restoring force $\{R\}$ of the internal structure:

$$^{t+\Delta t}\{F\} - {}^{t+\Delta t}\{R\}^i = \{0\}. \tag{2.11}$$

The restoring forces are obtained from the stiffness matrix of the previous iteration with the current displacements:

$$^{t+\Delta t}\{R\}^i = {}^{t+\Delta t}[K]^{(i-1)}\{d\}^i. \tag{2.12}$$

To treat large displacements and angles, the net displacements and the gimbal angle approaches are used in the framework. However, considering large strains is not possible with the implemented formulation. The consideration of stress stiffening effects is done by a non-linear consideration $[B_{nl}]$ in the strain displacement matrix:

$$\{\epsilon\} = ([B] + [B_{nl}])\,\{d\}. \tag{2.13}$$

For the non-linear component, large displacement and geometric stiffness can be considered. The latter is transformed to a function of the stress state, while the former is disregarded due to usual procedures.

2.1.3 Fluid-Structure Interaction Implementation

To evaluate the aeroelastic behaviour a fluid-structure interaction assessment is necessary. The FSI module of the framework couples the aerodynamic forces with the structural displacements. The implemented process is categorized as loosely coupled or partitioned, since the solution process of the structural and fluid solver is decoupled [237]. Each model is solved separately and the information is then sequentially given to the other solver. In this iterative process the aerodynamic loads are transferred to the structural model and the nodal displacements are calculated until the following

equilibrium is satisfied:

$$[K]\{q\} - [M]\{g\} - [A_K]\{q\} \approx 0, \tag{2.14}$$

where $[K]$ is the stiffness matrix is the structure, $\{q\}$ is the systems degree of freedom, $[M]$ is the element mass matrix, $\{g\}$ is the gravity vector and $[A_K]$ is the aerodynamic stiffness matrix. In turn the new deformed shape is fed back to generate the new geometric shape, a remeshing takes place and the new resulting load is calculate.

As in general the mesh resolution of the aerodynamic and the structural mesh are dissimilar, a procedure to transfer the aerodynamic forces and the structural displacements between the meshes with different resolution is necessary. Thus an algorithm transfers the aerodynamic force components of each panel to the two nodes of the closest finite element according to their distance. When the structural displacements are obtained, the aerodynamic mesh is deformed accordingly. In this deformation it is assumed that an airfoil section can rotate in its own plane, but is not deformed.

To enable a more robust solution process, the load steps can be incremented and the applied load is increased in an advancing manner. This way, the solution advances only when the equilibrium between the (reduced) aerodynamic and structural load is reached. Additional mass points, rigidly linked to the closest nodes, follow the deformation and are relocated accordingly. When the nodal displacements for the flexible structure consecutively fall below a predefined threshold, the process is terminated.

2.1.4 Consideration of Non-structural Inertia Mass

Non-structural masses are modelled as mass points, rigidly linked to the closest node. Those include payload and system masses that are a user input and can be distributed in the model. They are defined by their location in the global reference frame, the mass and the inertia properties in their local reference frame. Further, fuel mass is modelled as mass points located in predefined storage space in the wing or the fuselage. It is partitioned in small elements and horizontally leveled in its respective storage to respect the predefined fuel mass. Fuel sloshing is not included in the evaluation by the framework, as steady flight conditions are assumed. In the FSI process, the rigidly bounded mass points follow the displacement of the structure. Fig. 2.3 depicts the models with visualized mass points.

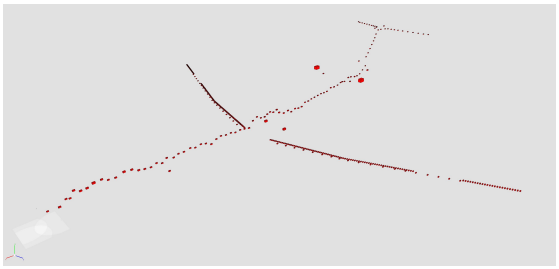

(a) Payload model with distributed mass points

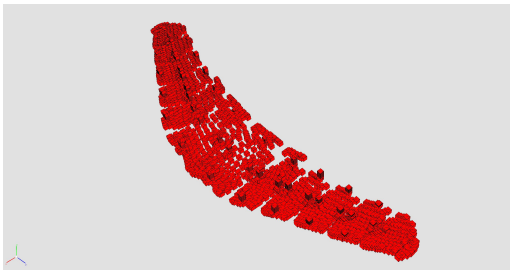

(b) The fuel mass in the wings

Figure 2.3: The two different classes of non-structural mass points, the fixed system and payload masses (a) and the horizontally leveled fluid masses (b)

2.2 High-fidelity CFD and Integration in Multi-disciplinary Design Analysis

The formerly described models aim for the analysis of aircraft up to high subsonic speeds (Ma ≤ 0.7), for which linearized aerodynamic potential theory suffices. The limitation of the aerodynamic methodology for assessment of the transonic flight regime called for an integration of higher-fidelity CFD. Therefore, an interface with a commercial CFD software, StarCCM+ [238], which is able to solve Reynolds Averaged Navier–Stokes based CFD (RANS CFD), was developed to enable the communication between the existing framework and the commercial software. This integration was not in the scope of this work and hence, only an overview of the most important aspects is given to understand the implementation and the use.

The RANS equations are used to model the flow domain Ω, which can be written in the differential form [239] as:

$$\frac{\partial \boldsymbol{U}}{\partial t} + \nabla \times \boldsymbol{F}^c - \nabla \times \boldsymbol{F}^v - \boldsymbol{Q} = 0 \quad \text{in } \Omega, \quad t > 0, \tag{2.15}$$

where $\boldsymbol{U}$ is the vector of state variables, $\boldsymbol{F}^c$ is the vector of convective flux, $\boldsymbol{F}^v$ represents the vector of viscous flux and $\boldsymbol{Q}$ denotes the source terms.

The turbulence model used to close the RANS formulation is Menter's shear stress transport (SST) $k-\omega$ model [240] and an all-y$^+$ wall treatment is employed. It provides a solution for the transport equations for the turbulent kinetic energy k and the specific dissipation rate ω to determine the turbulent viscosity.

While the interface offers some flexibility in the chosen options for the analysis, some limitations are given for the RANS CFD analysis, as the application is mostly

focused on the analysis of aircraft in the transonic flight regime. The geometry is defined solely in the framework and passed directly to the CFD solver, meaning a separated mesh preparation is not performed. Therefore, the mesh generation is delegated to the meshing procedure of the used commercial tool. It is based on a hexagonal surface mesh that is expanded to a volume mesh consisting of polyhedral cells. The exact meshing procedure is internally performed and not further discussed here.

Refinements are generated automatically as part of the geometry transfer for the leading and trailing edge of all present lifting surfaces (wing and tail in case of a full aircraft). A factor is available to adapt the global refinement size. Further, the aircraft is enclosed in a refinement box with adaptable cell size.

The fluid volume is predefined and consists of a quarter sphere as inlet and a block to fully enclose the aircraft. As symmetric flow conditions are present, only a half model is used to reduce the computational costs. If non-symmetric conditions would be investigated, a full aircraft model would be necessary. The distance margins between the aircraft surface and the outer boundaries of the fluid body are an approximation of wing span distances, where the sphere radius is approximately 3 half span distances and the length aft of the aircraft is around 5 times the half wing span.

A mesh convergence study should be performed beforehand and the refinement factors should be fixed throughout an optimization to assure a consistent quality for comparison. This was the case for the chosen application and is described in more detail in the corresponding section (5.2 and 5.3). A limitation is the overall number of cells, where the available memory of the server is the limiting factor. The physical properties of the flow (e.g.density, viscosity, velocity, direction, etc.) are taken from the framework and transferred directly as input in the solver. The boundary conditions are a no-slip wall condition for the aircraft, a velocity flow inlet and a pressure outlet. Asymptotic convergence criteria for the lift and drag coefficients is employed, being 0.0001 and 0.00001 for ΔC_L and ΔC_D for consecutive iterations, respectively. A continuity criterion provides an additional convergence criterion, with a value of 0.001.

After a CFD run is completed, the forces on the aircraft surface are extracted from the cells and transferred back to the analysis tool. Here, the forces are interpolated to according to their location to be assigned to the structural mesh nodes.

2.3 Multi-disciplinary Design Analysis Integration

The described tools for evaluating the single disciplines are wrapped in the framework to mutually interact and exchange the data between them. Fig. 2.4 visualizes the stream of the MDA of the framework for a single evaluation of a flight condition. Given

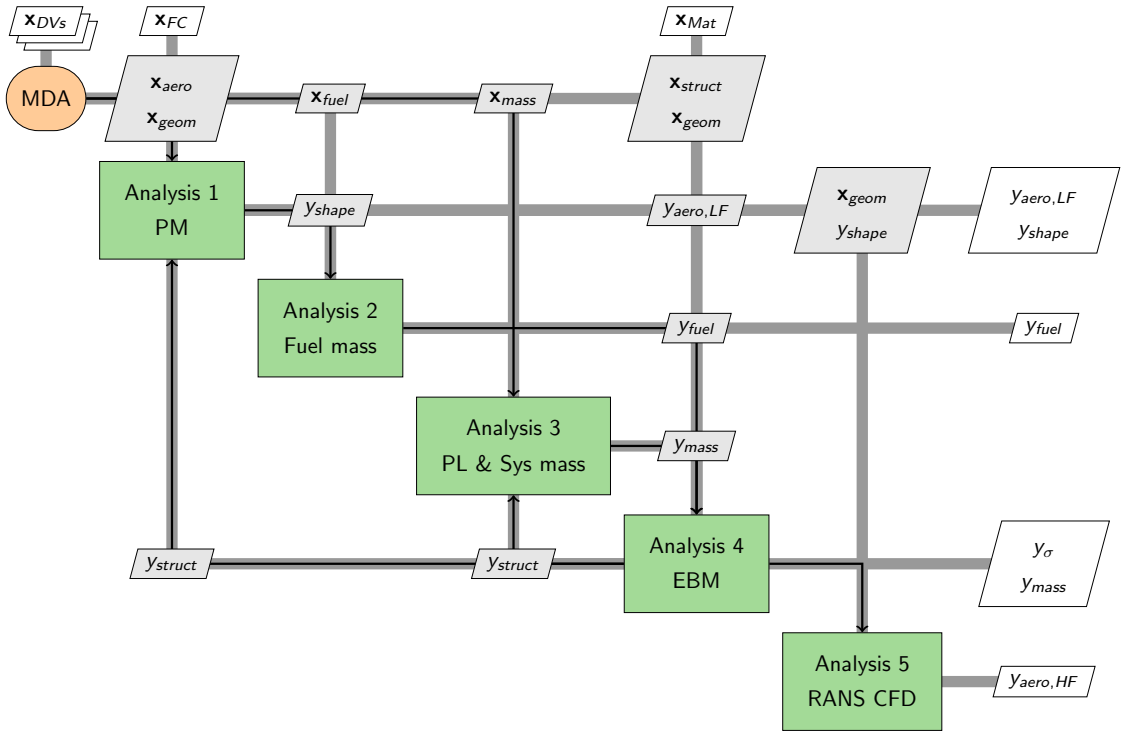

Figure 2.4: This is a flowchart of the MDA process performed with the MDOGUI. Incorporating the low and high fidelity panel-method and CFD for the aerodynamics and the equivalent beam model for the structure

the design variables and the imposed flight conditions as input, an aeroelastic solution is obtained, containing the mass estimation of the aircraft and the fuel consumption as output data.

Starting with the built geometry based on the design variables, the shape for the aerodynamic model is built. The computed aerodynamic load and the non-structural mass load is transferred to the structural model, where with the structural weight the deformed shape is generated with the FSI procedure. The final shape of the converged process serves as the input for the RANS CFD calculation. The acquired aerodynamic load is fed back to the structural model to obtain the shape caused by the high-fidelity CFD load. Therefore, the differences between the low- and high-fidelity results can

be quantified. With the given propulsion data, a fuel consumption can be calculated based on the drag results of the flexible aircraft.

2.4 Flutter Estimation Tool

To estimate the flutter boundary, NASTRAN is employed. The geometric input is derived from the formerly introduced framework and a MATLAB tool is employed to generate the necessary input file for the NASTRAN computation.

The aerodynamic model uses a doublet lattice method [241] to calculate the aerodynamic influence coefficient matrix. The structure is modelled with beam elements, considering the area and inertia properties (NASTRANs CBEAM and PBEAM). To obtain the aeroelastic flutter results, a linear spline connects the structural and aerodynamic model, where displacements are transferred from the structure to the aerodynamic model and the aerodynamic forces the other way around. For solving the flutter problem, the implemented PKNL method is used, which is based on the $p-k$ method [121] and sweeps through dynamic pressures given by the user in a matching triple of Mach number, velocity and density values.

The flutter equation in general form with the true airspeed v, the reference chord c and the density ρ is:

$$\left[\left(v^2/c^2\right)[M]\,p^2 + [K] - \frac{1}{2}\rho v^2\,[A(p)]\right]\{q\} = 0, \tag{2.16}$$

where the matrix $[M]$ contains the inertia properties connecting the inertia forces $\{Q_{in}\}$ to the generalized accelerations by:

$$\{Q_{in}\} = -[M]\{\ddot{q}\}, \tag{2.17}$$

$[K]$ defines the elastic properties by the generalized forces $\{Q\}$ and the generalized displacements $\{q\}$:

$$[K]\{q\} = \{Q\}, \tag{2.18}$$

and the matrix $[A(p)]$ are the unsteady aerodynamic forces, defined by:

$$\{Q_{aero}\} = \frac{1}{2}\rho v^2[A(p)]\{q\}. \tag{2.19}$$

For a fixed value of v, the determinant can be used to solve for p, defined as the

conjugate complex root

$$p = \gamma k \pm ik, \tag{2.20}$$

with k being the non-dimensional reduced frequency, defined as

$$k = \frac{wc}{v}, \tag{2.21}$$

and γ is the rate of damping.

In the $p-k$ method one assumes that the aerodynamic motions are harmonic, hence the aerodynamic matrix becomes $[A(ik)]$. Following that, for an estimated value of k, equation 2.16 can be solved for $p = \gamma k + ik$:

$$\left[\left(v^2/c^2\right)[M]\,p^2 + [K] - \frac{1}{2}\rho v^2\,[A(ik)]\right]\{q\} = 0, \tag{2.22}$$

to compute the $[A(ik)]$. This process is iterated until the imaginary part of p equals the value of k for the aerodynamics. From the converged process the damping and frequency can be calculated from the complex $p = \delta + ik$ via:

$$\gamma = \frac{\delta}{k} \quad \text{and} \quad f = \frac{vk}{2\pi c} \tag{2.23}$$

The damping and frequency results are subsequently used to identify the modes responsible for the flutter appearance. Fig. 2.5 shows an exemplary output for a v-g graph, where with the $p-k$ method a damping and frequency value is obtained. Plotting the results over a velocity range allows for the identification of the flutter. It occurs, when the damping becomes positive. In the frequency graph the coupling of two modes is clearly visible for the first and second mode. At this point, one mode becomes more damped, while the second coupled one has a reduced damping. Crossing the zero damping, one states that the structure flutters.

Correction inputs to resolve the transonic flow conditions with the linear aerodynamic model are not used in the implementation, as data for correction was too sparse. However, it was attempted to introduce correction based on single CFD results to model the shift in pressure distribution of the flight condition.

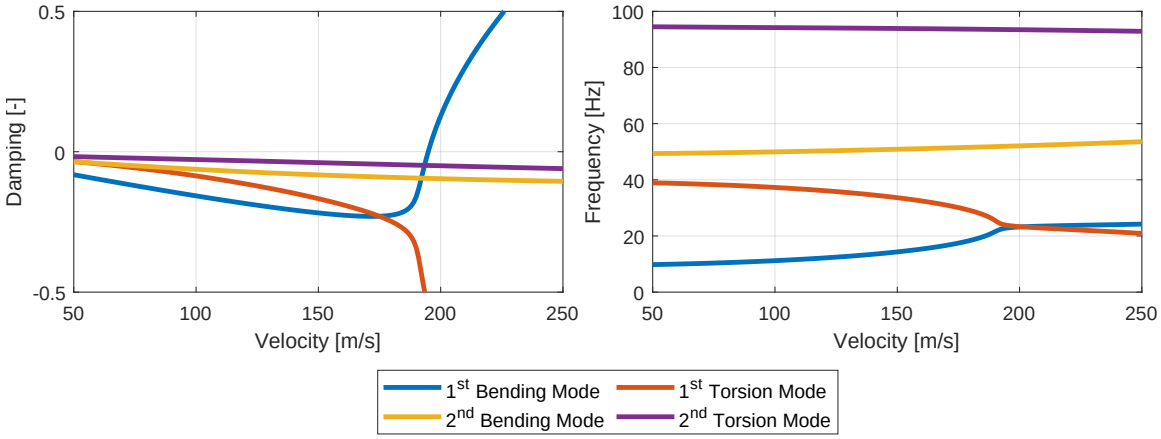

Figure 2.5: Exemplary v-g graph for the AGARD wing [242]. The onset of flutter is identified by a positive damping value. Further, the coupling of modes is visible in the frequency plot.

Chapter 3

Surrogate-based Optimization Methodology

This chapter describes in detail the theoretical background for the surrogate modelling. First, the rational is explained for the choice of employing a surrogate-based optimization, which is further extended to the reasoning for the decision to utilize a Kriging approach. Thereafter, more insight is given into the mathematical background and the different approaches for infill points, based on the uncertainty quantification of Kriging. A detailed explanation is then given about the constraint handling, with a focus on the proposed method for the probability of feasibility. At last, the implementation and integration into the optimization process is described.

3.1 Surrogate Methods and Choice of Model

The choice of the optimization method is influenced by a number of aspects. Those include if the optimization is focused on a global or a local improvement. Further, the cost of implementation can influence the choice for an approach, meaning the development and preparation of the optimization process. Another aspect is the cost of the optimization itself, in particular the number of evaluations throughout a process. If the evaluation of the models is computationally expensive, one is interested to reduce the number of evaluations.

For the application on the optimization of novel aircraft configuration, the optimization is focused more on a global scale. Obtaining more general features and regions of interest for possible designs is of higher benefit than a local exploitation of a specific

design. This is reflected also in the application later on (sections 4) where the number of design variables is in an intermediate range (< 50) and contain different disciplines. Therefore, the use of gradient based optimization methods appears not suitable, as they are in general local optimizer. The utilization of a multi-start approach could possibly counteract the issue, yet it is obtained with higher computational costs.

As the evaluation costs of objective and constraint functions are relatively high (minutes or hours rather than seconds), it is further desirable to lower the number of evaluations in the optimization process. Global optimizer such as evolutionary algorithms, simulated annealing or swarm-based optimization rely on a high number of designs to be driven towards an optimum [243]. This is to increase the chances of reaching a global optimum rather than a local one. Therefore, a number of methods are eliminated in the choice for a suitable approach for the intended work.

Other methods that recently increased in popularity are adjoint-based approaches. It is used in gradient based optimization and might have an issue with finding global optima. However, it is relatively cheap to obtain the gradient information of an evaluated point in the design space. It is therefore suitable especially for optimizations with a large number of design variables as the gradient information is independent of the dimensionality. This is attractive since otherwise gradients would need to be gained by laborious analytical calculation of the gradient or a finite difference approach if the latter is not available. Though, the implementation of adjoint methods requires a careful mathemaical treatment and further a software development down to the source code. If some of those prerequisites are not available, it can be arduous to develop.

With the mentioned methods and their respective issues, an alternative approach is the use of surrogate models. Herein, the real, expensive to evaluate function is approximated by a mathematical model. This surrogate of the real function can then be used in an optimization in lieu of the real function and optimizer, requiring many evaluations within their procedure, can be inexpensively employed.

Different surrogate models can be employed to model the response function of interest, including polynomial regression, radial basis functions, Kriging or artificial neural networks. A short overview of some of them was given already in section 1.4. Here, it will be discussed, why the model of choice is towards Kriging.

With its implementation, Kriging offers a regression or interpolation of the given set of data. If, for instance, numerical errors are present, this offers a feasible way to handle noisy data. Such discrepancies can appear due to mesh discretizations

or convergence criteria. Another advantage of Kriging is the relatively low required number of data samples to build a surrogate model. While it likely lacks accuracy due to the low knowledge, it offers a trend for the respone in the design space. This is specifically an advantage compared to machine learning approaches, such as neural networks, which require a large data base to build a model. With an increasing number of samples, the accuracy of Kriging increases and the fit of the surrogate and the real function becomes more alike. Using polynomial regression models can as well provide trends over the design space, however, with an increase in data points it becomes more difficult to fit the model to the real data. Increasing the order of the regression can counteract that to some extent, yet often leads to an over-fit and oscillation of the surrogate.

Since Kriging is a Gaussian process regression, its stochastic properties allows one to estimate a quantification of the error. This can be used to improve the model globally and locally or being integrated in the optimization process. Further, Kriging is the best linear unbiased predictor, fitting the model to the sampled data to be the most likely. It can be built with few initial samples, supporting the cost efficient optimization approach which allows for a low to medium number of design variables. However, the computational cost for fitting a model increases with the number of samples and design variables, as matrix inversion is necessary. This issue can be tackled with methods like partial least square Kriging (see 1.4), yet is not an issue in the application of interest for this work. Also, the Design and Analysis of Computer Experiments (DACE) toolbox [244] and the Surrogate Modelling Toolbox (SMT) [245] are among the available tools for building Kriging models, which can be extended to incorporate adaptations to suit the application.

Following herein, the mathematical background of Kriging and the related approaches for the infill criteria are presented. Furthermore, the constraint handling is explained, containing the new proposed method of a normalized probability of feasibility approach. The section concludes with some mathematical test cases for the proposed method. This discussion includes redrafted parts of the published article "Surrogate-based optimization based on the probability of feasibility" [229] in "Structural and Multidisciplinary Optimization, Springer".

3.2 Theoretical Background of Kriging

Kriging assumes measurements as the realization of a stochastic process and a global regression to obtain a deterministic response $y(\boldsymbol{x})$, expressed as mean function with stochastic deviation:

$$y(\boldsymbol{x}) = \hat{\mu}(\boldsymbol{x}) + Z(\boldsymbol{x}), \tag{3.1}$$

where $\hat{\mu}(\boldsymbol{x})$ is the estimated mean value and the random process $Z(\boldsymbol{x})$. Depending on the assumption for the mean value $\hat{\mu}(\boldsymbol{x})$, Kriging can be categorized in different ways. In the case of simple Kriging, a known constant mean value is assumed (μ), whereas for ordinary Kriging, a constant mean of unknown value is to be determined ($\hat{\mu}$). Universal Kriging can have a polynomial mean which is dependent on the location ($\hat{\mu}(\boldsymbol{x})$). The choice of which kind to use depends on the available data, if trends are expected or the implemented capability. In general, a constant mean is sufficient and favoured in the model building [155; 246; 247]. $Z(\boldsymbol{x})$ has an assumed zero mean value and the covariance:

$$\mathrm{cov}(\boldsymbol{x}, \boldsymbol{x}) = \sigma^2 \boldsymbol{\Psi}. \tag{3.2}$$

σ is the standard deviation and $\boldsymbol{\Psi}$ the correlation matrix, which is:

$$\boldsymbol{\Psi} = \begin{pmatrix} \psi^{(1,1)} & \dots & \psi^{(1,n)} \\ \vdots & \ddots & \vdots \\ \psi^{(n,1)} & \dots & \psi^{(n,n)} \end{pmatrix}. \tag{3.3}$$

The basis function expression ψ for the spatial correlation between the known responses is:

$$\psi^{(i_1,i_2)} = \exp\left(-\sum_{j=1}^{k} \theta_j |x_j^{(i_1)} - x_j^{(i_2)}|^{p_j} \right), \tag{3.4}$$

where the k-dimensional parameters θ and p describe the correlation between the known locations and the smoothness at those locations, respectively. For a value of 2 for the exponent p, one obtains the Gaussian correlation function, having a smooth transition at the sample point, meaning it has a continuous first derivative. Throughout the process, it is assumed the value is set to $p = 2$. Therefore, the correlation matrix $\boldsymbol{\Psi}$ contains all point wise spatial relations, with a diagonal of 1, if the built model interpolates all known points.

A factor λ of small value can be added to the diagonal of the correlation matrix to obtain a regression rather than an interpolation. This can be particularly helpful if

multiple points are close to each other to prevent an ill conditioned matrix $\mathbf{\Psi}$. Further, it enables the model to deal with small errors that can occur due to numerical limitations. Results obtained from discretized computer models can contain discrepancies due to the meshing process. With minor permitted deviations, allowing an error, numerical issues can be circumvented.

Estimation of the unknown parameters for the ordinary Kriging model (μ, σ, θ, p) is done with the likelihood function, which can be written as:

$$L = \frac{1}{(2\pi\sigma^2)^{n/2}|\mathbf{\Psi}|^{1/2}} \exp\left[-\frac{(\boldsymbol{y}-\mathbf{1}\mu)^T\mathbf{\Psi}^{-1}(\boldsymbol{y}-\mathbf{1}\mu)}{2\sigma^2}\right]. \tag{3.5}$$

Taking the log of the likelihood, differentiating it with respect to μ and σ give expressions for estimated mean and error:

$$\hat{\mu} = \frac{\mathbf{1}^T\mathbf{\Psi}^{-1}\boldsymbol{y}}{\mathbf{1}\mathbf{\Psi}^{-1}\mathbf{1}}, \tag{3.6}$$

$$\hat{\sigma}^2 = \frac{(\boldsymbol{y}-\mathbf{1}\mu)^T\mathbf{\Psi}^{-1}(\boldsymbol{y}-\mathbf{1}\mu)}{n}. \tag{3.7}$$

Substituting it back into Eq. 3.5 gives the *concentrated ln-likelihood* function:

$$\ln(L) \approx -\frac{n}{2}\ln(\hat{\sigma}^2) - \frac{1}{2}\ln|\mathbf{\Psi}|. \tag{3.8}$$

Maximizing it, one obtains the value for θ for the best statistical model fit.

To predict a response $\hat{y}$ at an unsampled site $\boldsymbol{x}^*$, augmented response and sample vectors are assumed as a modified correlation vector:

$$\boldsymbol{\psi} = \begin{pmatrix} \psi(\boldsymbol{x}^{(1)}, \boldsymbol{x}^{(*)}) \\ \vdots \\ \psi(\boldsymbol{x}^{(n)}, \boldsymbol{x}^{(*)}) \end{pmatrix}, \tag{3.9}$$

where ψ describes the correlation between the new point and the existing sample data base. With the resulting correlation matrix:

$$\tilde{\mathbf{\Psi}} = \begin{pmatrix} \mathbf{\Psi} & \boldsymbol{\psi} \\ \boldsymbol{\psi}^T & 1 \end{pmatrix}. \tag{3.10}$$

one obtains the ln-likelihood of the modified data and as the interest is towards the

prediction. Terms without $\hat{y}$ can be omitted and $\tilde{\boldsymbol{y}}$ and $\tilde{\boldsymbol{\Psi}}$ can be substituted to get:

$$-\frac{(\tilde{\boldsymbol{y}}-\mathbf{1}\hat{\mu})^T\tilde{\boldsymbol{\Psi}}^{-1}(\tilde{\boldsymbol{y}}-\mathbf{1}\hat{\mu})}{2\sigma^2}=\frac{-\begin{pmatrix}\boldsymbol{y}-\mathbf{1}\hat{\mu}\\ y^*-\hat{\mu}\end{pmatrix}^T\begin{pmatrix}\boldsymbol{\Psi} & \boldsymbol{\psi}\\ \boldsymbol{\psi}^T & 1\end{pmatrix}^{-1}\begin{pmatrix}\boldsymbol{y}-\mathbf{1}\hat{\mu}\\ y^*-\hat{\mu}\end{pmatrix}}{2\sigma^2}. \tag{3.11}$$

To take the derivative with respect to $\hat{y}$ to maximize the expression the inverse of the new correlation matrix is first obtained with the partial inverse formula [248] as:

$$\begin{pmatrix}\boldsymbol{\Psi}^{-1}+\boldsymbol{\Psi}^{-1}\boldsymbol{\psi}\left(1-\boldsymbol{\psi}^T\boldsymbol{\Psi}^{-1}\boldsymbol{\psi}\right)^{-1}\boldsymbol{\psi}^T\boldsymbol{\Psi}^{-1} & -\boldsymbol{\Psi}^{-1}\boldsymbol{\psi}\left(1-\boldsymbol{\psi}^T\boldsymbol{\Psi}^{-1}\boldsymbol{\psi}\right)^{-1}\\ -\left(1-\boldsymbol{\psi}^T\boldsymbol{\Psi}^{-1}\boldsymbol{\psi}\right)^{-1}\boldsymbol{\psi}^T\boldsymbol{\Psi}^{-1} & \left(1-\boldsymbol{\psi}^T\boldsymbol{\Psi}^{-1}\boldsymbol{\psi}\right)^{-1}\end{pmatrix}. \tag{3.12}$$

Inserted into Eq. 3.11 and differentiated one then obtains:

$$\left(\frac{-1}{\hat{\sigma}^2(1-\boldsymbol{\psi}^T\boldsymbol{\Psi}^{-1}\boldsymbol{\psi}}\right)(\hat{y}-\hat{\mu})+\left(\frac{\boldsymbol{\psi}^T\boldsymbol{\Psi}^{-1}(\mathbf{y}-\mathbf{1}\hat{\mu})}{\hat{\sigma}^2(1-\boldsymbol{\psi}^T\boldsymbol{\Psi}^{-1}\boldsymbol{\psi})}\right). \tag{3.13}$$

Solving for $\hat{y}$ the prediction with respect to the maximum likelihood estimation is:

$$\hat{y}(\boldsymbol{x})=\hat{\mu}+\boldsymbol{\psi}^T\boldsymbol{\Psi}^{-1}(\mathbf{y}-\mathbf{1}\hat{\mu}). \tag{3.14}$$

Further, with Kriging a mean squared error (MSE) can be estimated for a unknown response as:

$$\hat{s}^2=\sigma^2\left[1-\boldsymbol{\psi}^T\boldsymbol{\Psi}^{-1}\boldsymbol{\psi}+\frac{1-\mathbf{1}^T\boldsymbol{\psi}^{-1}\boldsymbol{\psi}}{\mathbf{1}^T\boldsymbol{\psi}^{-1}\mathbf{1}}\right]. \tag{3.15}$$

For the derivation of the MSE, the interested reader is refered to [182]. This concludes the basics of Kriging and further descriptions are now given for the infill points and constraint consideration.

3.3 Criteria for Infill Points based on Uncertainty Quantification

The purpose of the built meta model is now to use it for a minimization, where one needs to search it for promising locations to evaluate the real functions. If the generated model is accurate over the whole design space, the surrogate can simply be searched, as each evaluation is cheap.

However, the intent of the meta model is to generate a model with few initial real

function evaluations and it is therefore likely, that there is a substantial dissimilarity between the model and the reality. Thus, besides finding the optimum it is also a goal to locally increase the accuracy of the model in locations of interest whereas insignificant areas can be of lower accuracy. Using the mean prediction of the surrogate to minimize the objective generates a usually slow progress, as new samples often are sampled in the vicinity of known locations [162].

Further, with the solely prediction the uncertainty of the model is disregarded and can mislead the optimization process.

Fig. 3.1 shows the optimization and infill process for an example function, with the surrogate model in the upper graph and the infill criterion in the lower graph. The real response is shown as black line, which for an actual application is not known a priori. The four initial points are shown as blue dots and the created surrogate model based on those evaluations is shown as red line. The uncertainty is pictured as shaded red area. The blue line represents the infill criterion the optimizer sees in the process, here resembling the surrogate prediction. A new infill point, based on the minimum value found by the optimizer is indicated as green diamond (bottom) and green dashed line (top). The early uncertainty is large, yet the optimizer utilizes

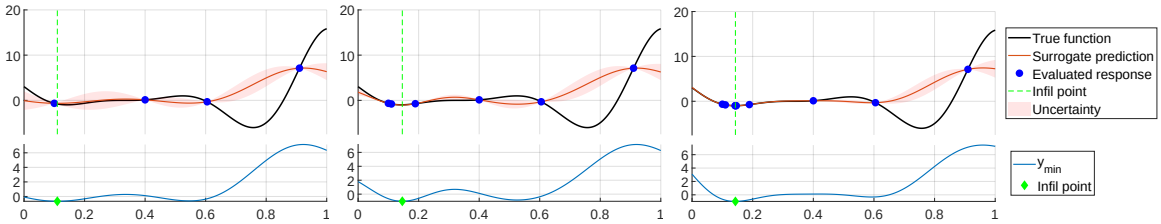

(a) Initial state (b) Optimization after two iterations (c) Optimization after five iterations

Figure 3.1: Process of an optimization utilizing a prediction-based infill criterion

the prediction only and searches with regards to it. In the advancing process it is visible that the optimization only progresses locally and the global optimum or its surrounding region is not identified.

By considering the uncertainty in the model, it should be ensured that not only a local minimum is found, but the design space is explored broadly enough to find the area of the global optimum. Therefore, rather than using the predicted response solely as objective function, an acquisition function can be defined, considering the prediction together with the present uncertainty of the model.

3.3.1 Expected Improvement

Jones and Schonlau [183] described the use of the *Expected Improvement* ($E[I]$) for efficient global optimization (EGO) and further investigated it [184]. In the current existing data set, the best achieved response is identified and the design space is compared against it considering the predicted value and the probabilistic expectation. This way, a balance between exploration and exploitation is achieved, where areas of high uncertainty can be searched despite having a poorer mean value. Due to its simple yet reliable balance between exploitation and exploration it finds application in engineering design until today [167; 173]. The formulation is as follows:

$$f_{Acq} = E[I(\boldsymbol{x})] = \begin{cases} (y_{min} - \hat{y}(x))\Phi\left(\frac{y_{min}-\hat{y}(\boldsymbol{x})}{\hat{s}(\boldsymbol{x})}\right) + s\phi\left(\frac{y_{min}-\hat{y}(\boldsymbol{x})}{\hat{s}(\boldsymbol{x})}\right) & \text{if } s > 0 \\ 0 & \text{if } s = 0, \end{cases} \tag{3.16}$$

where ϕ and Φ are the standard normal density and distribution function, y_{min} is the currently best value in the database, and s is the root mean squared error (RMSE), $s = \sqrt{s^2}$. The improvement at a sampled location, where the response is already known and therefore no uncertainty exists ($s = 0$), is zero. Fig.3.2 shows the criterion for the same one dimensional function as for the prediction-based optimization. Visualized are again the real response (black line), the surrogate model (red line), the evaluated points (blue dots), the uncertainty (red shaded area), the acquisition function the optimizer maximises (blue line), and the new infill points (green). To obtain a new

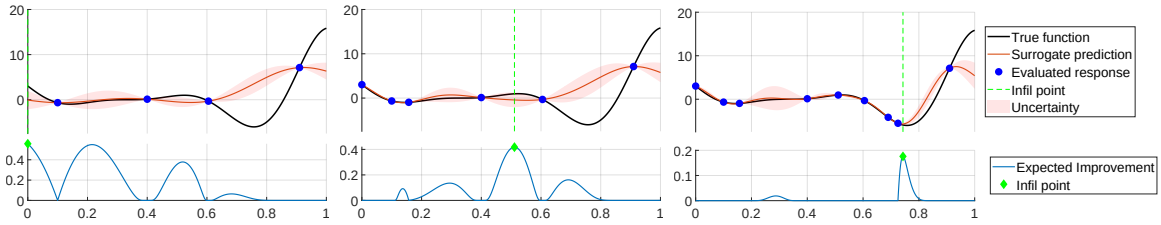

(a) Initial state (b) Optimization after two iterations (c) Optimization after five iterations

Figure 3.2: *Expected Improvement* infill criterion for an optimization process. The consideration of the uncertainty supports a balance between a global and local search to identify regions of interest

point, the criterion needs to be maximized or its negative value to be minimized. The zero value at the sampled points is clearly visible. Further, in some areas, where no improvement is expected, a low value separates those regions. With a progressing

sampling the regions of non-zero values become more narrow, making it possibly tougher for an optimizer to identify them. In the shown example, the optimizer is able to identify the region of the global minimum and progressing towards it.

3.3.2 Lower Bound

Other ways of considering the confidence interval of the prediction is the employment of a statistical lower bound, where with a fixed or adaptive multiplier the uncertainty is accounted for in the prediction [184], simply by subtracting the estimated error. It can be formulated as:

$$f_{Acq} = \hat{y}(\boldsymbol{x}^*) - \tau s(\boldsymbol{x}^*), \tag{3.17}$$

where τ is the multiplier specifying the magnitude of the estimated error (RMSE) considered. Therefore, throughout an optimization process, modifying τ can influence the balance between exploration and exploitation. Further, the error of the surrogate, locally and globally, will decrease and the second term will play a smaller role in the acquisition function. Fig. 3.3(a) visualizes the lower bound function based on the surrogate of the one dimensional function. As before, the real response is shown as black line, the surrogate model as red line, the evaluated points are blue dots, the uncertainty is visualized as red shaded area, the acquisition function the optimizer minimizes is the blue line, and the new infill points are represented by green diamonds and the dashed line. The criterion needs to be minimized to find an infill point. The

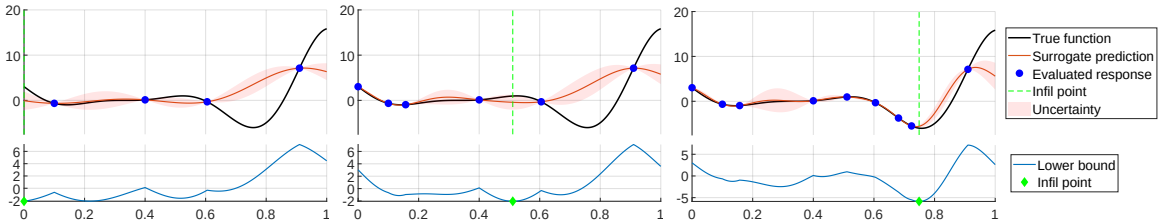

(a) Initial state (b) Optimization after two iterations (c) Optimization after five iterations

Figure 3.3: *Lower bound* infill criterion for an optimization process. The variable consideration of the uncertainty allows for an influence of exploration and exploitation

used uncertainty consideration in this simple example is $\tau = 1$. The global minimum is identified and the optimization is able to progress towards it.

3.3.3 Probability of Improvement

The *Probability of Improvement*, $P[I]$, is comparable to the $E[I]$, which expresses the likelihood that at a location $\boldsymbol{x}^*$ is an improvement. Opposing to the $E[I]$, no estimation is given on how much the improvement might be. The expression is given as:

$$f_{Acq} = P[I(\boldsymbol{x})] = \Phi\left(\frac{y_{min} - \hat{y}(\boldsymbol{x})}{\hat{s(\boldsymbol{x})}}\right), \tag{3.18}$$

with ϕ being the Normal cumulative distribution function. As the obtained values are small, especially later on in an optimization process, it is not a well suitable approach for most optimization cases [184]. A representation of the criterion in an optimization process is given in Fig. 3.4. The plotted data resembles the former representations, including the real response (black line), the surrogate model (red line), the evaluated points (blue dots), the uncertainty (red shaded area), the acquisition function the optimizer maximises (blue line), and the new infill points (green). The function

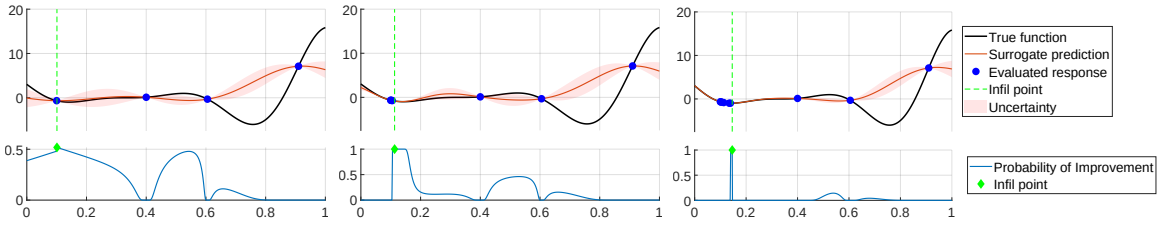

(a) Initial state (b) Optimization after two iterations (c) Optimization after five iterations

Figure 3.4: *Probability of Improvement* infill criterion for an optimization process. The optimizer needs to search for a maximum value, which can be a flat plateau (e.g. Fig 3.4(b)) and therefore not a distinct point

value needs to be maximized, alike to the expected improvement, to determine a new infill point. The rather sharp, almost discontinuous, trend visible in the initial state (Fig 3.4(a)), can make it more difficult to reliably identify the optimum. Further, for the shown function one can recognize a plateau in the intermediate state (Fig 3.4(b)), requiring either an interference of the applicant or an additional decision criterion. In the shown example the optimizer is not able to identify the region of the real global minimum ad rather searches around the determined local minimum. It also has regions of low value where some optimizer could have issues progressing and impeding the identification of the maximum.

3.3.4 Uncertainty-based Blends

Balancing the local and global search for an optimum value, Sasena et al. [217] analysed approaches proposed by Watson and Barnes [216]. Their strategies contain the search for finding the threshold-bound minimum (WB1), the regional minimum (WB2) and minimizing surprises (WB3), and were investigated together with a design space variance minimization. Of special interest in subsequent works is the WB2 criterion, stated as:

$$f_{Acq} = WB2 = \hat{y} - E[I], \tag{3.19}$$

which associates the mean prediction of the estimator ($\hat{y}$) with the expected improvement ($E[I]$), resulting in a more distinct function, which is more convenient to search with an optimization algorithm compared to the expected improvement alone (see Fig 3.2). This approach was extended to have a blend of the two terms to adapt better to the objective, named as WB2s [189]:

$$f_{Acq} = WB2s = \hat{y} - sE[I], \tag{3.20}$$

where s can be either a fixed value of be modified throughout the optimization process as proposed by Bartoli et al. [189], considering the magnitudes of $\hat{y}(\boldsymbol{x})$ and $E[I(\boldsymbol{x})]$. Fig. 3.5 shows the trend of this infill criterion. To identify a new sample point, the

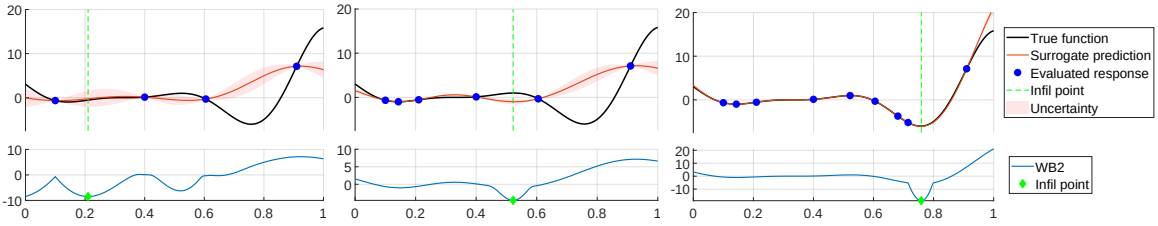

(a) Initial state (b) Optimization after two iterations (c) Optimization after five iterations

Figure 3.5: *WB2s* infill criterion for an optimization process with a fixed value for s ($s = 5$). The optimizer needs to search for a minimum value

function needs to be minimized. Compared to the aforementioned infill criteria, one can recognize a smoother trend over the entire design space, even though kinks are present, possibly jeopardizing gradient-based search methods. However, this "smoothness" gives it a favourable flavour for identifying the optimal point when searching for a new infill point. With the possibility to shift the blending between the estimation and the expected improvement term, some freedom is given in the exploitation and

exploration balance. In the presented example the optimizer is able to identify the region of the global optimum and to reduce the uncertainty in the regions of interest.

3.4 Constraint Consideration on the Basis of Uncertainty

Most engineering problems require the optimization of an objective while respecting equality or inequality constraints constraints, usually given as:

$$\begin{aligned} &\text{minimize} && y = f_{obj}(\boldsymbol{x}) \\ &\text{w.r.t.} && \boldsymbol{x} \\ &\text{subject to} && g(\boldsymbol{x}) \leq 0 \\ & && h(\boldsymbol{x}) = 0 \end{aligned} \tag{3.21}$$

If those constraints are expensive to evaluate, surrogate models can be used similarly as for the objective function. Often, the mean prediction is used to consider the meta model constraint [226].

The optimization problem posed as a SBO is then:

$$\begin{aligned} &\text{minimize} && \hat{y} = \hat{f}_{obj}(\boldsymbol{x}) \\ &\text{w.r.t.} && \boldsymbol{x} \\ &\text{subject to} && \hat{g}(\boldsymbol{x}) \leq 0 \\ & && \hat{h}(\boldsymbol{x}) = 0 \end{aligned} \tag{3.22}$$

where the real function evaluation is replaced by the approximations of the surrogate model ($\hat{f}_{obj}(\boldsymbol{x})$, $\hat{g}(\boldsymbol{x})$ and $\hat{h}(\boldsymbol{x})$). This approach is employed in the *Super Efficient Global Optimization* framework [249]. A challenge in optimization methods in general is the consideration of equality constraints [189]. Often, this kind of constraint is replaced by two inequality constraints close to the equality constraints, therefore allowing the optimizer more freedom.

In the initial phase of a SBO approach, as only few responses are evaluated, not a lot is known about the constraint function, possibly missing promising feasible areas in the design space and likely lacking accuracy [183; 250]. The mean predictions changes significantly throughout the optimization process, as the real function is not known a

priory. Further, alike to the direct minimization of the surrogate objective, the progress in gaining knowledge about the constraint function is slow. Therefore, considering the uncertainty of those models when searching for new sample points in the constraint problem enables the optimization to search the design space more thoroughly. On that account, different ways can be employed, explained in the following part.

As an additional remark, in following formulation statements the equality constraint is disregarded. Since for any optimization applications in this work no equality constraints were existing, this is seen as acceptable. Nevertheless, an equality constraint could be added without predicament if necessary.

3.4.1 Upper Trust Bound - UTB

As mentioned in the introduction, a strategy alike to the lower bound can be employed to relax the constraints in a model with uncertainty [251; 226; 227]. This allows for infill points to be spread out more widely in a more complex constrained function [217]. With the progressing optimization the uncertainty will decrease locally and finding feasible points improving the objective along constraints is more likely [226]. Thus, the constraints are relaxed by the uncertainty and more design space is available for the optimizer to explore, especially in the early stage of the optimization, when the surrogate model lacks accuracy due to scarce sampling. The optimization statement for this acquisition function is then:

$$\begin{aligned} &\text{minimize} && \hat{y} = \hat{f}_{obj}(\boldsymbol{x}) \\ &\text{w.r.t.} && \boldsymbol{x} \\ &\text{subject to} && \frac{\hat{g}_i(\boldsymbol{x}) - \tau_{UTB}\, s_{\hat{g}_i}(\boldsymbol{x})}{b_i} - 1 \leq 0 \end{aligned} \tag{3.23}$$

where $\hat{s}$ is the root mean squared error of the prediction, τ_{UTB} is the uncertainty consideration parameter, determining how much the constraint is relaxed, and b_i being the constraint value. This resembles a confidence interval of the constraint.

3.4.2 Probability of Feasibility - P[F]

Investigated by Sasena et al. [217] was the probability of feasibility as a constraint. Also, Forrester et al. [162] touch on the subject and give a short introduction to the process. Alike to the Probability of Improvement, a probability is estimated that the

constraint is below (or above) a constraint threshold.

Fig. 3.6 shows an artificial constraint function (black line) together with the evaluated points (blue dots) and the subsequently built surrogate model (blue line). Additionally, the arbitrary constraint value, that has to be surpassed, is shown as red line. As can be seen, the mean value of the prediction is unfeasible in the whole design space and an optimization would be unsuccessful to find a new point. Considering the uncertainty of the Gaussian process (red shaded area), one can compute the $P[F]$, shown in the second graph, and chances are that the (constraint) function will actually surpass the boundary, marked in the figure as gray areas.

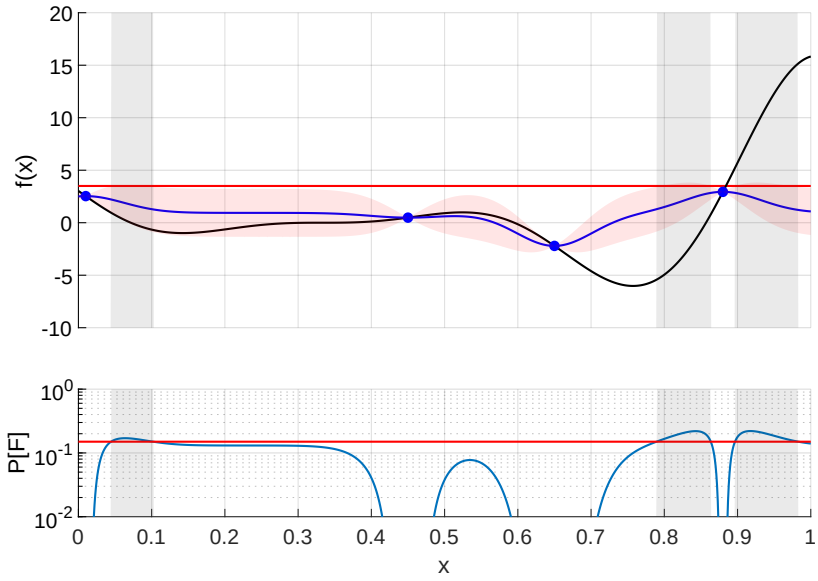

Figure 3.6: Visualization of the probability of feasibility for a surrogate constraint function (blue) with inequality (red) for an artificial constraint function (black)

With this property, the $P[F]$ can be used for inequality constraints, as they can be relaxed and therefore give the optimizer more freedom for searching for possibly feasible design areas. This, in turn, improves the exploration of the design space for feasible designs. For equality constraints, one creates two inequality constraints, generating a narrow bound in which the both constraints need to be fulfilled. Calculating a likelihood for a function being above a threshold is:

$$P\left[F\right] = \Phi\left(\frac{b - \hat{g}(\boldsymbol{x})}{\hat{s}(\boldsymbol{x})}\right), \tag{3.24}$$

with Φ being the Gaussian cumulative distribution function, $\hat{g}(\boldsymbol{x})$ is the predicted

value of the constraint surrogate, $\hat{s}(\boldsymbol{x})$ the predicted uncertainty at the corresponding sample point and b is the boundary of the constraint.

The optimization statement for this method can therefore be written as:

$$\begin{aligned} &\text{minimize} && f_{acq}(\boldsymbol{x}) \\ &\text{w.r.t.} && \boldsymbol{x} \\ &\text{subject to} && 1 - \frac{P\left[F(\boldsymbol{x})\right]}{\tau_{PFCON}} \leq 0, \end{aligned} \tag{3.25}$$

where τ_{PFCON} is the minimum probability value that needs to be exceeded by the constraint, considering the present uncertainty of a surrogate-based constraint. The value of τ_{PFCON} can be adapted in an iterative process, enabling an initial exploration (with a lower probability value) with an exploitation towards the final phase (with a higher probability value) of the optimization dependent on the maximum number of iterations.

To account for multiple constraints, one can either introduce multiple constraints or take the product of the probabilities for each constraint, resulting in a likelihood of all of them being fulfilled:

$$P\left[F\right] = \prod_{i=1}^{n} P\left[F\right]_i, \tag{3.26}$$

For the latter approach, however, one has to keep in mind that the values for each $P[F]$ is between zero and one and therefore the threshold (τ_{PFCON}) for the product might need to be adapted.

3.4.3 Normalized Probability of Feasibility - OFPF

The more common way and investigated method by Sasena et al. [217], Forrester et al. [162] and others [250; 225], is the use as a multiplier for the objective function. The probability of feasibility can be used to transform a constrained optimization to an unconstrained optimization, by multiplying its value towards the objective function:

$$\begin{aligned} &\text{minimize} && f_{obj}(\boldsymbol{x}) \quad = -f_{acq} \times P\left[F(\boldsymbol{x})\right] \\ &\text{w.r.t.} && \boldsymbol{x} \end{aligned} \tag{3.27}$$

In this approach all constraints are condensed into one probability value, mentioned before and calculated as in equation 3.26.

Together with the EGO approach as acquisition function ($f_{acq} = E[I]$), it showed applicability but had some issues with reaching constrained bounded minima [217]. Further, one would want to adapt the way of weighting, as already mentioned in [250], as the multiplication of $P[F]$ and $E[I]$ results in a Pareto front-like objective function.

The use with other acquisition functions is possible but has some limitations. Mentioned by Sasena et al. [217] is the possible issue of the multiplication of the estimated objective function $\hat{y}(\boldsymbol{x})$ by $P[F]$, if $\hat{y}(\boldsymbol{x})$ changes the sign. Therefore, a minimization does not necessarily lead to a successful infill criterion based optimized point. One can find ways to circumvent this issue with case sensitivity and an inverse use of the value of the $P[F]$, for instance as:

$$OF_{ucon} = \begin{cases} f_{acq} \times P\left[F\left(\hat{y}\right)\right] & \text{if } f_{acq} < 0, \\ f_{acq} \times \left(1 + \epsilon - P\left[F\left(\hat{y}\right)\right]\right) & \text{if } f_{acq} \geq 0. \end{cases} \tag{3.28}$$

where ϵ prevents the second multiplicand to become zero which would make the acquisition function value independent of the objective function value in the feasible region.

To circumvent the aforementioned issue, an approach is proposed to normalize the infill criterion term in the objective function. Additionally, it is proposed to embed the $P[F]$ in a sine function to strengthen lower probability values to shift to a greedier exploration. This can be especially helpful in the initial phase of an optimization process, when much uncertainty is still present in the surrogate model.

For the latter, to account more generously for the uncertainty in the constraint, a sine function can be used to value probabilities of high likelihood. Hence, the expression for the $P[F]$ is embedded in a sine function with an exponential parameter n in a multiplicative formulation for the unconstrained optimization. Here, the parameter n allows for an influence for the exploration and exploitation balance of the constraint surrogate with the considered uncertainty. The optimization statement with the new multiplier is then:

$$OF_{ucon} = f_{acq} \times \sin\left(P\left[F\left(\hat{y}\right)\right] \times \frac{\pi}{2}\right)^{n} . \tag{3.29}$$

Fig. 3.7 shows the influence of the exponent n in the $P[F]$ term and therefore how the objective and probability of feasibility functions are weighted together. In the mathematical test cases (section 3.6), a suitable value of n is explored, the more

favourable one was later used for the engineering application (section 4). A new

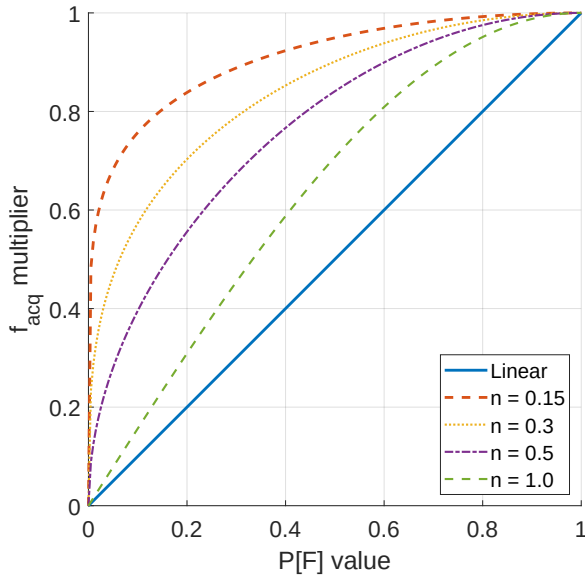

Figure 3.7: Transformation of the P[F] value to expand the multiplicative factor for the objective function value

possible issue, that needs to be further researched, is the magnitude of the different part of the new acquisition function. If, for instance, the prediction $\hat{y}(\boldsymbol{x})$ and the $E[I]$ differ distinctively in magnitude, a normalization may jeopardize this difference in scale and possibly lead to the wrong direction in the global search for the optimum. In the tested cases, this possible issue was not noticed so far, but was acknowledged for to be under further investigations for future applications

The normalization for the response values is a way to bypass the issue based on the sign of the infill criterion mentioned before. The normalized $WB2s$ criterion [189], based on the prediction ($\hat{y}(\boldsymbol{x})$) and Expected improvement ($E[I]$), is then always positive and multiplied as objective with the also always positive $P[F]$. Consequently, the predicted values are normalized in each iteration to reassure all values are in a bounded domain of $[0, 1]$. The new optimization statement is then a maximization of all components. As the boundaries are already considered with the ($P\,[F]$) multiplier in the OFPF method, this becomes the following unconstrained optimization problem:

$$\begin{aligned} &\text{minimize} \quad f(\boldsymbol{x}) \quad = -\left(\hat{y}_{norm}(\boldsymbol{x}) + E[I(\boldsymbol{x})]_{norm}\right) sin\left(P\,[F(\boldsymbol{x})]\,\frac{\pi}{2}\right)^{n} \\ &\text{w.r.t.} \qquad \boldsymbol{x} \end{aligned} \tag{3.30}$$

Independent of the used infill methodology, it should be noted that depending

on the constraint surrogate precision and the uncertainty, no feasible point can be identified within the constrained bounds by the optimizer. Here, an approach is to prioritize the improvement of the constraint function(s) with an unconstrained optimization to meet the boundary conditions. Using an acquisition function for searching within the constraints will support an initially poorly sampled design space to find feasible regions. Subsequently, as soon as area(s) of feasibility are identified, the primary optimization can continue.

3.5 Implementation and Integration of Surrogate Methods

For the implementation of Kriging and the integration in the MDO process, the MATLAB Kriging toolbox DACE [244] is employed, which is based on the work of Sacks et al. [182]. The integrated regression (constant, linear, quadratic) and correlation (Gaussian) models were used as well as the hyperparameter estimation based on a Hooke and Jeeves pattern search [252]. Additionally, adaptations were performed to enable an advanced and more suitable use of the toolbox. This includes the preparation for regression Kriging with the additional parameter λ for the correlation matrix. To obtain the value for λ the already implemented hyperparameter estimation is used. Further, functions were added to calculate the expected improvement and probability of improvement (also for the probability of feasibility) to be prepared for the MDO process.

The identification of new sample points to improve the design is then based on a search in the surrogate model. By replacing the expensive to evaluate real function with an inexpensive alternative, one can use an optimizer of choice to search the surrogate. Implemented in the presented methodologies are a gradient based optimizer and an evolutionary global optimizer. The first is the MATLAB internal "*fmincon*", a non-linear programming solver for multivariable functions with non-linear equality and inequality constraints [253; 254]. It employs sequential quadratic programming techniques with trust regions. As gradient based optimizer it might only be able to identify a local optimum, which requires a multi-start approach to increase chances of finding the global optimum. However, additionally a global search algorithm was set up to be used in the surrogate based search for a new infill point. The genetic algorithm implemented in MATLAB is employed in this case, which is based on

Goldberg [255]. As global optimizer the chances to identify the global optimum or a design close by are higher than for a gradient based optimizer. However, the expense for this higher probability of finding the region of the global optimum is a high number of function evaluations, related to the initial population, the maximum number of iterations and convergence criteria for fitness and constraint function values.

Despite the higher costs due to the number of evaluations for the genetic algorithm and the gradient based optimizer in a multi-start approach, the surrogate based optimization is a feasible approach as single evaluations are inexpensive. One can employ different infill criteria or change weightings in blends (e.g. WB2s or lower bound approach) to determine different infill points for a balanced exploitation and exploration. The new infill point is evaluated with the expensive solver, the surrogates are rebuild with the obtained response and the optimizer can be employed again to thoroughly search the surrogate for a new infill point.

While the emplyed tools for the multi-disciplinary analysis contain different levels of fidelity, one could consider to utilize it in a multi-fidelity surrogate modelling approach. However, it was decided not to apply it in the present work. This is due to the expected highly non-linear responses for the tools that were present at different levels of fidelity, namely the aerodynamic evaluations and the non-linear structural model considering geometric non-linearities. It was anticipated that the additional gain would be limited and the implementation and validation effort was not in the scope of the project time. With the developed methodology for the multi-disciplinary analysis, it can be of interest for future work to extend the capabilities and consider the different fidelity levels not only in the assessments, but also for the employed surrogate models.

In the following section, the applicability is shown based on mathematical test function. Later on, an aerodynamic shape optimization of a transonic airfoil demonstrates the proposed method in an engineering environment.

Another important aspect of the employed methodology, including surrogate-based optimization, multi-disciplinary analysis and multi-fidelity aspects, is the computational budget allocation strategy. This includes the available time and resources distributed towards the various performed computations. The problem specific allocation of computational budget is described in the corresponding problem statements. The strategies to obtain optimization results with limited computational resources is related to different rationality of the various problems.

In the novel infill criterion approach test cases, as described in section 3.6, and

its engineering application in chapter 4, the budget was determined by researched comparable works and the dimension of the problem. The amount of real function evaluations is related to the number of runs for and the duration of single evaluations to obtain results in reasonable time.

The allocated computational budged of the project related research, described in chapter 5 and chapter 6, was driven by the time frame of the project. Considering the dimensional size of the problem, implementation and integration of computational tools, convergence behaviour of the problem and encountered computational costs of single evaluations, the budget was determined appropriately and adapted to the corresponding situation. Short explanations are given in the respective descriptions.

3.6 Mathematical Test Cases for the Probability of Feasibility Approaches

To show the applicability of the proposed methods, mathematical test functions are considered as optimization problem. Their local and global optima are know, thus methods can be evaluated regarding their convergence, search behaviour and accuracy.

3.6.1 Two-dimensional Test function - Branin

The adapted Branin function [162] is used as a two-dimensional (2D) example with two different constraint cases, a simple constraint (hyperbolic) case and a heavily constrained case. The formulation of the Branin function is then:

$$f = \left(x_2 - \frac{5.1}{4\pi^2} + \frac{5}{\pi}x_1 - 6\right)^2 + 10\left[\left(1 - \frac{1}{8\pi}\right)\cos x_1 + 1\right] + \frac{5x_1 + 25}{15}, \tag{3.31}$$

with $x_1 \in [-5, 10]$ and $x_2 \in [0, 15]$. For the process, the design variables are normalized in the design space. The simple constraint is an inequality product of the two design variables with a threshold of $g \geq 0.2$ and therefore:

$$0.2 - x_1 x_2 \leq 0, \tag{3.32}$$

where $x_1, x_2 \in [0, 1]$. The more complex constraint is a multi modal function, mentioned in [217] and used as well in other surrogate optimization methodology problems, such

as in [250] and [227]. It is formulated as:

$$\begin{aligned} g(\boldsymbol{x}) =& 4 - \left(4 - 2.1(2x_1 - 1)^2 + \frac{(2x_1 - 1)^4}{3}\right)(2x_1 - 1)^2 \\ & - (2x_1 - 1)(2x_2 - 1) - 16(x_2^2 - x_2)(2x_2 - 1)^2 \\ & - 3\sin[12(1 - x1)] - 3\sin[(1 - x_2)], \end{aligned} \tag{3.33}$$

with $x_1, x_2 \in [0, 1]$ and $g \geq 0$. Fig. 3.8 shows the objective function with the simple (3.8(a)) and the complex (3.8(b)) constraints.

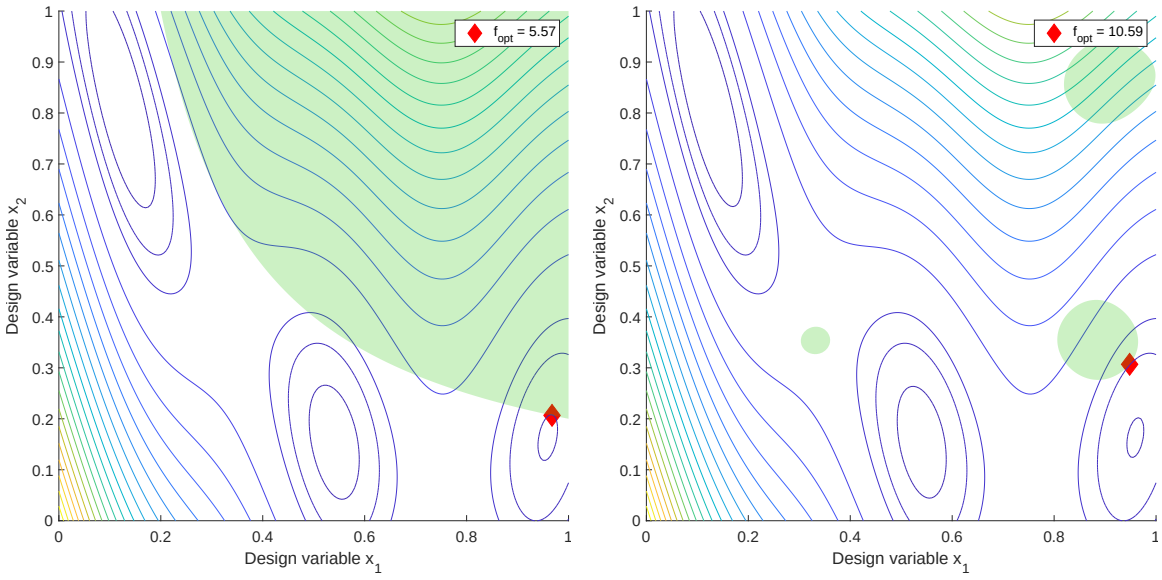

(a) Branin function with the simple constraint

(b) Branin function with the complex constraint; the feasible regions are disconnected

Figure 3.8: Adapted Branin function with simple (a) and complex (b) constraint; the contour lines depict the objective function value, where blue are lower (better) values; the green shaded area represents the feasible region;

The used methods for the problems are the probability of feasibility as an independent constraint (PFCON), the probability of feasibility as a multiplier for the normalized objective function (OFPF) and the upper trust bound approach (UTB) as comparison. For both test cases an initial sample of 5 points is used, distributed over the design space with a Latin Hypercube Sampling (LHS) [175]. To eliminate some of the randomness of the initial sampling, 50 runs are executed with different initial samples. The number of maximum iterations is set to 25 for the simple constraint and 30 for the more demanding constraint. The $\alpha WB2$ infill criterion is used for identifying new infill points, where α is set to 10 for all methods and τ for the UTB and the

PFCON is explored with different values. The optimization is terminated prematurely if a new design point is in a close vicinity of the real optimal point. This relates to a distance of $d < 0.005$ and $d < 0.01$ for the simple and demanding constraint, respectively. To find new sample points the genetic algorithm (GA) implemented in MATLAB [255] is used to search the surrogate models. Adapted from the default values are the function and constraint tolerances (both $1e-8$), the population size (100 $\times$ number of design variables) and the initial population contains the DoE samples. The new design is then added to the existing samples and the surrogates are updated in each iteration.

Depending on the existing samples within a run and the quality of the built surrogate model(s) for the constraint(s), no feasible solutions might exist. Therefore, the GA is unable to find a new design site that satisfies the surrogate constraint [1]. For this case, a secondary optimization was introduced with the purpose of improving the constraint surrogate, as mentioned beforehand. With an expected feasibility approach a new sample point was generated to find feasible regions in the constraint.

Fig. 3.9 shows the convergence progress throughout the optimization for the simple (3.9(a)) and the complex (3.9(b)) constraints. Visualized are the mean value of the currently best objective function value for different parameters for the respective approach. To provide a complete impression of the analysis of all executed runs, Fig. 3.10 shows the mean value of the currently best objective function value as lines as well as the standard deviation as shaded areas for the applied methods. To allow for an easier perception of the results, each method is shown in their own graph with two different color schemes. For the simple as well as for the demanding constraint, the OFPF has the best performance for this example for both chosen exponent parameter (n). In case of the more restricted boundary, a difference for the tuning parameter is noticeable for the convergence speed as well as the convergence success. For this reason, the parameter n was set to a more favourable value ($n = 0.15$) for the higher dimensional cases. However, the global optimum could be identified with admissible accuracy.

The UTB has a similar performance for the simple constraint, but for the second case converges only similarly for a lower value for the uncertainty consideration ($\tau_{UTB} = 1$). While for both constraint cases in the initial phase of the optimization the success is dependent on the initial samples, for the simple constraint almost all

[1] For the OFPF this happens less likely but can still occur as the change in objective is small from generation to generation.

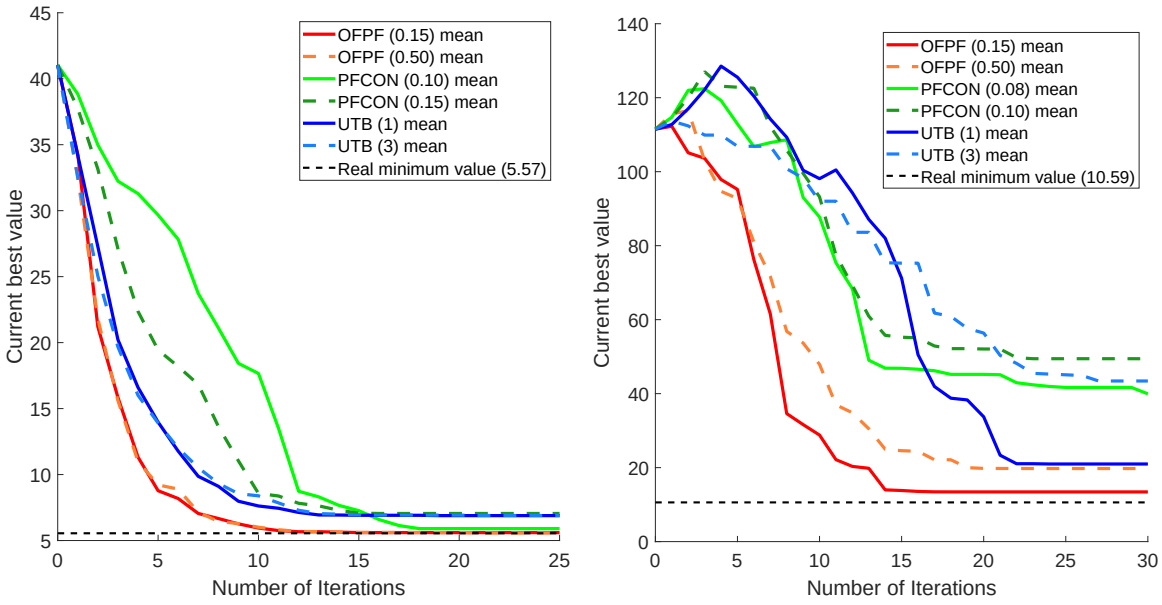

(a) Convergence for the simple constraint for the search methods

(b) Convergence for the narrow constraint for the search methods

Figure 3.9: Convergence for the different search methods and tuning parameters for the Branin function

runs are able to converge towards the global optimum, visible in the low standard deviation in Fig. 3.10(e) For the second constraint case, the deviations between the single runs are higher after the maximum number of iterations, as can be noticed in the standard deviation in Fig. 3.10(f). Since for one of the parameters the method obtained significant better results, it was chosen for later optimizations.

The PFCON takes the longest time to converge for the simple constraint, but is able to reach the vicinity of the global optimum slightly more often than the UTB, as shown in Fig. 3.10(c). For the more demanding constraint, the performance of the PFCON is considerably worse than the other two methods. Almost independent of the investigated parameter for the method, it displays a high deviation in achieving the optimum design, shown in the deviation of the best found point in Fig. 3.10(d). Tuning the constraint parameter for the uncertainty consideration (τ_{PFCON}) can possibly improve the convergence behaviour but was not considered here.

Table 3.1 summarizes the results for the two 2D test functions. The values for the UTB and PFCON method are the success rate for the parameter variation.

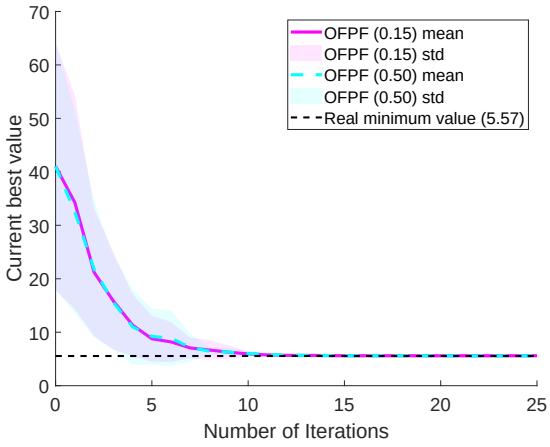

(a) OFPF with simple constraint

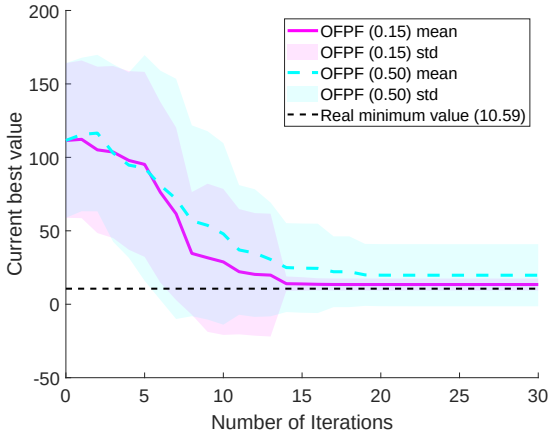

(b) OFPF with complex constraint

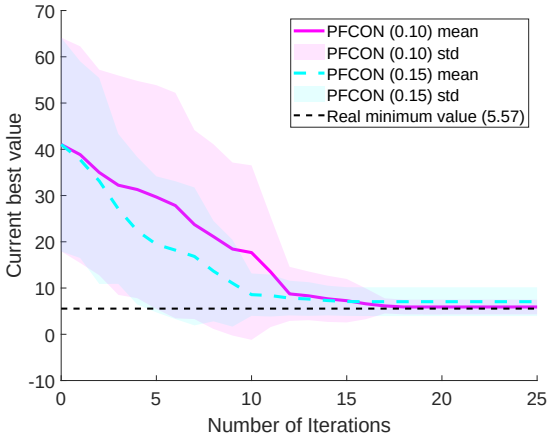

(c) PFCON with simple constraint

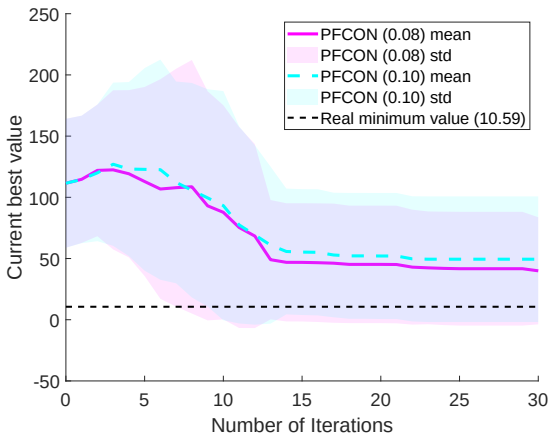

(d) PFCON with complex constraint

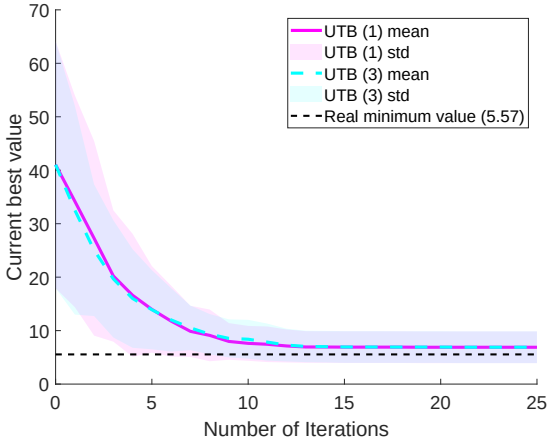

(e) UTB with simple constraint

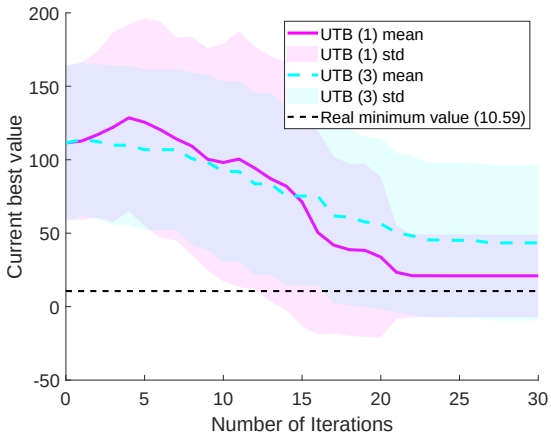

(f) UTB with complex constraint

Figure 3.10: Convergence for the different search methods and their tuning parameters with their respective standard deviation for the executed runs for the Branin function

Method	Simple constraint		Demanding constraint	
	Average Iterations	Success rate [%]	Average Iterations	Success rate [%]
UTB	16.5 & 18.0	84 & 82	22.8 & 23.3	54 & 40
PFCON	18.0 & 17.1	96 & 82	26.9 & 27.0	48 & 48
OFPF	15.1 & 16.5	100 & 100	21.5 & 23.5	80 & 64

Table 3.1: Performance of the 2D test case results

3.6.2 10-dimensional Test function - Stepped Cantilever Beam Design

A higher dimensional test function is used to show the applicability of the proposed methods towards higher dimensional problems. This test function, an engineering problem for a stepped cantilever beam design, is published in [256] and used as test case, for instance, in [257]. The mass is to be minimized, while constraints are related to the maximum bending stress, the aspect ratio of the segments and the maximum displacement under a given load. This example has a linear objective function, while the constraint functions are partially highly nonlinear. The formulation of the objective function is:

$$m = \rho(b_1 h_1 l_1 + b_2 h_2 l_2 + b_3 h_3 l_3 + b_4 h_4 l_4 + b_5 h_5 l_5) \tag{3.34}$$

with the length l_i, the height h_i and the width b_i of each segment i. ρ is the density of the material and the mass m the objective. The design variables are the width and height of the segments, while the lengths are evenly distributed over the whole length

$(500cm)$. The constraints are the following:

$$
\begin{aligned}
g_1(x) &= \frac{6Pl_5}{b_5h_5^2} - 14000 \leq 0 \\
g_2(x) &= \frac{6P(l_5+l_4)}{b_4h_4^2} - 14000 \leq 0 \\
g_3(x) &= \frac{6P(l_5+l_4+l_3)}{b_3h_3^2} - 14000 \leq 0 \\
g_4(x) &= \frac{6P(l_5+l_4+l_3+l_2)}{b_2h_2^2} - 14000 \leq 0 \\
g_5(x) &= \frac{6P(l_5+l_4+l_3+l_2+l_1)}{b_1h_1^2} - 14000 \leq 0 \\
g_6(x) &= \frac{Pl^3}{3E}\left(\frac{1}{\frac{b_1h_1^3}{12}} + \frac{7}{\frac{b_2h_2^3}{12}} + \frac{19}{\frac{b_3h_3^3}{12}} + \frac{37}{\frac{b_4h_4^3}{12}} + \frac{61}{\frac{b_5h_5^3}{12}}\right) \\
g_7(x) &= \frac{h_5}{b_5} - 20 \leq 20 \\
g_8(x) &= \frac{h_4}{b_4} - 20 \leq 20 \\
g_9(x) &= \frac{h_3}{b_3} - 20 \leq 20 \\
g_{10}(x) &= \frac{h_2}{b_2} - 20 \leq 20 \\
g_{11}(x) &= \frac{h_1}{b_1} - 20 \leq 20
\end{aligned}
\tag{3.35}
$$

where P is the applied load, E is the Young's modulus.

The initial sample, generated as a Latin Hypercube, consists of 11 samples ($n_{DVs}+1$). Subsequently, all the samples are normalized within the design space for the OFPF approach. Each iteration within the optimization process, this normalization has to be reevaluated, in case higher or lower responses are received. To circumvent the influence of the initial sampled values, the test case was run 50 times for each method with the same initial samples for the three of them. Fig. 3.11 shows the mean optimal value of the optimization for the 50 runs of the different methods as well as the standard deviation for those runs. All approaches have two distinct runs with different parameters to be compared in a better manner with each other. Due to the multiple constraints, there is a high probability the initial samples are all unfeasible and the first iterations will have high objective values to get an initial feasible design. As long as no feasible design is present, the "best" design is the one with the highest

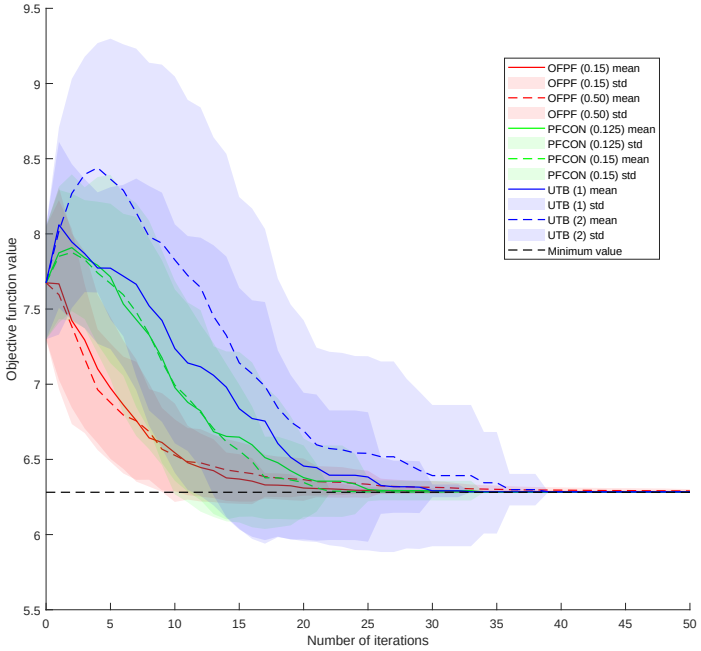

Figure 3.11: Convergence for the 10D test function for the different methods

objective function value. This allows the $\alpha WB2$ more freedom in the design space exploration. The resulting increase is visible in the convergence graph as the initial increase in the objective function value.

For both OFPF cases, it is visible that within the first 25 iterations the objective function value is minimized towards the optimal solution with a significant reduction of the standard deviation (shaded area). For the exponent $n = 0.15$ all runs achieve a final solution within less than 1% difference of the optimal value, while for a value of $n = 0.5$ 90% of the runs reach the real minimum. For the latter however, all optimizations exhibit a normalized distance from the optimum of less than 1% from the optimal design site, which was a convergence criterion. Given the results for the two test cases, the parameter n was set to the more favourable value ($n = 0.15$) for the following engineering application cases.

The UTB as well as the PFCON are initially exploring the design space, leading to an increase in objective function value. After some iterations the objective is decreasing drastically. Given the performance of the two methods in the test functions, the parameters were chosen accordingly for the engineering application .

For the test functions evaluation, the OFPF was found to be reliable, robust and fast, reaching the known global optimum with a high likelihood (between 80% and 100%). The PFCON performed well for the simple case and was comparable to an

upper trust bound approach. However, for higher complexity problems it was not as robust and reliable as the other approaches.

Chapter 4

Aeronautical Application of the proposed Probability of Feasibility Approach

In the following chapter two aerodynamic test cases are studied for the applicability of the proposed method for a surrogate based optimization. This single discipline (aerodynamics) aeronautical problem is a way to show the relevance of the approach in future optimizations, where surrogate based optimization can be employed. Infill criteria based on the probability of feasibility are herein employed to optimize a two dimensional transonic airfoil. This includes the approach with a normalization of the objective function to then account for the constraints and to use the probability value as a constraint.

The strategy is compared against a more established upper trust bound methodology for constraint consideration. Conclusions are drawn regarding the applicability, strengths and weaknesses of the approach. For both cases, an airfoil optimization under transonic speed conditions is performed. The baseline airfoil is the RAE2822, which is commonly used to test optimization algorithms in aerospace engineering, e.g. [168; 258; 163; 201], given the existence of experimental wind tunnel data [242]. This chapter contains modified excerpts from the article “Surrogate-based Optimization based on the Probability of Feasibility [229]. The content is elaborated in the scope of the present thesis.

4.1 Problem Description

The objective of the aerodynamic optimization is the reduction of the drag coefficient (C_d) subjected to an aerodynamic constraint of a lift coefficient (C_l) and a geometric constraint of a minimum thickness. The first case (Case 1) considers steady compressible Euler equations [259] to model the flow and therefore disregards viscosity. In the more challenging second case (Case 2), the steady compressible RANS equations [259] are employed to additionally account for viscosity. Both cases are exposed to a steady flow under a fixed angle of attack and pressure and density resembling an atmospheric condition at an altitude of 11,000m. The flow conditions considered for the two cases are summarized in Table 4.1. The shape of the airfoil is characterized with eight design variables.

Boundary condition	Case 1	Case 2
Mach number Ma [-]	0.734	0.729
Angle of attack α [deg]	2.79	2.31
Ambient pressure p_∞ $[Pa]$	28,745	28,745
Ambient density ρ_∞ $[kg/m^3]$	0.44	0.44
Speed of sound a_∞ $[m/s]$	301.86	301.86

Table 4.1: Flow conditions for the two airfoil optimization cases

Case 1 has five different initial samples, while Case 2 has only one initial sampling due to limited computational resources. Therefore, the results give a glimpse about the convergence behaviour. With a different initial set of samples, differences are expected as could be seen already in the mathematical test cases.

4.2 Airfoil Geometry Parameterization

To generate airfoil geometries, the Class Shape Transformation (CST) parametrization [260; 261] is used. Consisting of a class and a shape function, the airfoil geometry is defined as:

$$y_{cs}(\boldsymbol{\psi}) = c(\boldsymbol{\psi})\ s(\boldsymbol{\psi})\ , \tag{4.1}$$

with the class function c defined as

$$c_{n_1}^{n_2}(\boldsymbol{\psi}) = \Psi^{n_1}(1-\boldsymbol{\psi})^{n_2}, \tag{4.2}$$

where the indices n_1 and n_2 are set to 0.5 and 1.0, respectively. These parameters define a shape with a round-nose leading edge and a sharp trailing edge. The shape function s is defined as:

$$s(\boldsymbol{\psi}) = \sum_{i=0}^{n} \beta_i \, \boldsymbol{\psi}^i, \tag{4.3}$$

with β_i being the coefficients of the n-order Bernstein polynomials. With an order of 3, and a separated upper and lower surface polynomial, the number of design variables is then 8, with 2 $(n_s + 1)$. To generate the RAE2822 airfoil from the parametrization, a least square method was applied to estimate the closest possible shape resembling the RAE2822. Fig. 4.1 shows the original and the approximated shape, obtained via a minimum least square method. As can be seen, the upper surface is matched closely,

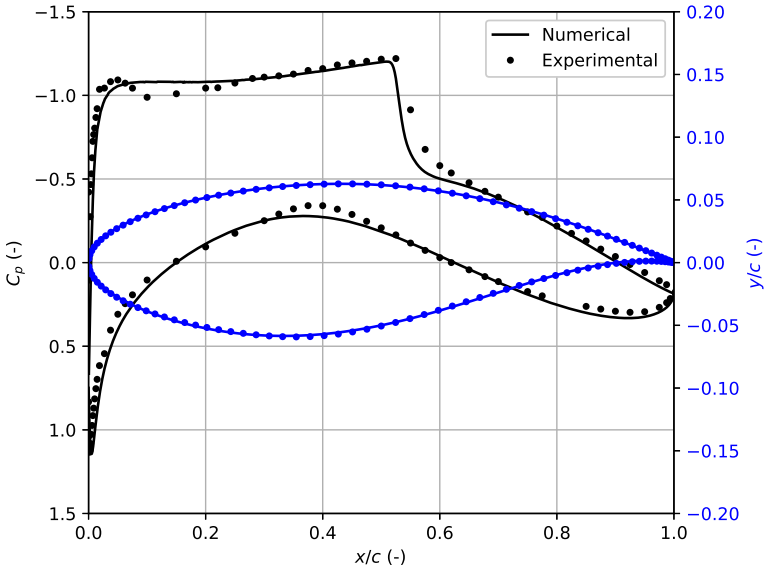

Figure 4.1: Shape matching (in blue) between the experimental RAE2822 airfoil (blue dots) and the numerical CST approximation (blue line) and comparison of pressure coefficient C_p distribution (in black) between CFD (black line) and experimental data (black dots) from [242]

while the lower surface has some deviation in the curvature at the leading and trailing edges. However, as the most influencing part to the evolving wave drag is developing on the upper surface, it is accepted as suitable for this application. Furthermore, for the aerodynamic mesh chosen for the RANS simulations (Case 2) the coefficient of pressure C_p distribution compares well with the experimental data from AGARD [242] as shown in Fig. 4.1.

4.3 CFD Modelling

For the inviscid test case (Case 1), a C-type mesh comparable to the one from Renganathan et al. [163] is generated, with a mesh size of around 50,000 cells. A refinement box is generated around the airfoil to capture the shock. The mesh generation is done by the CFD tool, where the maximum cell size in the fluid volume and the surface cell size on the boundaries (inlet, outlet, airfoil) are defined. No further actions were carried our regarding surface expansion for this case.

A convergence study was performed to obtain suitable mesh and refinement sizes. Table 4.2 displays the values acquired from the numerical runs for 3 different meshes. The lift represents the airfoil surface forces perpendicular to the flow direction, while the drag force is the component parallel to the flow. With an asymptotic convergence and a relative difference of less than 1% for both lift and drag coefficients, the medium mesh is seen as a good compromise between accuracy and computational time.

	Number of cells	C_l [-]	C_d [drag counts]
Coarse	6,766	1.028	260.7
Medium	42,877	1.046	249.0
Very fine	427,132	1.050	248.6

Table 4.2: Mesh convergence for the inviscid airfoil optimization problem (Case 1)

The same procedure was applied for Case 2. However, in this case the number of cells required to converge the mesh is higher as one can note from Table 4.3. This is

	Number of cells	C_l [-]	C_d [drag counts]
Coarse	64,995	0.8467	186.6
Medium	127,521	0.8087	177.2
Fine	198,438	0.8049	176.7

Table 4.3: Mesh convergence for the viscid airfoil optimization problem (Case 2)

due to the fact that now viscosity is being considered, thus a higher detail is given to the boundary layer region where a prismatic layer was included (see Fig. 4.2). The expansion of the surface cells is defined here by a thickness to capture the visous boundary layer and a number of layers. The cell size around the airfoil was chosen to respect a maximum y^+ value of 1. Additional refinements were added for this purpose around the leading and trailing edge, defined as circles to ensure a proper cell size.

For the same reasons as before, the medium mesh is selected for the optimization

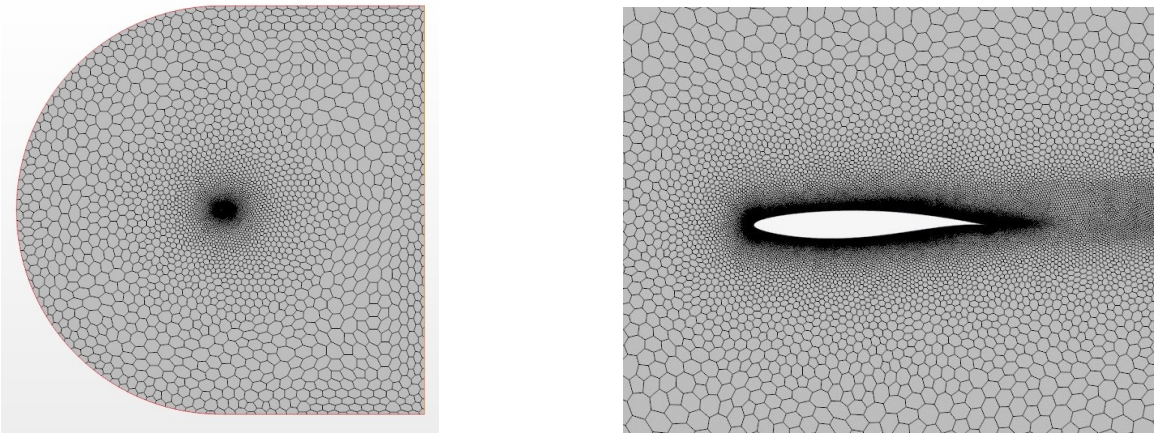

(a) Mesh (b) Refinement Region

Figure 4.2: CFD mesh defined for the numerical simulations with the full fluid volume (a) and the detailed view of the refinement region near the airfoil(b) for the viscous case

process. This mesh was also compared with experimental data from AGARD [242]. From this comparison, depicted in Fig. 4.1 and mentioned earlier, one can note a good agreement between experimental and numerical results. Furthermore, in terms of lift and drag coefficients the selected mesh also compares well with experimental [242] data for the same flow conditions as can be seen in Table 4.4. The slight difference can be explained by the small outer shape deviation due to the parametrization via CST.

	C_l [-]	C_d [drag counts]
Present Work	0.7417	120.1
Experimental [242]	0.7436	127.0

Table 4.4: Comparison of the obtained lift and drag coefficients with experimental data for the RAE2822 baseline

The resource for the computation is a personal computer with a AMD Ryzen 9 3900X 12-Core Processor with 3.79GHz and 32Gb of RAM. This leads to a performance of 5-10 minutes for a single inviscid calculation (Euler) and 20-30 minutes for a viscous solution (RANS), both including the surrogate building and search per iteration. Considering the different cases and methods, the raw computational time for the executed runs is around 125 processing hours.

4.4 Case 1 - Inviscid CFD

The objective of this first test case is to minimize the drag coefficient C_d for the prescribed flow conditions, while ensuring a lift coefficient C_l greater than 1.0. To accomplish this the vector of design variables $\boldsymbol{x}$ consists of the 8 parameters earlier defined for the CST parametrization technique. Two different variations are studied. In the first one, no geometry constraint is applied to the airfoil. While in the second one, the airfoil is subjected to two thickness constraints placed at 25% and 75% of the chord to impose a wing-box region. The optimization statement for these two variations of Case 1 are shown in Equations 4.4 and 4.5, respectively.

$$\begin{aligned} &\text{minimize} && C_d(\boldsymbol{x}) \\ &\text{w.r.t.} && \boldsymbol{x} \\ &\text{subject to} && C_l(\boldsymbol{x}) \geq 1.0 \end{aligned} \tag{4.4}$$

$$\begin{aligned} &\text{minimize} && C_d(\boldsymbol{x}) \\ &\text{w.r.t.} && \boldsymbol{x} \\ &\text{subject to} && C_l(\boldsymbol{x}) \geq 1.0 \\ & && t_{0.25c}(\boldsymbol{x}) \geq t_{0.25c_{\mathrm{RAE2822}}} \\ & && t_{0.75c}(\boldsymbol{x}) \geq t_{0.75c_{\mathrm{RAE2822}}} \end{aligned} \tag{4.5}$$

For this engineering application, as computational budget was limited, one run was performed with 100 iterations and four additional runs with only 50 iterations. Hereby the iterations are related to the real function evaluations. Within a single iteration, the surrogate model is searched by a genetic algorithm to determine the next infill point. With the inexpensive to evaluate surrogate model, the size of the population could be set to a high value of 400 to increase the likelihood of finding the location of the maximum fitness function value. The responses of the real function evaluation were a part of the initial population set.

The objective of the first run was to investigate if convergence is achievable within a given reasonable computational time. Given the fact that the global minimum is not known, it is difficult to predict convergence. Furthermore, it is expected that due to the nonlinearity of the Euler equations and the global influence of the design variables, the response function is also highly nonlinear, if not even multi-modal. As for meta models in general, the whole design space would have to be sampled to assure the global minimum is the one found.

The purpose of the four additional runs were to study the influence of the location of the initial values, which should be reduced. However, it is hard to eliminate the influence completely and possibly one specific set of initial samples might favour one method over the other. A more profound analysis would be needed to mitigate those effects.

Fig. 4.3 shows an exemplary iterative process of the optimization without the wing box constraint, for the drag coefficient (upper graphs) and the lift coefficient (lower graphs) with the UTB, PFCON and OFPF strategies (left, mid and right, respectively) for the 100 iterations case. In Fig. 4.4 the optimization iterations are shown for the

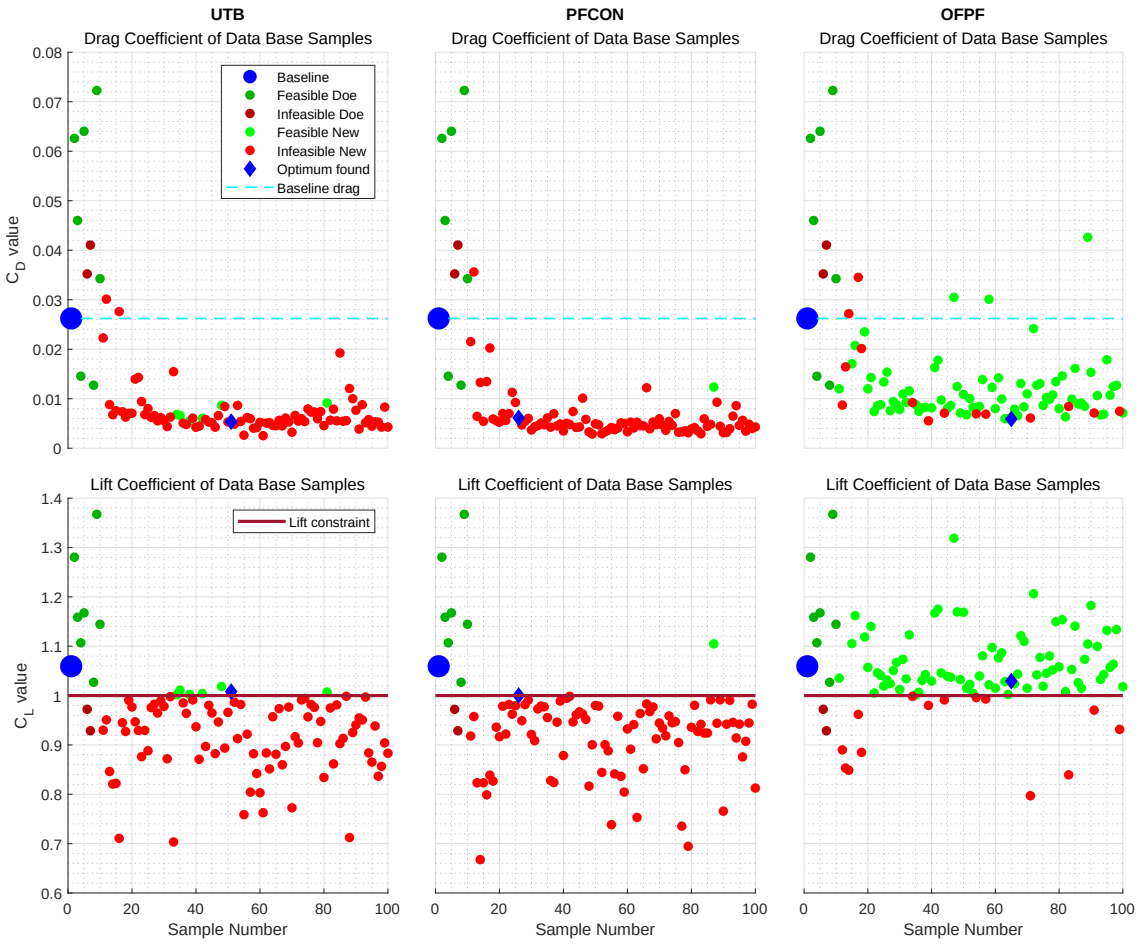

Figure 4.3: Convergence results of the inviscid optimization (Case 1) with the lift coefficient constraint only for the three tested methods (UTB, PFCON and OFPF in the left, mid and right graphs, respectively)

considered lift coefficient and wing box constraints. In these graphs, the baseline is represented as blue circles, feasible data as green circles and infeasible data as red

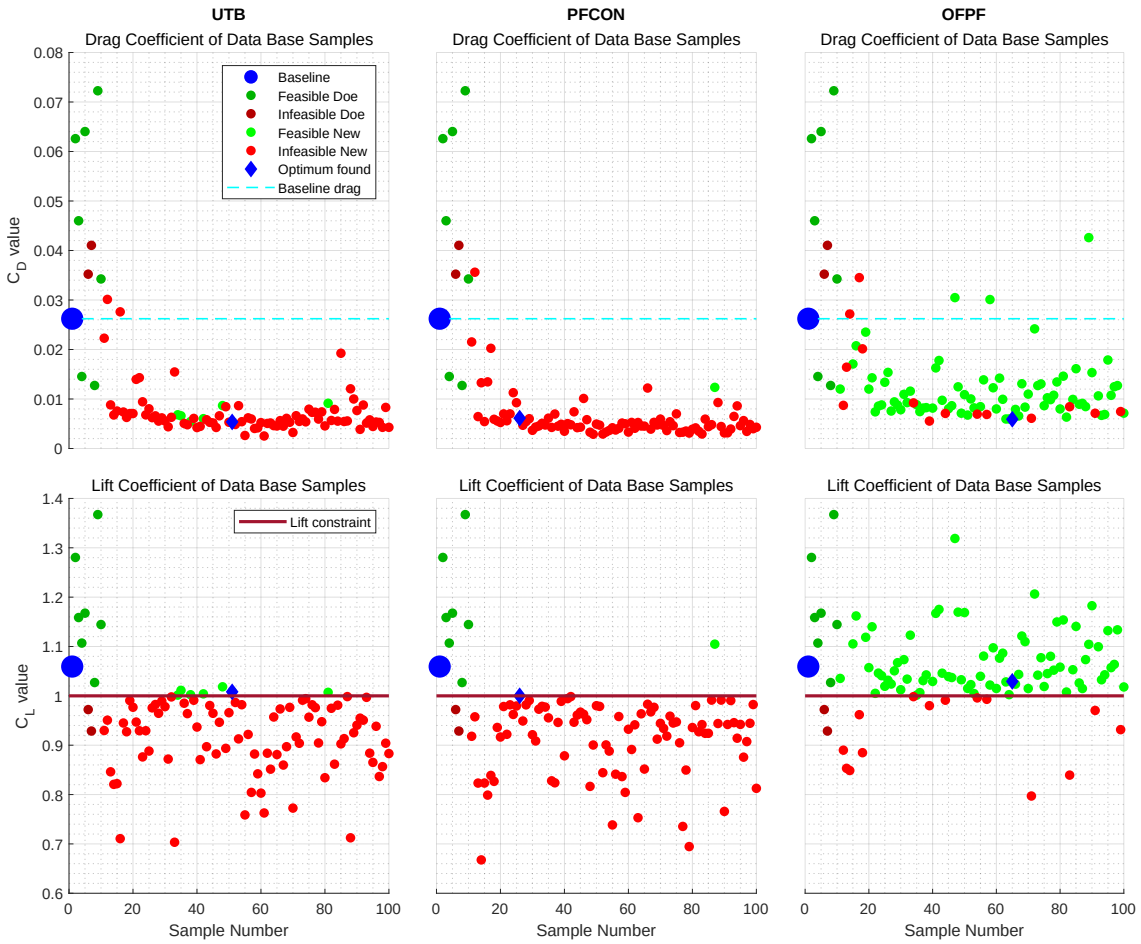

Figure 4.4: Convergence results of the inviscid optimization (Case 1) with the wing box constraint for the three tested methods (UTB, PFCON and OFPF in the left, mid and right graphs, respectively)

circles. The light blue line illustrates the baseline drag value as comparison. The dark red line in the lower graphs represents the imposed lift constraint. Green coloured points represent results that fulfill the constraints, while red points represent infeasible designs. If during the process a proposed infill point is evaluated and not feasible, the response is still added to the data set, the surrogate model is updated and the search for a new infill point happens on the updated model.

It is worth to note that for the OFPF method, more feasible designs are explored, closing to the boundary from the valid region of the boundary. In the same way as the lower bound, many of the samples are close to the feasible region but do not fulfill it completely. This is due to the fact that the bound is given a wide threshold to explore around the boundary and overstep it more often. Regarding the results,

all three methods improve the initial configuration significantly if 100 iterations are performed (drag reductions greater than 75%), as can be seen in Table 4.5. The best result without the geometric constraint is obtained from the UTB, followed by the OFPF and the PFCON. With the wing box constraint, the PFCON obtains the best result closely followed by the UTB and the OFPF. For both constraints, the PFCON generates the design closest to the C_l boundary. As seen before, for the UTB and the PFCON many of the obtained results are in close infeasible proximity, showing that the process is not converged yet and an exploratory phase is ongoing. However, due to the limited computational resources the number of iterations was limited and the goal was to reduce the drag within the given time.

	C_l constraint			C_l + WB constraint		
	#	C_l [-]	C_d [drag counts]	#	C_l [-]	C_d [drag counts]
Baseline	-	1.0594	262.2	-	1.0594	262.2
UTB	51	1.0082	53.7	36	1.0126	62.1
PFCON	26	1.0001	61.4	78	1.0096	58.9
OFPF	65	1.0293	59.1	87	1.0194	63.2

Table 4.5: Results of airfoil optimization with the three search function for Case 1with a budget of 100 iterations (inviscid)

Four other runs were performed, with a budget of only 50 iterations to limit the computational cost. Furthermore, the benefit of running 50 more iterations was not clear, as can be seen in Fig. 4.3 and Fig. 4.4. Table 4.6 shows the result for all runs up to 50 iterations and the best obtained result up to that point. Further, the average value of C_d throughout the 5 runs is shown. As can be seen, the UTB and the OFPF

	C_l Constraint			C_l + WB constraint		
	UTB	PFCON	OFPF	UTB	PFCON	OFPF
Run 1	54.5	61.4	71.3	62.1	66.8	84.8
Run 2	50.3	67.5	52.8	76.8	69.1	54.0
Run 3	54.8	61.3	53.3	90.4	62.2	88.2
Run 4	73.5	59.2	59.5	54.3	57.4	79.0
Run 5	47.2	60.7	44.6	71.1	80.1	67.4
Average	56.1	62.0	56.3	70.9	67.1	74.7

Table 4.6: Best results obtained for the performed five runs for the three methods with the two constraints.

perform quite similar, while the PFCON results for the geometrically unconstrained run is the least benefit, while for the wing box constraint it results in the best average design. Additionally, it should be noted that the best overall designs are all obtained with the OFPF method.

It is clear that all three methods are able to reduce the objective distinctively. Improvements are on average in the range between 76% and 79% for the unconstrained geometry and between 71% and 75% when the geometric constraint is considered. Fig. 4.5 compares the results for the pressure distribution of the baseline airfoil with the optimized results, using the PFCON, UTB and OFPF. For all three results

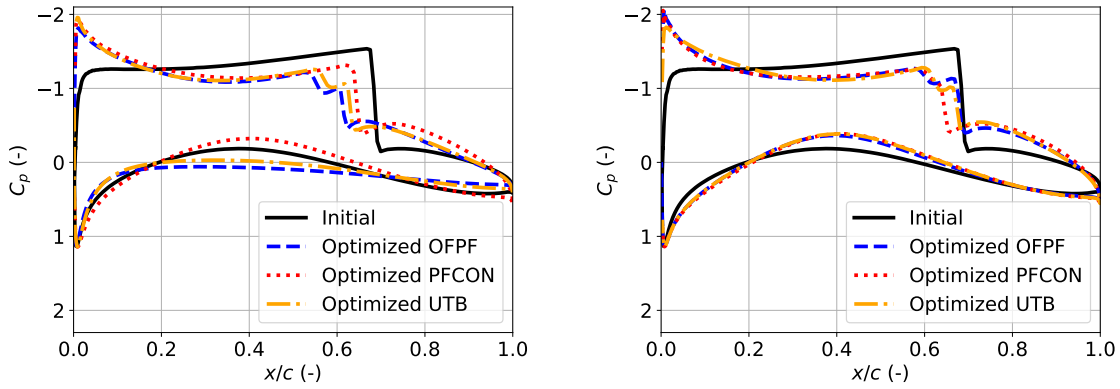

(a) C_p distributions for C_l constraint

(b) C_p distributions for C_l and geometric constraint

Figure 4.5: C_p distributions of the baseline and the optimized airfoils for the best obtained results in Case 1 (inviscid) without and with wing box constraint (left and right graphs, respectively), considering the three search methods

some significant trends can be observed. While the shock strength is reduced and shifted slightly forward to reduce the wave drag, an increase in pressure coefficient at the leading edge supports the necessary minimum lift requirement. The initial and optimized airfoil shapes are plotted in Fig. 4.6 to help understand the changes in pressure distribution along the chord. Despite assuming different values for the design variables as can be seen in Fig. 4.7, the three search functions follow the same approach to minimize drag, i.e. to increase the leading edge radius to accelerate the flow at that region and decrease the strength of the shock, accompanied by a thickness reduction. Those results indicate that regions of local minima in a shallow multi-modal designs space are found. Given the high minimum prescribed lift coefficient it is not possible to soften further the shock wave, as observed in Case 2 for a lower lift coefficient

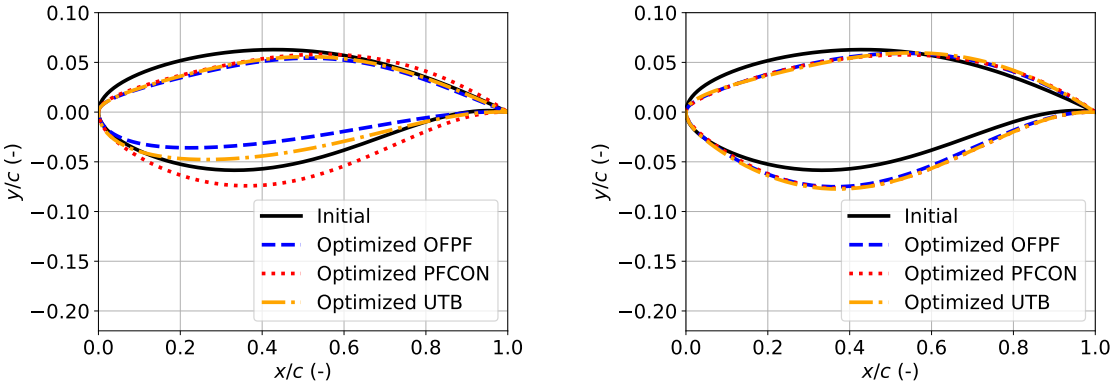

(a) Airfoil shapes for C_l constraint

(b) Airfoil shapes for C_l and geometric constraint

Figure 4.6: Airfoil shapes of the RAE2822 baseline and the optimized airfoils for the best obtained results in Case 1 (inviscid) without and with wing box constraint (left and right graphs, respectively), considering the three search methods

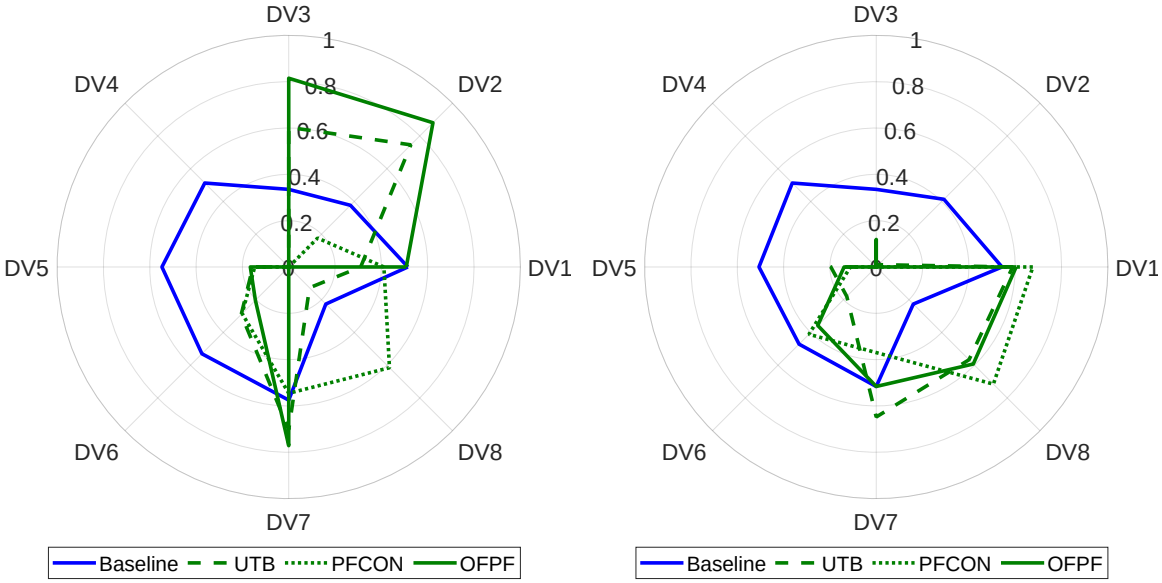

(a) Normalized design variables for C_l constraint

(b) Normalized design variables for C_l and geometric constraint

Figure 4.7: Normalized design variables of the RAE2822 baseline and the optimized airfoils for the best obtained results in Case 1 (inviscid) without and with wing box constraint (left and right graphs, respectively), considering the three search methods

constraint.

When the thickness of the airfoil is constrained at the wing box region, the search functions followed the approach as before for the upper surface, although to a

less extent, as depicted in Fig. 4.6(b). However, the curvature of the lower surface increased to cope with the two thickness constraints, resulting in slightly lower drag reductions. Regarding the design variables, as for the previous case they differ among the search functions even though similar airfoil shapes are obtained, which can be seen in Fig. 4.7(b).

4.5 Case 2 - Viscous CFD

Similarly to the inviscid optimization case, the objective for the viscous condition is a minimization of the drag, subjected to a minimum lift coefficient, which is now set to 0.7325. Two optimizations are considered, one with a lift coefficient constraint only and a second geometrically restrained to imply a wing box, where the thickness at 25% and 75% is to be kept at a minimum value. Equations 4.6 and 4.7 state the optimization problems without and with a wing box constraint, respectively.

$$\begin{aligned} &\text{minimize} && C_d(\boldsymbol{x}) \\ &\text{w.r.t.} && \boldsymbol{x} \\ &\text{subject to} && C_l(\boldsymbol{x}) \geq 0.7315 \ , \end{aligned} \tag{4.6}$$

$$\begin{aligned} &\text{minimize} && C_d(\boldsymbol{x}) \\ &\text{w.r.t.} && \boldsymbol{x} \\ &\text{subject to} && C_l(\boldsymbol{x}) \geq 0.7315 \\ & && t_{0.25c}(\boldsymbol{x}) \geq t_{0.25c_{\text{RAE2822}}} \\ & && t_{0.75c}(\boldsymbol{x}) \geq t_{0.75c_{\text{RAE2822}}} \ . \end{aligned} \tag{4.7}$$

Due to the high computational costs, only one run with an initial sample is performed and the number of iterations was limited to 50, as already sufficient results were obtained for case 1. Similar to case 1, the surrogate model of the drag and lift response is searched with a genetic algorithm to determine the next infill point. With a large size of population the optimizer is able to identify a new design with improved fitness with a high chance.

Fig. 4.8 displays the convergence for the case with the constraint for the minimum lift coefficient. In Fig. 4.9 the iteration progress of the optimization with the lift coefficient and the wing box constraint is shown. The upper row visualizes the drag coefficient value, while the lower row represents the lift coefficient with the minimum

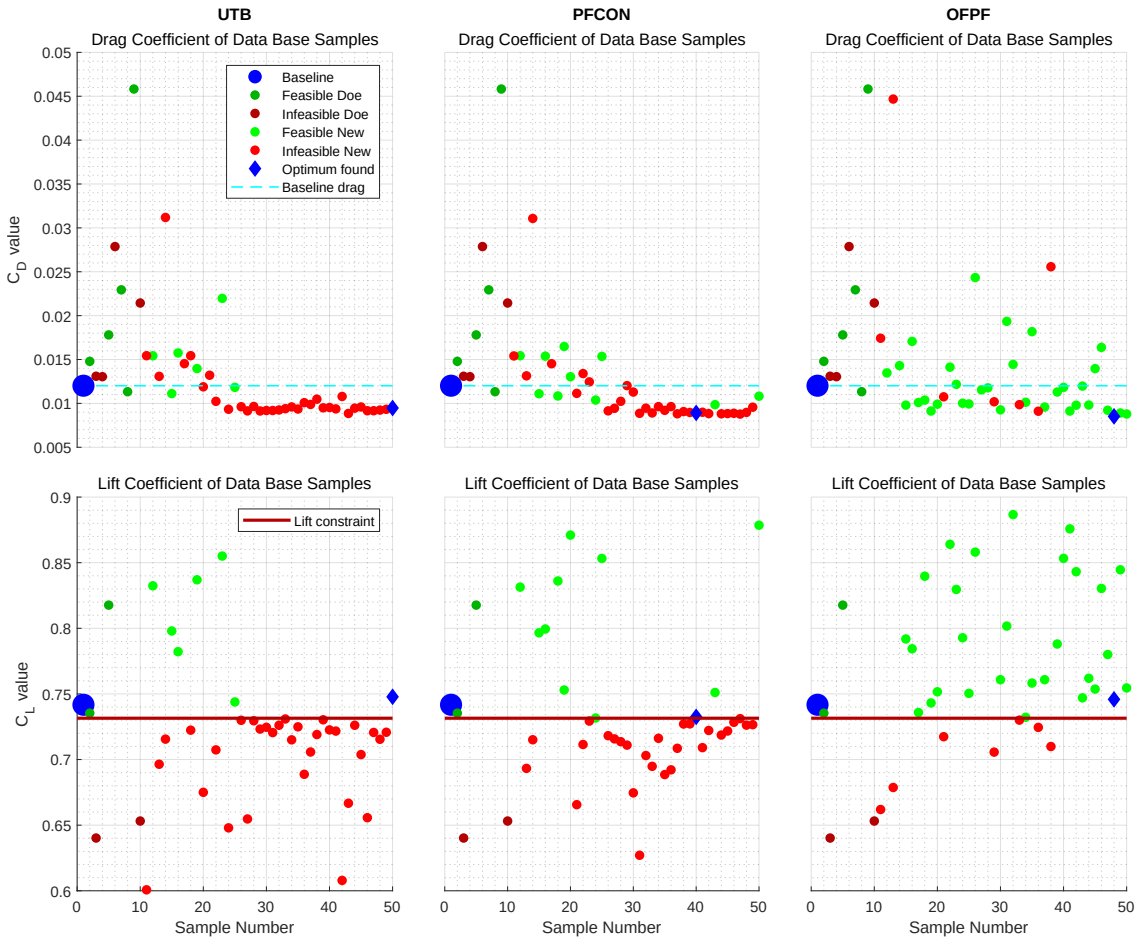

Figure 4.8: Convergence results of the viscous optimization (Case 2) with the minimum lift coefficient constrain for the three tested methods (UTB, PFCON and OFPF in the left, mid and right graphs, respectively)

required value, shown as dark red line. The blue dot represents the baseline configuration, the blue diamond the best obtained result within the given computational time. From left to right, the shown results are the UTB, PFCON and OFPF, respectively. As observed in the inviscid optimization case, the OFPF evolves from the feasible region, seen as green designs in the iterations, while the UTB and PFCON approach from the infeasible site, as more freedom is permitted due to the uncertainty consideration.

All three methods were able to reduce the drag significantly while fulfilling the constraints. The results are summarized in Table 4.7. For the case without the geometric constraint, the highest reduction was achieved by the OFPF (29%), followed by the PFCON (26%) and the UTB (21%). Considering the thickness constraint, all three results were very close, with the PFCON having a slightly better reduction

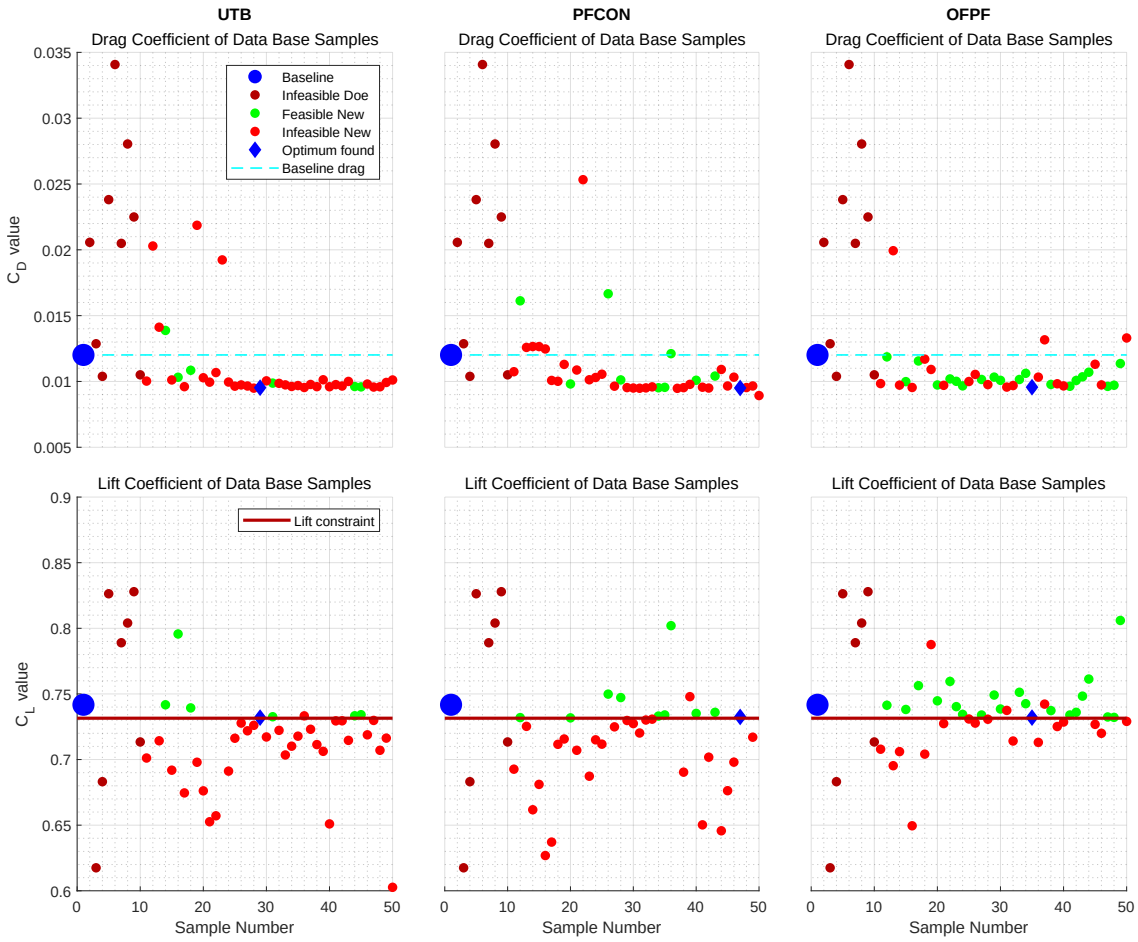

Figure 4.9: Convergence results of the viscous optimization (Case 2) with the lift coefficient and the additional wing box constrain for the three tested methods (UTB, PFCON and OFPF in the left, mid and right graphs, respectively)

	C_l Constraint			C_l + WB constraint		
	#	C_l [-]	C_d [drag counts]	#	C_l [-]	C_d [drag counts]
Baseline	-	0.7417	120.1	-	0.7417	120.1
UTB	50	0.7478	94.7	29	0.7320	95.3
PFCON	40	0.7325	89.1	47	0.7325	95.0
OFPF	48	0.7459	85.2	35	0.7319	95.6

Table 4.7: Results of Airfoil Optimization for Case 2 (viscous)

(20.9%), before the UTB (20.6%) and the OFPF (20.4%). However, convergence was not reached in any of the three methods, as the change in design, objective and constraint is still varying significantly.

In Fig. 4.10 the pressure distribution for the airfoils is presented for the two constraint cases. The baseline pressure coefficient is visualized bedsides the results of the three optimization methods. One can observe that the shock is weakened for

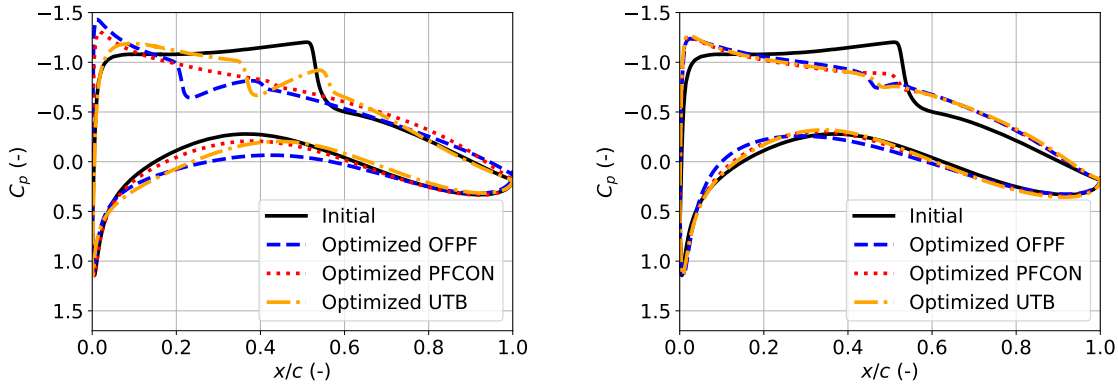

(a) C_p distributions for C_l constraint

(b) C_p distributions for C_l and geometric constraint

Figure 4.10: C_p distributions of the baseline and the best obtained results of the optimization for Case 2 (viscous) with lift coefficient constraint (left) and with lift coefficient and wing box constraint (right), considering the three search methods

both constraint cases, while the leading edge pressure coefficient is increased. The differences between the three optimization results for the lift coefficient constraint only, as shown in Fig. 4.10(a), are clearly visible, showing that a convergence towards one design is not yet present. Considering the lift coefficient and geometric constraint, the results are more alike, observable in Fig. 4.10(b), slightly increasing the leading edge pressure coefficient and weakening the shock to a small bump. Those differences can be noticed as well in the resulting airfoil shapes, presented in Fig. 4.11. While significant differences are present when only the lift constraint is considered, the airfoils are similar shaped if aerodynamic and geometric constraints are imposed. Regarding the trend of the shapes, if only the lift coefficient constraint is considered, the strategy of increasing the leading radius to accelerate the flow combined with a thickness reduction is followed by the three search functions in Case 2, alike to Case 1, visible in Fig. 4.11(a). However, a different extend of this shaping is recognizable, showing the aforementioned absence of convergence. When the wing box constraint is added the differences to the initial airfoil are reduced as observed in Fig. 4.11(b). The increase in leading edge radius, however, is again present. A flatter upper surface is compensated by a thicker leading edge region of the lower surface to comply with the

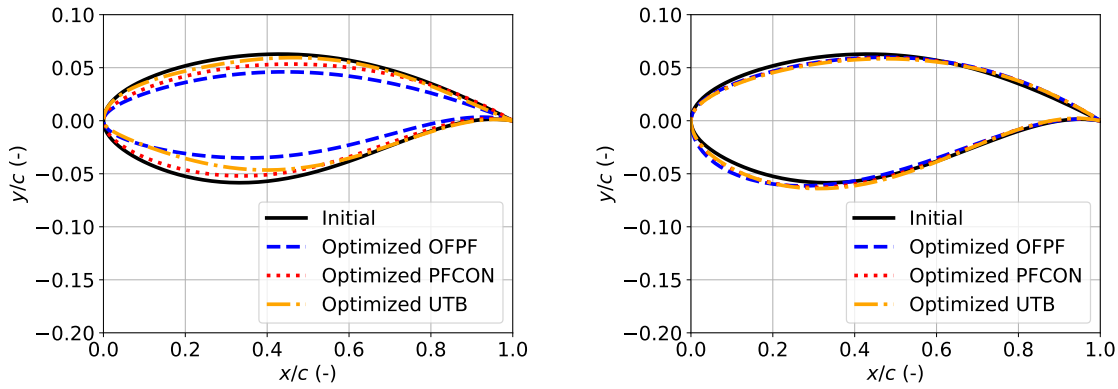

(a) Airfoil shapes for C_l constraint

(b) Airfoil shapes for C_l and geometric constraint

Figure 4.11: Airfoil shapes of the baseline and the best obtained results of the optimization for Case 2 (viscous) with lift coefficient constraint (left) and with lift coefficient and wing box constraint (right), considering the three search methods

thickness constraint. All three methods evolved the design towards a similar shape, implying the presence of a more distinct minimum.

Fig. 4.12 presents the distribution of the normalized design variables. As anticipated from the airfoil shapes, significant differences can still be found in the distribution of the design variables for the case where only the aerodynamic constraint is required. While , but also in Fig. 4.12(b). Nevertheless, the strength of the shock is still substantially reduced as noted from the decrease in C_d.

4.6 Remarks regarding the Probability of Feasibility Approach on the Airfoil Optimization

Opposing to the mathematical test functions discussed in section 3.6, the aerodynamic shape optimization problem shows less conclusive results. For the inviscid flow case (Case 1), the UTB delivers the best results on average for the geometric unconstrained optimization followed closely by the OFPF and the PFCON, with drag reductions of 78.8%, 78.5% and 76.4%, respectively. When the wing box constraint is introduced, the PFCON performs slightly better than the UTB and the OFPF, with improvements of 74.4%, 72.9% and 71.5% respectively.

For the viscous flow case (Case 2), the OFPF performed better than the PFCON and the UTB for the C_l constraint case, with approximately 29%, 26% and 21%

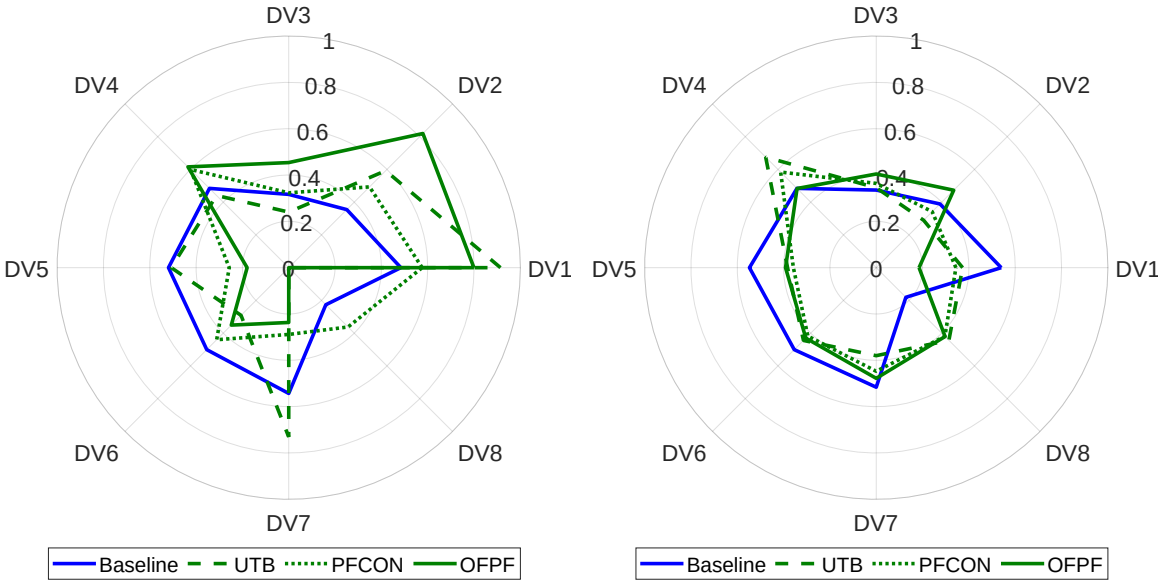

(a) Normalized design variables for C_l constraint

(b) Normalized design variables for C_l and geometric constraint

Figure 4.12: Normalized design variables of the baseline and the best obtained results of the optimization for Case 2 (viscous) with lift coefficient constraint (left) and with lift coefficient and wing box constraint (right), considering the three search methods

reduction in drag, respectively. When considering the wing box thickness constraint, all three methods result in less than 1% difference in the final result for the best case, where the PFCON performed marginally better and reached a drag reduction of almost 21%.

Furthermore, it was observed that the iterative process using OFPF was more focused on feasible designs as opposed to the PFCON and the UTB. For the latter methods, the constraints considering the uncertainty of the model were allowed to be exceeded, leading to more infeasible designs close to the boundary. However, none of the methods ultimately converged as the design response did not close on both constraint and objective. Moreover, the highly nonlinear behavior of the flow physics is expected to influence this outcome. Nevertheless, all methods were able to reduce the drag significantly compared to the initial design. The present work highlights the well known issue in surrogate based optimization, where the termination of the process is reached usually by limited computational resources available.

Chapter 5

Multi-disciplinary Design Optimization of Novel Aircraft Configurations

In this chapter the analysis tools are applied to preliminary aircraft design studies in a multi-disciplinary design optimization environment. The methodology is set up in the first part to contextualize the employed tools in the process, including the evaluation tools for the different disciplines and the surrogate based optimization procedure. Subsequently, the described methodology is utilized for two novel aircraft configuration optimizations.

Those optimizations were performed in cooperation with an industrial partner to investigate aeroelastic influence on novel aircraft configuration. More specifically, an aircraft with a high-aspect ratio wing was optimized from a baseline towards a higher aspect ratio. Likewise, based on the same baseline aircraft and with similar initial and boundary conditions, a strut-braced wing aircraft was investigated and optimized. It is assessed to which extend the optimization can rely on low- and high-fidelity models. Further, it is evaluated if the computational cost can be reduced by a reduction of the multiple constraints. In a priori assessments of sets of configurations, covering a wide range of designs, the active constraints are identified and addressed. The results are discussed and conclusions are drawn regarding computational costs and optimization results.

This chapter contains modified excerpts from the articles “On the Multi-fidelity Approach in Surrogate-based MDO of HARW aircraft” [230] and “Optimization and

comparison of strut-braced and high aspect ratio wing aircraft configurations including flutter analysis with geometric non-linearities" [231], the author was involved in with major contributions. The modifications serve to contextualize the aspects of the context and are elaborated in the scope of the thesis.

5.1 Multi-Disciplinary Design Optimization Methodology

The introduced tools are combined and integrated in a multi-disciplinary design optimization methodology. This includes the surrogate-based optimization strategy, the multi-disciplinary design analysis framework to assess the aeroelastic response of an aircraft configuration and the flutter estimation. Further, some additional aspects need to be incorporated to complete the process, which will be explained in the following section.

For one, to wrap the optimization in a structure, MATLAB is employed, serving as the interface for the data and information transfer between the models and tools. Furthermore, since the MDA does not model control surfaces, a trimmed flight condition has to be obtained by means of interpolated untrimmed conditions. Thus, a prior evaluation of the tail with several different areas is performed for a range of AoAs in advance using RANS. From the obtained results the drag, lift and moment coefficients can be calculated and used as tail model to trim the aircraft. The range of areas ensures that with a change in wing area a constant volume coefficient can be maintained, to maintain similar control/stability characteristics. These generated results can then be interpolated to obtain the lift, drag and pitching moment variation with AoA for the horizontal tail corresponding to wing area of the configuration being analysed. In the trim analysis the results from the horizontal tail model, a propulsion model and the obtained FSI solution can then be interpolated or extrapolated to obtain the trimmed AoA. Further, horizontal tail incidence angle and thrust/fuel flow for a specific flight condition (speed, altitude, aircraft mass, load factor) is obtained.

With all tools in place, the methodology can be established. A XDSM graph is shown in Fig 5.1. Assuming a novel aircraft configuration is to be analysed, the starting point is the definition of the design variables and the parametrization. With an initially generated DoE and the evaluation of each initial design, the surrogate models can be built and the MDO, based on those surrogates, can start. For any

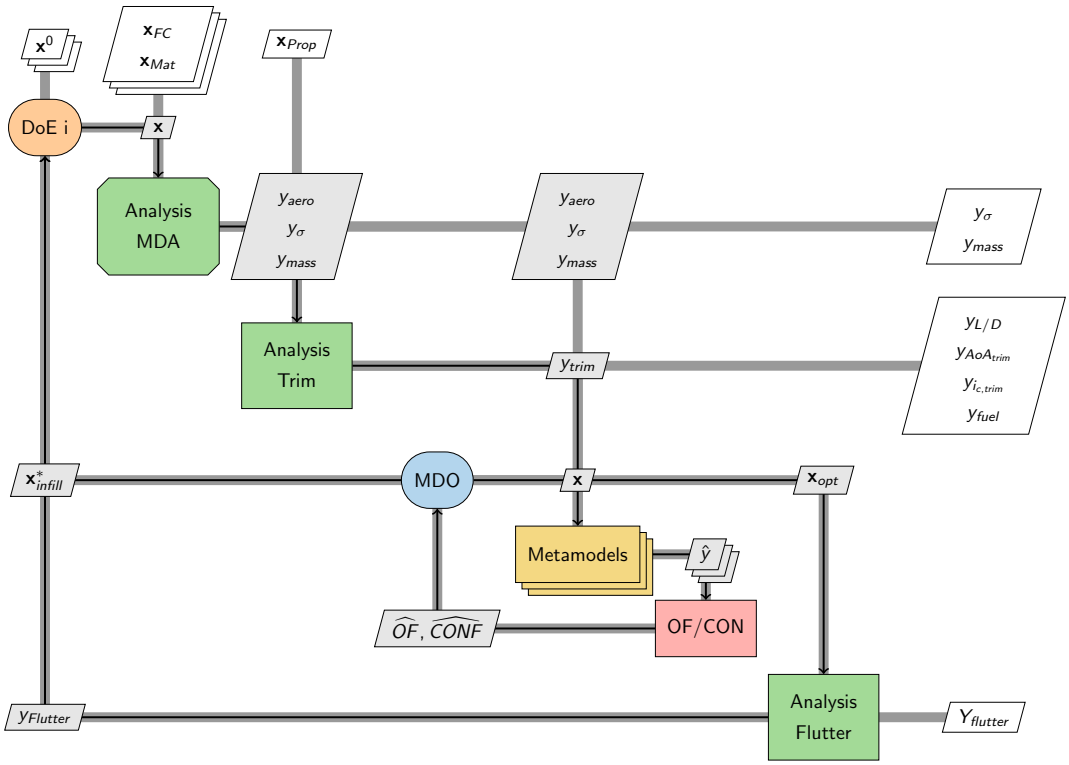

Figure 5.1: The XDSM for the integrated

infeasible point throughout the process, the data obtained is fed back into the data base and the surrogate models are rebuilt. Subsequently, the process is continued by searching and evaluating a new infill point. In the case of a design that could not be evaluated due to physical or computational issues, the predicted mean value of the surrogate is used as response. This way, the optimizer is encouraged to find more promising areas. Possible mentioned issues could arise from: (1) designs with highly unfeasible structure, where physically non-realistic deformations occur; (2) designs that happen to have meshing issues due to geometric shapes, where no reasonable mesh can be generated in the automatic process.

The evaluation of the single disciplines requires different duration, one objective of the methodology is therefore the reduction of computational cost. This intention can be tackled at different stages in the process. The use of high- and low-fidelity evaluation tools enables the possibility to investigate the extend, to which computationally costly high-fidelity models can be replaced by low-fidelity evaluations. This aspect is discussed in the application later on in chapter 5.2. Also, to reduce the number of

costly physics based evaluations, one can assess which assessments are necessary to drive a successful optimization. Considering all imaginable constraints and objectives is a precise, but costly way. Therefore, if specific evaluations can be eliminated from an optimization, additional cost reduction can be obtained. This aspect is as well further investigated in chapter 5.2. Furthermore, an efficient search strategy for the surrogate modelling process is another engagement point, where a cost reduction can be achieved. The proposed method using the uncertainty in the surrogate model is applied to an engineering problem in chapter 4 and conclusions regarding cost effectiveness and results are drawn.

5.2 Multi-disciplinary Design Optimization of a High Aspect Ratio Wing Aircraft

The introduced methodology was applied within a project together with an industrial partner. The goal of the project was the assessment of novel aircraft configurations and the influence of aeroelasticity in the preliminary aircraft design process. With the limited computational resources available, the decision was made to use a SBO approach. Furthermore, an interest was expressed about the use of different levels of fidelity in the early design stages of the development process.

Nowadays conceptual aircraft design requires assessment tools other than empirical formulas or statistical data to determine the best conceptual candidates to proceed with a detailed design. This requirement is prompted by the emergence of new aircraft configurations that rely on design space expansion to comply with environmental impact and cost reduction requirements. The MDO procedure should be as fast as possible; therefore, utilizing lower fidelity and computationally cheaper models extensively is favored considered the final result is not jeopardized.

5.2.1 Problem Description

A baseline aircraft configuration has been provided by Bombardier Aerospace (BA) in order to develop the study of the HARW configuration. It represents a generic medium range transport aircraft with a low wing with aspect ratio of 12, a typical fuselage and a T-tail. Structural, fuel and system masses distribution were also provided, and a predefined jet engine database is used to determine the fuel consumption given a thrust requirement and a flight condition. Figure 5.2 shows the mission profile. The

cruise Mach number and altitude are 0.7 and 11Km (36000ft) respectively; the dive Mach number is 0.82.

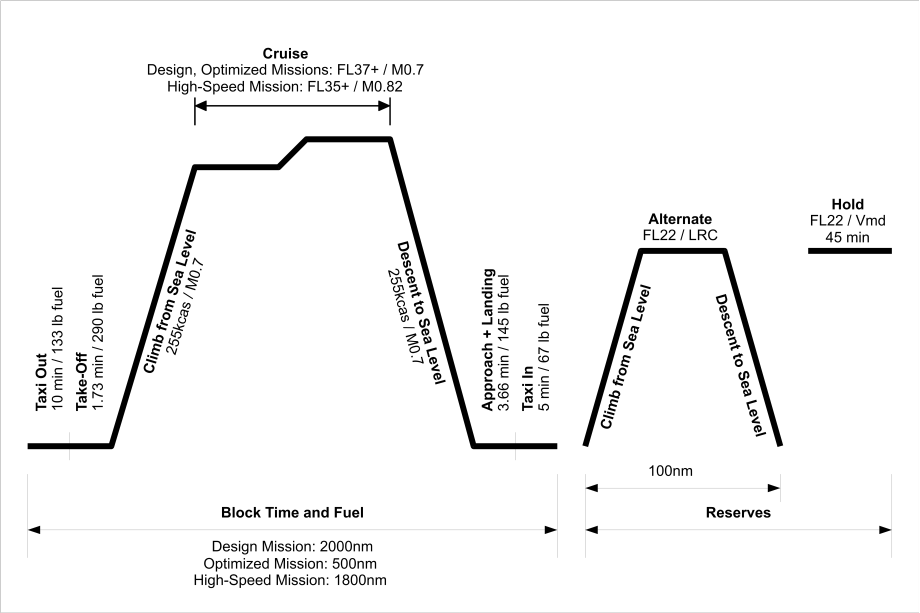

Figure 5.2: Mission Profile Definition

The objective of this application is to optimize the aircraft configuration considering environmental and operational costs metric (fuel consumption in cruise) and also a production cost metric (wing structural mass). The constraints for the optimization include maximum allowable wing structural stress (σ) in 3 different load cases and a minimum flutter margin constraint. The flutter margin is defined by the flutter speed estimated at a 2.5g loading condition at dive speed. The MDO procedure introduced earlier is employed for this purpose.

Throughout this study, the wing's airfoils shape and span-wise relative position are assumed constant along with wing sweep. Hence, the optimization result is limited in its potential, as overall changes in geometry would require a further aerodynamic optimization. However, the computational costs would be significantly higher as the number of design variables would increase considerably. Furthermore, the benefit throughout the optimization and the methodology of the multi-fidelity assessment can be shown with the given restraints in the detail of the optimization. Fuselage, vertical tail geometry and horizontal tail planform are also assumed to be constant, as well as their structural components and mass distribution. The wing structure is assumed to

be a wingbox type structure made of isotropic aluminum to match a typically used aircraft material. The properties are summarized in table 5.1.

Material property	Unit	Value
Young modulus	$[GPa]$	70
Rigidity modulus	$[GPa]$	27
Poisson ratio	[-]	0.33
Yield strength	$[MPa]$	400
Material density	$[kg/m^3]$	2700

Table 5.1: Material properties of the employed aluminum alloy for the aircraft structure

Variations allowed from the baseline wing configuration include parameters that directly affect both aerodynamic and structural characteristics (span, chord and twist distributions) and parameters that affect primarily the structural characteristics and indirectly the aerodynamic characteristics due to effects on deformation and mass (spar and skin thickness distributions). As a consequence of the wing geometric changes, the horizontal tail area is changed in order to maintain the same volume coefficient as the baseline configuration.

The problem statement is as follows:

$$\begin{aligned} &\text{minimize} && f(\boldsymbol{x}) = Aw(\boldsymbol{x}) + Bc(\boldsymbol{x}) \\ &\text{w.r.t.} && \boldsymbol{x} \\ &\text{subject to} && \sigma_i(\boldsymbol{x}) \leq \frac{\sigma_{yield}}{SF}; \quad i = 1..3 \\ & && \frac{FM \times DS - FS(\boldsymbol{x})}{DS} \leq 0, \end{aligned} \tag{5.1}$$

where w and c are the objective function values of structural mass and fuel consumption based on cruise flight thrust requirement, respectively. A and B are weighting constants for the multi-objective optimization and were set by external reference according to typical industrial weighting of $A/B = 1/3$, based on correspondence with the industrial partner and their earlier work, to be found in the literature as well [262; 227]. The load case index is described by i, the maximum allowed stress is yield stress of aluminum, σ_{yield}, paired with a safety factor (SF) of 1.5. The flutter margin, is given as the difference of the estimated flutter speed and the dive speed, shown in the equation as FM, FS and DS, respectively.

The 14 design variables are listed in Table 5.2 and contain geometric, aerodynamic

and structural influence variables. Fig. 5.3 presents the design variables graphically for a better understanding of the geometric relations. The skin and spar thicknesses as

Design variable	Description
x_1	Span factor (relative to baseline)
x_2	Chord factor (relative to baseline)
x_3 & x_7	Skin & spar kink position (relative to wingspan)
x_4 & x_8	Skin & spar root thickness
x_5 & x_9	Skin & spar kink thickness
x_6 & x_{10}	Skin & spar tip thickness
x_{11}	Twist kink position (relative to wingspan)
x_{12}	Twist at wing root (incidence)
x_{13}	Twist at wing kink
x_{14}	Twist at wing tip

Table 5.2: Design variables for the wing parametrization and optimization

well as the twist spanwise distributions are bilinear, *i.e.* are described by continuous functions composed of two linear segments with different slopes. The span-wise

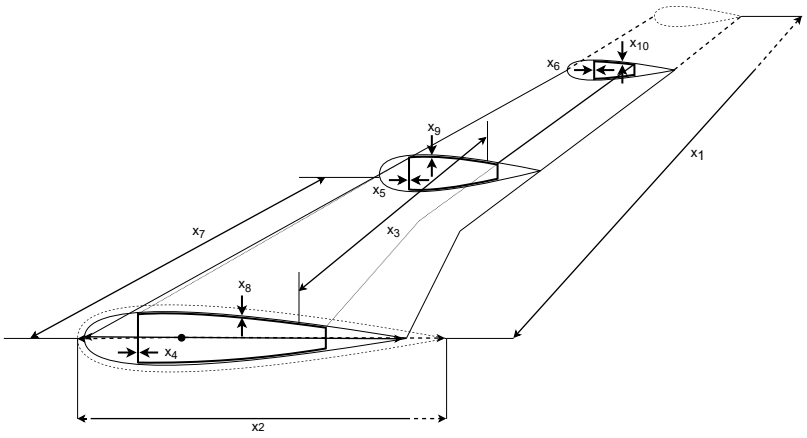

Figure 5.3: Representation of exemplary design variables

position where the slope changes is hereafter referred to as kink position. A decoupling of structural and aerodynamic kink position allowed more freedom for the optimization, while the number of design variables could still be relatively low, considering the related high computational expenses for single function evaluations.

Furthermore, choices are made about which evaluations require high- and low-fidelity results for sufficient accuracy, leading to a mixed-fidelity approach. This study

presents a quantification of the differences between FSI results using low and high-fidelity aerodynamics models as a precursor to building a surrogate model and running a surrogate based multi-disciplinary design optimization of a HARW. It intends to provide practical information on the advantages and accuracy of multi-fidelity analyses approaches in aero-structural optimization as well as on the design driving constraints, including flutter margin. The utilization of the levels of fidelity refer herein on the assessment tools. The use of multi-fidelity responses to built surrogate models is not intended, since the differences of the low- and high-fidelity responses at the critical assessments might jeopardize the results due to their non-linear nature. This investigation also reports the findings on the performance improvements of a surrogate based optimized HARW configuration when compared to a baseline configuration for a medium range transport aircraft. As stated before, the expectation is that increasing AR translates into higher deformations with effects on fuel consumption and flutter speed.

To analyse and improve the aircraft configuration the multi-disciplinary design optimization methodology introduced previously is employed. It utilizes the multi-disciplinary design optimization framework that includes the multi-disciplinary design analysis tool, with low- and high-fidelity capabilities, for the FSI analysis, NASTRAN with its low fidelity models as flutter estimation tool, and integrates it into the surrogate based optimization. Rehearsing the key features, the FSI calculation couples an Equivalent Beam Model (EBM) to a Panel Method (PM) as a low-fidelity assessment to obtain the deformed shape due to wing loading. The same EBM coupled with a RANS aerodynamic solver is used as the high-fidelity FSI model. The Shear Stress Transport $k-\omega$ model is used for the turbulence modelling and an asymptotic ΔC_L and ΔC_D criterion is used for convergence. The wall clock time for the high-fidelity analysis of the 1g load case was 5 hours and for the 2.5g load case 7 hours, where roughly 30% of the time was necessary for the meshing procedure for the deformed aircraft. The computation was executed on a server with 60 cores[1].

With the obtained data, estimations can be performed regarding the wingbox mass, the distribution of the maximum Von-Mises stress and the aerodynamic coefficients of the flexible aircraft. An initial mesh convergence study was performed on the baseline model to establish the refinements and mesh sizing for the high-fidelity CFD, exemplary values are listed in Table 5.3. The final models contain between 6 million to 9 million cells. To obtain the trimmed state of the aircraft, a number of AoAs

[1]Intel i7 4870 @2.4GHz

Mesh refinement	Number of cells	C_L	C_D
Coarse	4 mil	0.325	0.0230
Medium	7 mil	0.349	0.0182
Fine	14 mil	0.351	0.0181

Table 5.3: Mesh properties

to interpolate or extrapolate the the aerodynamic coefficients was performed. The required incidence of the horizontal tail is calculated a posteriori together with the thrust and aircraft AoA after all the aerodynamic load components (lift, drag and pitching moment) are calculated.

All configurations preserved a constant volume coefficient to maintain similar control/stability characteristics. As a consequence, the effect of the horizontal tail incidence on the wing loads and deformation are neglected in these analyses. This seems reasonable, given that the tail is located aft of the wing and that the tail loading acts in the fuselage.

The propulsion model provided by BA comprises a database with entries for thrust, fuel flow, altitude and Mach number which are interpolated to obtain an approximation of the fuel consumption for a given thrust requirement and flight condition. This model was not incorporated into the FSI procedure in the current study, meaning that the thrust force is not included in the structural deformation calculations. Similar to the horizontal tail trimming effect, the thrust effect is deemed to be of negligible consequence in the wing's deformed shape since the engines are located in the aft part of the aircraft and loading the fuselage, and the aircraft is assumed trimmed at a fixed fuselage pitch angle.

The flutter speed is estimated for the deformed wing shape under the steady flight condition loading. After extracting the shape information from the MDA framework and generating the NASTRAN input, the $p-k$ method is used to solve for the flutter speeds and respective frequency. As a remark it should be noted, that no transonic corrections are considered. Further, no nominal steady-state stress or stress stiffening effects are induced in the beam structure, only the effects of the geometry are being accounted for. As NASTRAN's implemented PKNL approach is used, triplets for realistic flight conditions of Mach number, density and speed are given to the solver.

Figure 5.4 depicts the used models.

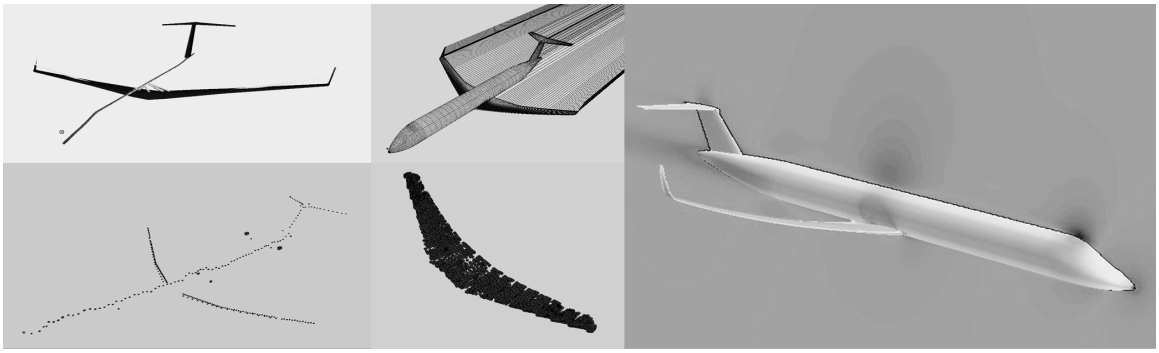

Figure 5.4: Model representations: EBM (up left); PM (up middle); RANS CFD (right); Payload and Systems mass distribution (down left) and Fuel mass (down middle).

5.2.2 Assessment and Analysis of Fidelity and Constraints

One aspect of the work was the assessment of the utilization of low- and high-fidelity tools in the preliminary design stage. The question was raised to which extend one could rely on low-fidelity models to predict values of interest with sufficient accuracy to allow an evaluation of the design.

Given the workflow described previously, the number of the more expensive FSI runs required per configuration should be minimized. The evaluation of the objective function and each constraint in the optimization statement requires the FSI calculation at 2 different AoA for posterior trimming and flutter margin calculations.

It is generally accepted that optimization based on high-fidelity CFD results is prohibitively costly in terms of computational resources and/or time. The FSI procedure alone using high-fidelity CFD is over 10 fold more time consuming than the low-fidelity alternative, as it currently also requires remeshing. This factor could potentially be reduced if a mesh deformation algorithm could be implemented but would still be about 5. In a preliminary design stage a lower level of fidelity is deemed sufficient to obtain comprehensive overall results. Therefore, taking into consideration this specific aircraft optimization problem, strategies to minimize the number of FSI runs and also the high-fidelity CFD runs based on design knowledge are, in order:

1. Reduce the number of constraints assuming that it is known a priori which ones are active during the optimization procedure. This would reduce significantly the number of evaluations required and the satisfaction of the remaining initial constraint can be verified after the optimized result is obtained.

2. Substitute FSI results based on high-fidelity CFD by results based on low-fidelity CFD if and whenever the accuracy of results allows it. This could be the case if lift predictions by the low-fidelity CFD models are accurate enough and allow for satisfactory evaluations of the stress constraints.

3. Perform FSI based on low-fidelity CFD and use the converged result to calculate the high-fidelity CFD results for the final deformed shape obtained. If the final shape is not significantly changed by the loading calculated with high-fidelity CFD the result might still be below the convergence criteria. This is more likely to occur for low deformation flight conditions as in cruise and would allow assessment of the drag accurately, resorting to only one high-fidelity CFD run. If the accuracy allows, the same strategy can be used to evaluate and obtain the transonic correction for the flutter speed calculation at the 2.5g dive speed flight condition.

The aforementioned possibilities to reduce the computational time aim to either reduce unnecessary constraints or reduce the number of high-fidelity CFD analyses.

Active Stress Constraint Assessment

In order to understand the validity of the strategies described above to limit the high-fidelity CFD runs in the MDA procedure, an initial set of configurations was analyzed. The set consists of 5 configurations with increasing AR that include the baseline configuration. All configurations have the same wing area while the span is varied between 95% and 115% and the chord distribution is scaled accordingly. The AR of the configurations therefore varies between 90% and 132% of the baseline configuration. The relative spanwise twist distribution is maintained for all configurations in this set.

While the geometric variables become defined by the statements above, the structural variables still require definition. A separate structural optimization procedure was implemented in order to minimize the structural weight for each configuration. A feasible sequential quadratic programming optimizer was employed to obtain the values for the structural design variables. This procedure uses the same structural stress constraints as the MDO procedure, but no FSI is performed; therefore, the loading for each constraint is constant.

Figure 5.5 depicts the Von-Mises stress distribution on the wing structural models for each structurally optimized configuration and for each constraint. The maximum

stress is located around 40% of the wing, at the aerodynamic kink (Yehudi break). It is clear from Figure 5.5 that the active constraint corresponds to the full fuel @ cruise speed 2.5g pull-up load case for all configurations. Both the full fuel @ cruise speed -1g load case and the half fuel @ cruise speed 2.5g pull up still have significant margin before becoming active constraints. Based on these results, the subsequent MDO procedure dropped the above-mentioned inactive constraints.

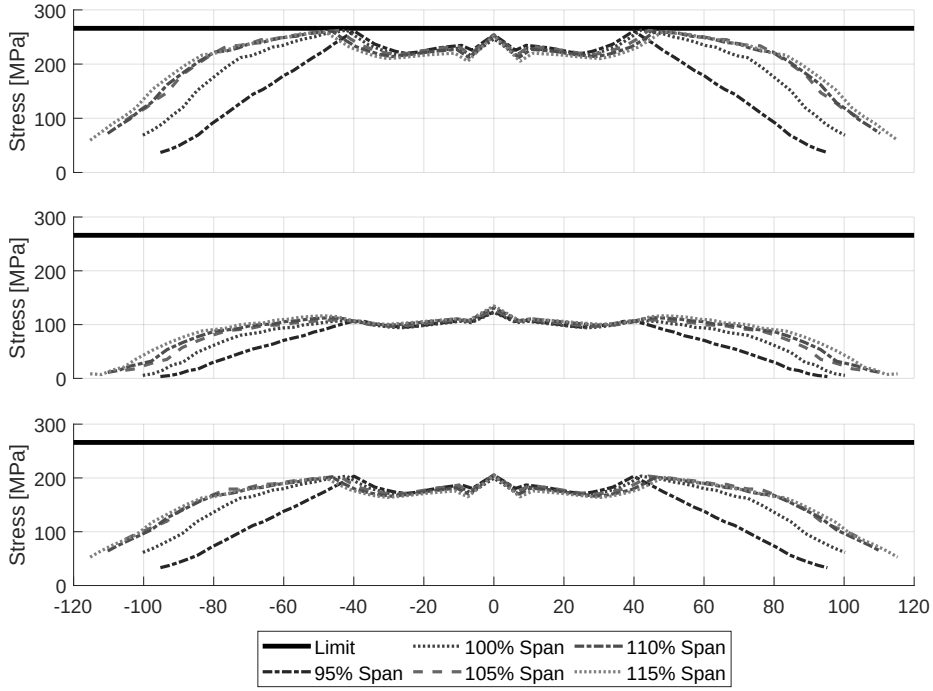

Figure 5.5: Von Mises stress distribution along the wingspan of the analyzed set of configurations for each structural optimization constraint (top to bottom: Load case 1, load case 2 and load case 3).

Assessment of low- and high-fidelity Loading and Deformation

Once the structural variables were determined, the next step was the investigation of the low- and high-fidelity FSI procedure. A FSI run using low-fidelity CFD alone and a low-fidelity FSI run followed by one FSI iteration using high-fidelity CFD were performed for the cruise flight condition and the active constraint flight condition (2.5g pull up @ full fuel). This is intended to quantify the differences between the loading and deformation predicted with low-fidelity CFD as compared to the high-fidelity CFD results, and determine in which cases the high-fidelity CFD requires further FSI

iterations.

At the same AoA, the wing tip vertical displacement and the wing twist displacement show extrapolated relative differences between the low-fidelity and high-fidelity assessments up to 9% with respect to the undeformed wing for the cruise flight condition. These percentage differences were actually the maximum percentage differences found during the optimization procedure, among the 110 configurations analyzed. The vast majority of the configurations showed differences below 3%, with the average difference for the tip displacement 2.8% and for the twist displacement 1.8%.

These modest changes in deflection are despite the differences in total lift for the cruise condition being higher in magnitude (up to 14.8% with an average of 5.5%). In this flight condition, the low-fidelity FSI result over predicts lift for the same AoA relative to the first iteration using high-fidelity CFD, which means that the difference in the load and its distribution is not enough to cause more significant differences in the wing's deformed shape. Therefore, it is expected that an FSI scheme such as the one described above, where the low-fidelity FSI is followed by only one high-fidelity FSI iteration, would suffice to obtain accurate drag predictions since the shape of the deformed wing is nearly maintained when changing from low-fidelity to high-fidelity FSI. Table 5.4 shows the results for the differences in vertical and twist displacements and C_L for the analyzed AoAs and for the calculated trim AoA. The shown values

	AR 10.9			AR 13.2			AR 15.7		
	1	2	Tr_{CFD}	1	2	Tr_{CFD}	1	2	Tr_{CFD}
AoA (°)	2.50	2.70	2.83	2.50	2.70	2.78	2.20	2.50	2.97
Δu (%)	-1.95	-2.35	-2.61	1.95	-0.57	-1.48	2.64	-2.47	-8.66
$\Delta twist$ (%)	-1.44	-1.77	-1.97	6.09	3.00	1.87	7.74	0.06	-8.96
ΔC_L (%)	7.70	6.81	6.25	7.08	4.87	4.06	5.88	4.63	2.92

Table 5.4: Cruise flight tip differences for vertical and twist displacements at the analyzed AoAs and at the high-fidelity CFD based extrapolated trim AoA for each configuration

describe the differences between the results of the low-fidelity and high-fidelity FSI runs. The indices 1 and 2 refer to the two calculated angles of attack, while the index Tr is for the extrapolated trimmed case for the cruise flight condition. Differences below 10% for the low-fidelity FSI are deemed acceptable for the preliminary aircraft design study.

For the active constraint case the situation is reversed, with the low-fidelity FSI

underestimating the load for the same AoA, which results in a predicted higher AoA to obtain the same 2.5g lift load. Reasons for this difference can be the more intense transonic non-linearities, for instance shocks and flow separation onset. Consequently, a higher AoA is interpolated to retrieve the same load. Table 5.5 shows the calculated AoAs and the differences in vertical and twist displacement at the same load based on the low-fidelity FSI results and on the first high-fidelity FSI iteration for the 2.5g lift load.

	AR 10.9	AR 13.2	AR 15.7
$AoA_{HF,CFD}$ (°)	3.04	3.08	2.94
AoA_{PM} (°)	3.63	3.72	3.77
Δu (%)	-6.57	-6.73	-5.70
$\Delta twist$ (%)	-6.68	-6.71	-4.28

Table 5.5: Active constraint tip differences for vertical and twist displacements between at the analyzed AoAs and at the high-fidelity CFD based interpolated trim AoA for each configuration

Figures 5.6 and 5.7 depict the vertical and twist angle displacement span wise distributions results for configurations *AR10.9*, *AR13.2* and *AR15.7* for both the cruise and active constraint trimmed flight conditions. These results show that the differences between the low-fidelity and the high-fidelity CFD FSI procedures described tend to increase as the AR increases and as the load magnitude increases.

Stress Assessment: Low-fidelity FSI plus one high-fidelity FSI Iteration vs Full high-fidelity FSI

As a result of this higher magnitude difference in the high load case, the stress distribution shows differences which are significant in the context of a MDO procedure and feasibility of a design cannot be assessed based on low-fidelity FSI alone, since it is not a conservative estimate (Figure 5.8). Given the higher magnitude of the negative twist for the first high-fidelity FSI iteration, it is expected that some load alleviation would cause a redistribution of lift and a relief of the bending moment in the wing for the same 2.5g load, resulting in a stress distribution closer to the low-fidelity FSI result. The one high-fidelity FSI iteration procedure would then be a conservative way to avoid the unacceptable computational cost of a full high-fidelity FSI run to assess the stress constraint. A more dominant difference in the stress results can be seen in the distribution when comparing the results with and without one high-fidelity

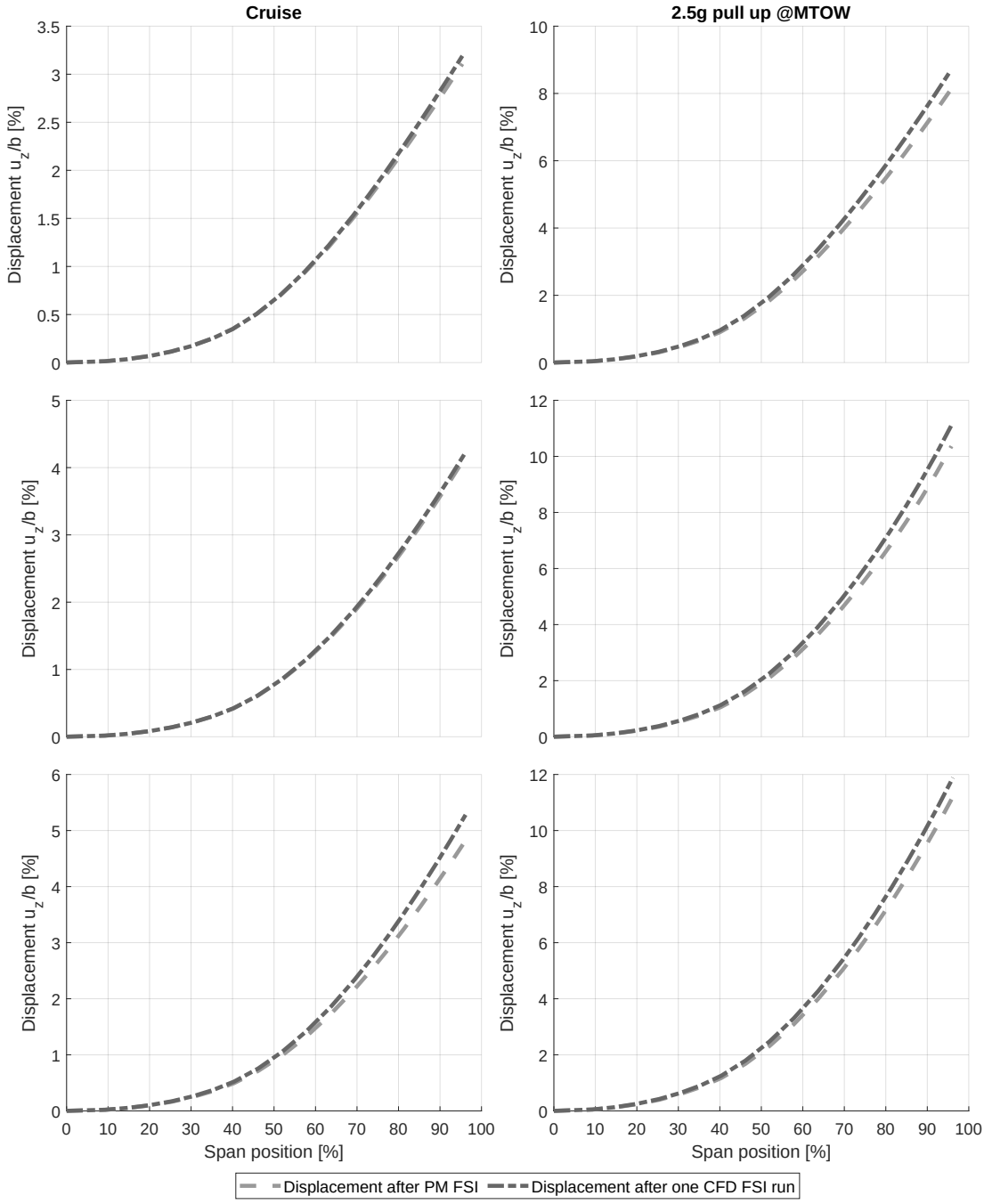

Figure 5.6: Vertical displacement vs spanwise station for Configurations with AR10.9 (Top), AR13.2 (Middle) and AR15.7 (Bottom) for a cruise flight condition (left) and a 2.5g pull up @ MTOW flight condition (right).

FSI iteration. Due to the altering geometric shape and the emerging change in lift distribution, especially for higher AR, the stress distribution distinguish significantly

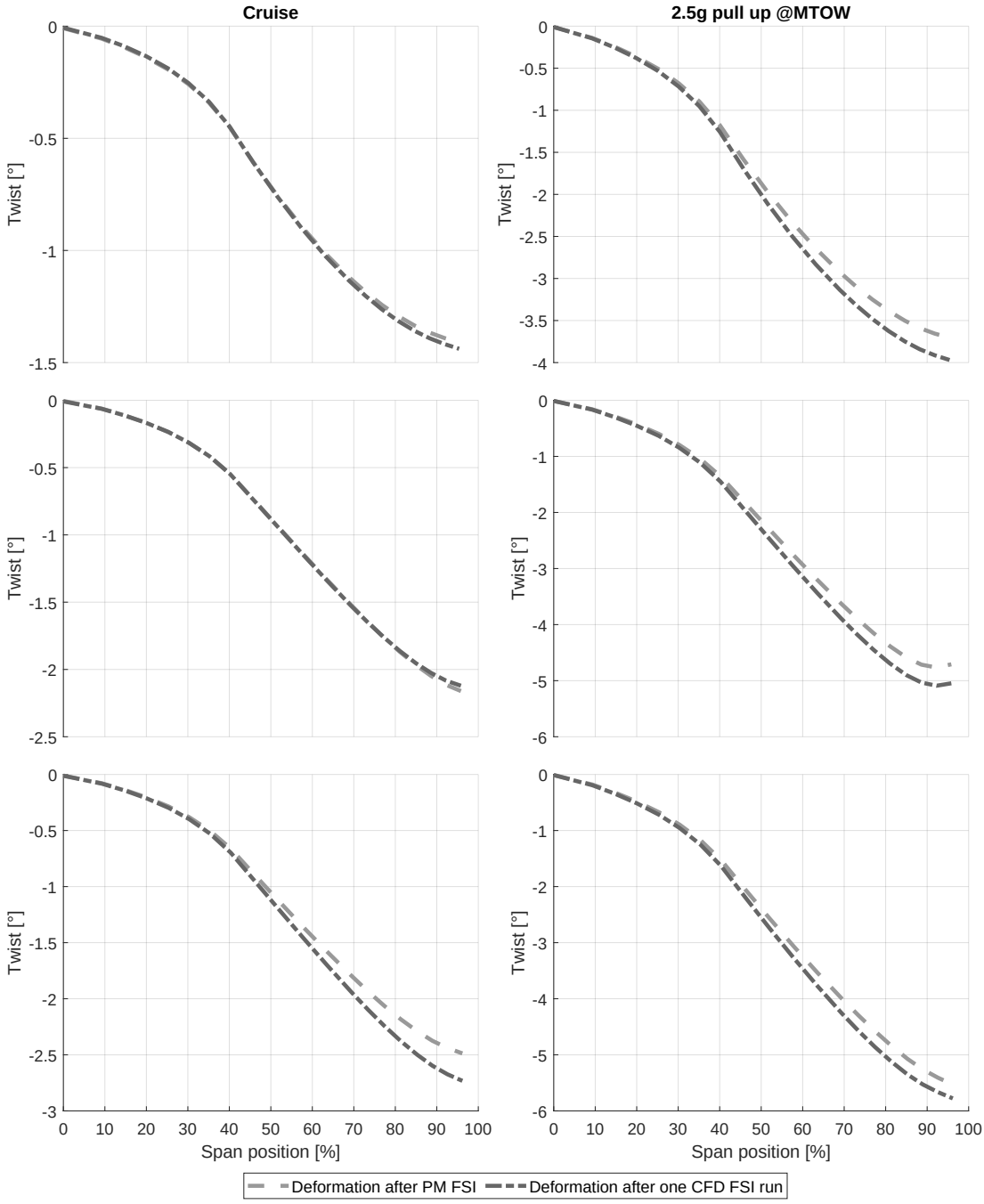

Figure 5.7: Twist displacement vs spanwise station for AR 11 (Top), AR 13.2 (Middle) and AR 15.7 (Bottom) for a cruise flight condition (left) and a 2.5g pull up @ MTOW flight condition (right).

from the rigid results (as shown in Figure 5.5).

A full high-fidelity CFD based FSI run was performed for the best configuration

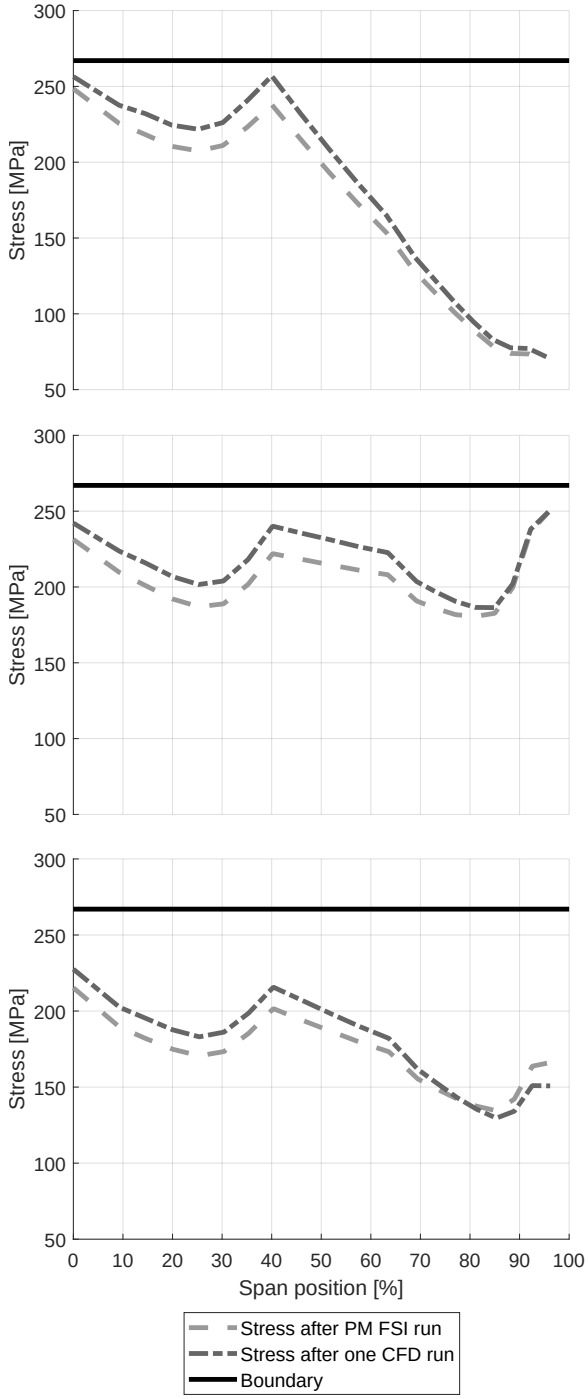

Figure 5.8: Von-Mises equivalent stress spanwise distribution for AR 11 (Top), AR 13.2 (Middle) and AR 15.7 (Bottom) for the 2.5g pull up @ MTOW flight condition.

obtained during the optimization procedure. This enabled validation of the assump-

tions of reduced influence of load differences between the low-fidelity FSI followed by one high-fidelity FSI iteration and the converged results of a complete high-fidelity FSI run in the lift and drag results. It also allowed the verification that the procedure of performing one high-fidelity FSI run after a converged low-fidelity FSI produces conservative stress estimates when compared to a converged full high-fidelity FSI run. Figure 5.9 depicts the results. One can observe that both assumptions seem to be valid for the configuration analyzed, with the converged high-fidelity FSI results being closer to the low-fidelity FSI results for dynamic pressures approximating the cruise and the active constraint cases, therefore reducing the shape differences as assumed for the cruise case and showing the stress results as being conservative in the active constraint case.

Table 5.6 shows the differences in lift and drag of the optimized configuration for the same AoA and the dynamic pressure approximating the cruise case. The results

$C_{L,C}$	$C_{L,up}$	$\Delta C_L(\%)$	$C_{D,C}$	$C_{D,up}$	$\Delta C_D(\%)$	L/D_C	L/D_{up}	$\Delta L/D(\%)$
0.658	0.662	-0.50	0.0314	0.0317	-1.00	20.958	20.852	0.51

Table 5.6: Comparison of lift and drag results between the used procedure (UP) and the converged (C) high-fidelity FSI for optimized configuration for a constant $AoA = 3°$

show that the magnitude of the error of the used procedure relative to the converged high-fidelity FSI is around 1% in drag and around 0.5% in both lift and L/D for this configuration. Under the assumption that these results can be generalized for the current problem, any configuration with improvements in L/D above 1% of the baseline model is deemed as having a better performance than the baseline.

Flutter Margin Assessment of various Aspect Ratio Configurations

Flutter boundary assessment for flutter margin calculations was performed to understand if this would be an active constraint. Fig. 5.10 shows the flutter boundary results for the configurations with *AR10.9*, *AR13.2*, *AR15.7* and the optimized configuration in undeformed and deformed states, together with the flight envelope and the flutter margin boundary requirement.

It is apparent that the flutter boundary is altered, with deformation reducing the flutter margin for all configurations shown. Nevertheless, the flutter speeds calculated greatly exceed the required flutter margin. Therefore, the flutter margin does not

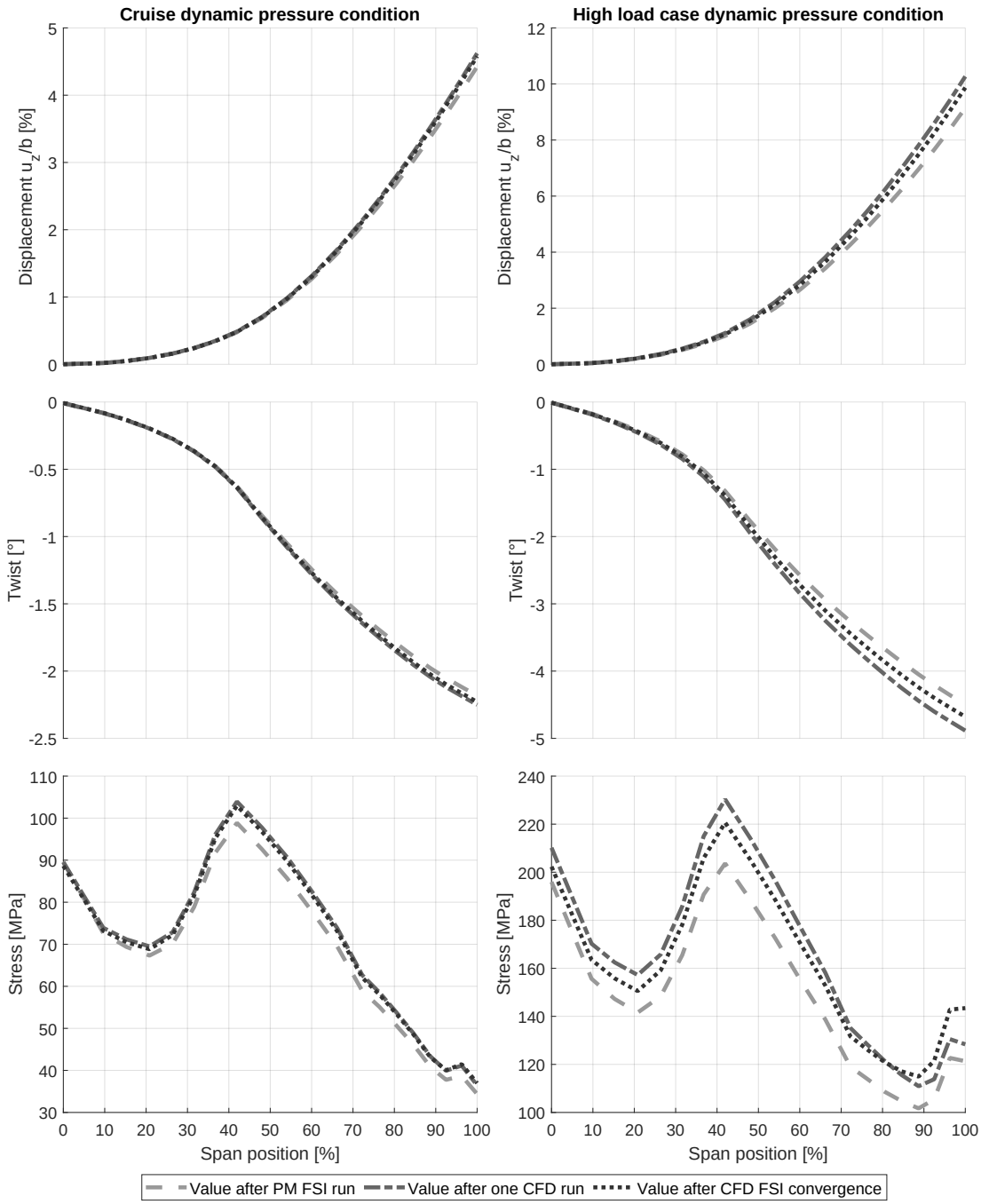

Figure 5.9: High-fidelity CFD based FSI results for the optimized configuration (AR 14) compared to low-fidelity FSI and to one high-fidelity FSI run after low-fidelity FSI convergence for a constant $AoA = 3°$ and different dynamic pressures.

seem to be an active constraint in the optimization, and it is confirmed that the best configuration respects the minimum flutter margin constraint.

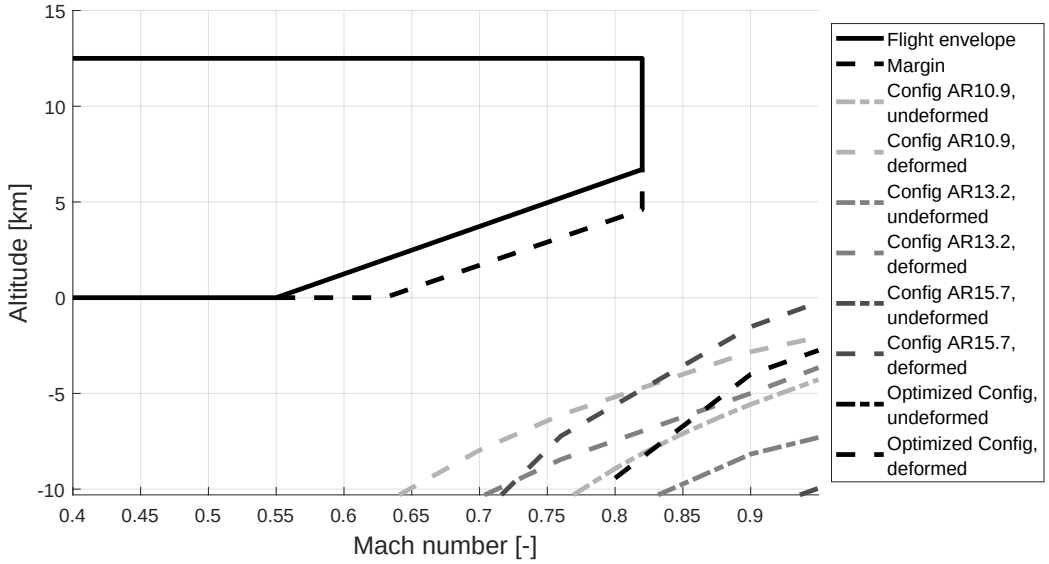

Figure 5.10: Flight envelope and required flutter margin and flutter boundaries for configurations *AR10.9*, *AR13.2*, *AR15.7* and the optimized one in undeformed and deformed states.

5.2.3 Multi-disciplinary Design Optimization Results

The MDO process followed the scheme introduced in Figure 1.11. The initial sample is generated by Latin Hypercube Sampling (LHS) [175] to ensure an adequate design space sampling. When the simulator cannot evaluate a specific sample, which can happen for some design variable combination, meshing errors or likewise, the sample was taken out and replaced by a different sample in a similar region (short Euclidian distance of not more than 5% of the normalized design space).

The surrogate models were built for the objective (weighted function of wing structural mass and fuel consumption) and constraint function (stress distribution along the wing structure). A Kriging regression model is used as described in the methodology chapter (section 3.5), with a regression hyperparameter value with limits of $1e-6$ and $1e-3$. This is necessary as inaccuracies due to meshing error, numerical rounding effects and likewise could otherwise result in a poorly built model if close points deviate too much.

The optimization with iterative sample addition was started and run until a maximum number of iterations was reached. In this work an Expected Improvement (EI) based infill criterion is used, using the uncertainty quantification provided by the Kriging model Jones and Schonlau [183]. The reason why the proposed approach with

the probability of feasibility (section 3.4) is not employed, has two distinct reasons. First, the proposed methodology using the probability of feasibility could not show a distinct advantage over a commonly used EGO approach. Second, at the time of the start of the optimization, the methodology was not yet developed to its current state and restrictions in project time required an alternative approach.

In each iteration the new sample is evaluated for the objective and constraint function and added to the initial database. This improves the model locally and, as each sample has a correlated influence on the other samples, the global prediction as well. In this procedure the prediction of surrogate model becomes less erroneous and the predictions of the surrogate model therefore closer to the real response. The new sample, determined by the infill criterion, was then evaluated. If a convergence criterion or the maximum number of iterations is reached, the process is terminated.

In the present optimization the process was terminated after 110 iterations reaching the maximum available number of iterations and no remarkable improvement could be achieved in the later iterations. Figure 5.11 shows the fuel consumption relative to the baseline throughout the optimization process, where a negative value corresponds to a fuel saving. Black square markers indicate feasible configurations, white circle markers indicate unfeasible points. Grey triangle markers indicate configurations for which the

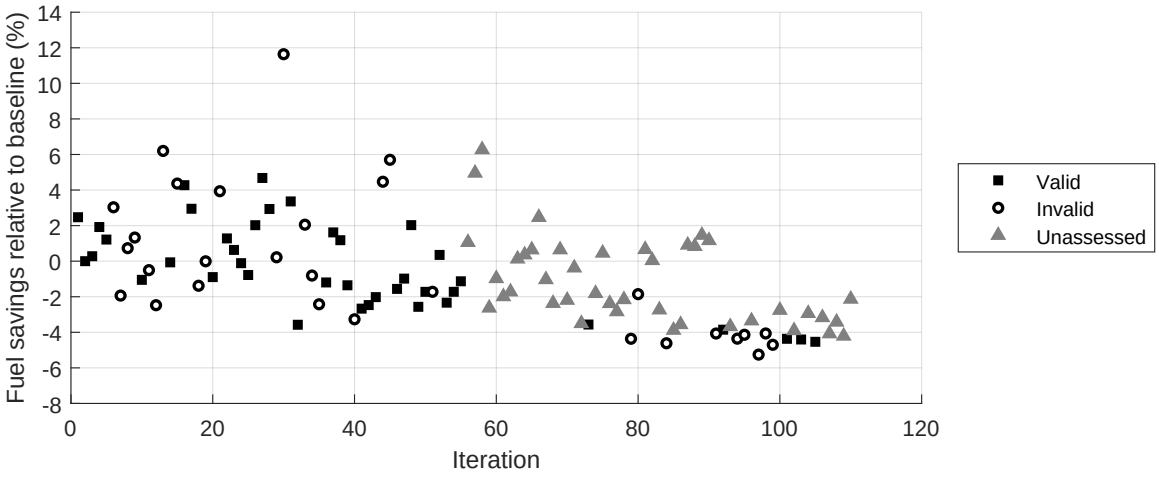

Figure 5.11: Optimization progress for the infill designs regarding the relative fuel consumption.

stress constraint was not assessed since they did not show fuel savings improvement relative to the best configuration at that point of the optimization. The attained results are seen as satisfying, considering the available resources, rather than a rigorously

defensible globally optimal result. Table 5.7 below shows the relative changes of the significant parameters of the best optimized versus baseline configuration, as well as the maximum occurring stress.

Δ AR	16.8%
Δ Weight	2.74%
Δ Fuel consumption	-4.53%
Maximum Stress	259 MPa

Table 5.7: Optimal configuration differences relative to baseline configuration

Figure 5.12 shows a comparison of the outer shapes clearly showing the noticeable AR increase above the baseline. It is expected that with further continuation of the optimization additional improvement could be achieved, based on the progress of the optimization specifically in the end phase, where the average improvements increased significantly compared to the baseline configuration.

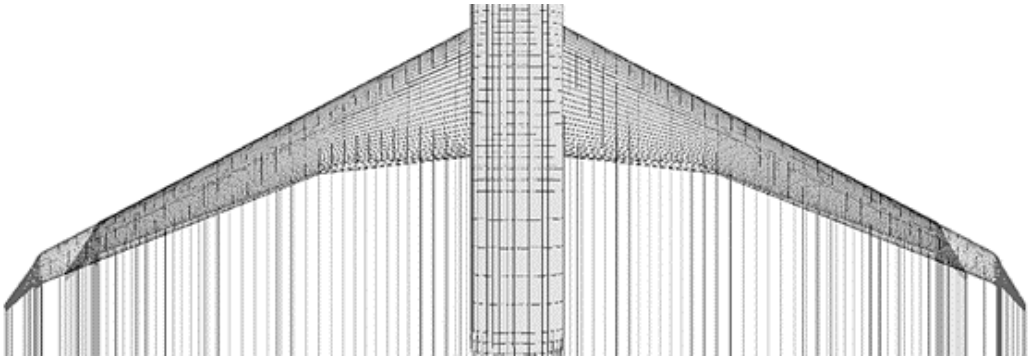

Figure 5.12: Overlapping comparison of the baseline (dark grey) and the optimized wing (light grey) configuration planforms.

5.2.4 Concluding Remarks

In order to reduce the computational costs of MDO of a typical medium range commercial aircraft including flutter constraints, studies were performed on the most likely active constraints in the MDO problem and on the validity and accuracy of estimating drag and stress using low-fidelity FSI followed by one iteration high-fidelity FSI versus a converged high-fidelity FSI calculation.

The results show that for this problem the active constraint is only one of the load cases, which is the 2.5g pull up at MTOW. The other load cases considered

appeared less severe and therefore were left unassessed during the MDO procedure. The flutter constraint is also not active, although the effect of deformation on the flutter margin reduction is visible in the results. As novel aircraft configurations tend towards higher aspect ratios with more flexible wings, it is expected that dynamic aeroelastic behavior will become a more prominent design driver. Slenderer wings are more prone to high deformations, closing into the flutter margin. Altering the number of (structural) design variables is expected to bring the stress distribution closer to the boundary along the whole wing (outer wing), potentially reduce the wing mass and increase the authority of the flutter margin as a constraint driver.

Drag evaluation in the cruise case can be performed using the low-fidelity FSI followed by one high-fidelity FSI. The low-fidelity FSI allows speed-up of the deformed shape calculation to an acceptable level of accuracy when compared to a converged high-fidelity FSI run. Maximum displacement differences between low-fidelity FSI and after one high-fidelity FSI iteration are generally below 3%, and tend to be reduced for the converged high-fidelity FSI results. Differences in drag and L/D between the first high-fidelity FSI iteration and the converged high-fidelity FSI were estimated to be around -1% and 0.5% for the best configuration in the analyzed set.

Stress evaluation can also be performed using the same procedure, however not with the same level of accuracy, yet still conservative. Converged high-fidelity FSI results tend to redistribute the loads for this wing geometry and reduce the stress to values between the low-fidelity FSI result and the first high-fidelity FSI iteration results. Unfortunately, the low-fidelity FSI load predictions alone are not accurate or conservative enough to dismiss the high-fidelity evaluation.

A further reduction in computational costs was attained using a surrogate based MDO approach. Using surrogate models for both objective function and active constraint, an expected improvement approach was used to determine the surrogate models infill configuration designs and the best feasible configuration after 110 iterations was chosen as the optimization result. For the different used models and to evaluating parameters, the chosen approach is a viable alternative compared to more complex approaches like adjoint class methods.

The used models in the multi-disciplinary design optimization methodology were of different levels of fidelity to evaluate different disciplines. Therefore, one has to keep in mind that the results contain some uncertainty. The use of a limited number of design variables is another reason for obtaining a direction of the design rather than an exact optimum. Further, surrogate modelling approach support an identification

of regions of interest for an optimization. However, due to the relatively low number of evaluated designs in the design space does not allow the assumption of a global optimum region. It can therefore be concluded from the obtained results, that a direction for a HARW design is given, yet a further potential improvement with other approaches, such as adjoint methods, can be attainable.

In summary, the outcome of the optimization and the consideration of different levels of fidelity and complexity was manageable in a straightforward way. After all, the chosen configuration had an increase in AR of 16% and yield a reduction in fuel consumption of 4.5% while increasing the wing weight by 2.7%.

5.3 Multi-disciplinary Design Optimization of a Strut-braced Wing Aircraft

The analysis and optimization of a SBW concept was the second part of the project with the industrial partner. The requirements, objectives and methodology were similar to the process of the conventional aircraft optimization. Some changes naturally occur due to the differences in the overall concept of the SBW. They will be mentioned in the respective section.

Yet again, the surrogate based multi-disciplinary design optimization with adaptive sampling methodology was applied to the problem. The results are analysed in the same fashion as the HARW application at the same operating conditions. Further, a comparison of the optimization results of the HARW and the SBW is performed regarding the best performance-cost compromise.

5.3.1 Problem Description

Originating from the conventional baseline configuration, an initial SBW concept is generated. This SBW baseline was manually engineered to be a feasible design from the constraint point of view. Primary calculations were used to establish suitable design variables and their limits, which are characterized further below. The wing aspect ratio of the baseline SBW was adjusted to 14 and its area was maintained from the conventional low wing configuration for comparability.

The flight profile is a simple cruise-to-destination mission, with a design mission range of 2000nm with an additional hold segment reserve for 45 min. For the optimization the segment of interest is the cruise flight condition at mid flight and

a high load case, namely a 2.5g pull-up maneuver at a speed of Mach 0.76, to ensure structural soundness. The corresponding data is summarized in Table 5.8. The remaining components were maintained from the conventional design, including

Parameter	Value
Cruise altitude	36,000ft [11,000m]
Cruise speed	Ma 0.7 [206.5m s^{-1}]
Maneuver (2.5g) altitude	25,000ft [7,620m]
Maneuver (2.5g) speed	Ma 0.76 [235m s^{-1}]

Table 5.8: Cruise and 2.5g pull-up maneuver flight conditions

fuselage and the empennage with T-tail. The horizontal tail was again adapted to match the wing geometric changes and maintains a constant volume coefficient.

Non-structural and system masses are taken from the conventional baseline configuration and, where necessary, adapted to fit the SBW configuration. This includes the storage of fuel in the wing, where the volume above the passenger cabin is free of fuel. Further, system masses with regards to high-lift devices are adapted to fit in the more slender wing configuration. The propulsion system is adopted from the conventional configuration, where jet engines are mounted to the fuselage rear and propulsion data is given for the jet engine, with respect to thrust requirements and flight condition.

The wing structure is similar to the conventional design, being box like and made of aluminum alloy. The parametrization for the optimization contains variables affecting both, aerodynamic and structural properties, as well as on a secondary level their interdependent characteristics due to flexibility.

The airfoil shape along the wing is maintained constant throughout the optimization process. Acknowledging the limited aerodynamic potential benefit, it provides the general direction of the optimization process and allows the comparison with the HARW configuration.

The MDO procedure considers the same objective as the HARW MDO, aiming towards reduction in both operational and manufacturing costs. Constraints are posed by the maximum allowable structural stress for a high load case, namely a 2.5g pull-up maneuver, as well as a minimum flutter margin. The neglected constraints compaired to the HARW MDO stem from the investigation of the constraint cases in the HARW approach and the conclusion that the 2.5g load case is the constraint driver. For the flutter estimation, the flexible wing is deformed under the 2.5g load at maneuver

speed. This optimization problem can therefore be stated as following:

$$\begin{aligned} &\text{minimize} && f(\boldsymbol{x}) = Aw(\boldsymbol{x}) + Bc(\boldsymbol{x}) \\ &\text{w.r.t.} && \boldsymbol{x} \\ &\text{subject to} && \sigma(\boldsymbol{x}) \leq \frac{\sigma_{yield}}{SF} \\ & && \frac{FM \times DS - FS(\boldsymbol{x})}{DS} \leq 0, \end{aligned} \tag{5.2}$$

where w and c are the objectives with respect to manufacturing cost (mass) and operational cost (fuel consumption due to thrust requirement), respectively. The factors A and B correspond to the weighting between the two objectives, with the same weighting as the HARW of $A/B = 1/3$. The stress σ is constrained by the maximum yield strenght σ_{yield} of the used material and a safety margin (SF). The flutter margin (FM) is imposed by the constraint that the dive speed (DS) needs to be sufficiently lower than the flutter speed (FS).

Listed in Tab. 5.9 are the geometric, aerodynamic and structural design variables with their description and respective minimum and maximum values. The area and aspect ratio (AR) factor in the design variables are oriented on the initially generated configuration as a geometry, with an area of $75m^2$ and AR of 14. As stated before, this design was manually generated to not exceed any constraints and be comparable with other SBW concepts, such as the ones studied in [49; 54]. Thus, the area can be modified between $52m^2$ and $82m^2$ and the AR between 12 and 25. This allowed a wide range of designs to be explored.

The structural thicknesses of the skin and spar are linear for the inboard and outboard wing segments. The strut is reinforced around the joints (fairing and wing) and has a constant thickness along its length. To provide more design freedom the optimization process, the location along the strut where the reinforcement of the joints start are design variables as well. The twist distribution for the wing is bi-linear, meaning they are described by continuous functions composed of two linear segments with different slopes. The location of slope change is a design variable itself, referred to as twist kink position. Further, the strut contains a twist variable near the wing joint, to mitigate possible aerodynamic interference effect between the wing and strut. Shown in Fig. 5.13 is a graphical representation specifically for the structural parameters for a better understanding.

Category	Design variable			Description
Geometry	x_1	0.7	1.1	Area factor [-]
	x_2	0.85	1.8	AR factor [-]
	x_3	0.2	0.35	Taper ratio [-]
	x_4	10	20	Wing sweep [^{o}]
	x_5	0.1	0.3	Strut position x relative to chord [-]
	x_6	0.5	0.69	Strut position y relative to wing span [-]
	x_7	0.1	0.3	Strut position z relative to chord [-]
	x_8	0.3	0.5	Strut chord relative to wing chord @joint [m]
Aerodynamic	x_9	0.2	0.8	Kink position twist relative to wing span [-]
	x_{10}	0	4	Wing twist root [^{o}]
	x_{11}	-1	2	Wing twist kink [^{o}]
	x_{12}	-2	1	Wing twist tip [^{o}]
	x_{13}	-2	0	Strut twist [^{o}]
Structural	x_{14} & x_{18}	0.002	0.022	Skin & spar thickness inboard root [m]
	x_{15} & x_{19}	0.005	0.013	Skin & spar thickness inboard joint [m]
	x_{16} & x_{20}	0.008	0.03	Skin & spar thickness joint [m]
	x_{17} & x_{21}	0.0005	0.008	Skin & spar thickness tip [m]
	x_{22}	0.02	0.1	Strut thickness @joint [m]
	x_{23}	0.05	0.25	Kink position strut thickness @joint [-]
	x_{24}	0.008	0.05	Strut thickness main [m]
	x_{25}	0.03	0.07	Strut thickness @fairing [m]
	x_{26}	0.75	0.95	Kink position strut thickness @fairing [-]

Table 5.9: Design variables for the wing parametrization and optimization

5.3.2 Multi-disciplinary Design Optimization Process and Methodology

The MDO process is the one described in section 5.1 and will not be repeated in detail here. The most important aspects are the use of low-fidelity models for the aerodynamic and structure for the FSI process. Additional, a high-fidelity RANS based CFD evaluation can be employed for accurate drag predictions. Fuel and non-structural masses are modelled as mass points, rigidly linked to the closest structural element nodes and relocated within the FSI process.

The meshing procedure for the RANS CFD is automated, refinements are added around the leading and trailing edges of the wing and strut. A refinement is also added around the joints of the strut near the wing and the fuselage, to capture flow details in those regions. A mesh convergence study was performed on the baseline to estimate a reasonable mesh size, balancing performance and precision. The results are shown in Table 5.10. It should be noted that flow fields with more than 14 million cells could not be solved due to memory limitations. Throughout the optimization,

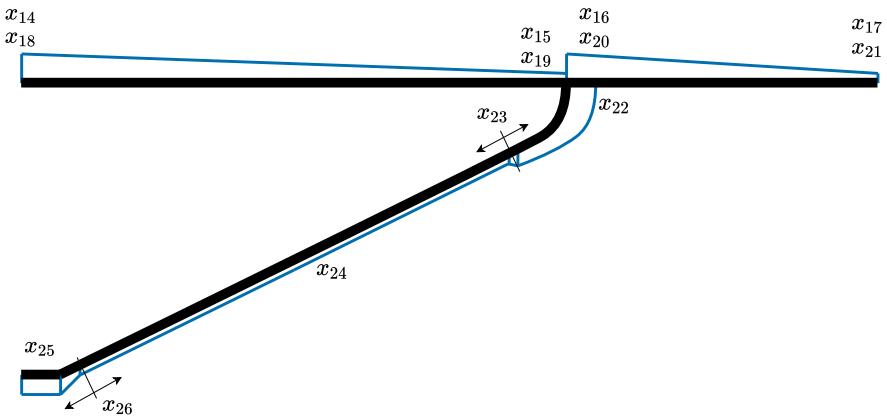

Figure 5.13: Graphical representation of the structural design variables according to Table 5.9

the different models contain between 9.5 million and 11 million cells, depending on the geometric shape of the design throughout the optimizations. The computational costs for a single run depended on the load case and flow condition. For the the cruise flight condition it was 7 hours, while for the 2.5g load case it was 9 hours. A large amount of the time was used for the automated mesh generation. For the simulations a 60 core server[2] was used. To obtain a trimmed solution for the aircraft, the preceding

	Number of cells	C_L [-]	C_D [Drag counts]
Coarse	∼5.8 Mil.	0.747	401.0
Medium	∼10.2 Mil.	0.760	375.0
Fine	∼13.0 Mil.	0.759	379.6

Table 5.10: Mesh convergence for the SBW RANS CFD runs

calculations with horizontal tail volume coefficients introduced for the HARW were employed.

For the flutter estimation, the SOL145 solver of NASTRAN was again employed. The structural and aerodynamic model were modified appropriately to match the required boundary conditions. This included the clamping at the roots of wing and strut, as well as the stiff connection at the wing-strut joint. The aerodynamic panel were refined to better resolve the curvature of the strut.

The surrogate based optimization included again an adaptive sampling approach, as it showed satisfactory results for the HARW. It was, however, acknowledged, that

[2]Intel i7 4870 @2.4GHz

the posed problem was more challenging due to the number of design variables. The design of experiments was extended to contain more samples in the initial phase. The ordinary Kriging modelling approach was seen as sufficient, as the number of designs variables was still within a reasonable range. Further, the benefits of the possibility of using the uncertainty quantification was considered beneficial for the problem. Compared to the HARW MDO, the computational budget was extended to 150 iterations due to the larger amount of design variables.

5.3.3 Multi-disciplinary Design Optimization Results

Fig. 5.14(a) shows the evolution of the improvement in fuel consumption and overall objective function along the optimization iterations. A 0% improvement corresponds to the baseline configuration. Fig. 5.14(b) visualizes the fuel benefit of the infill samples throughout the optimization process.

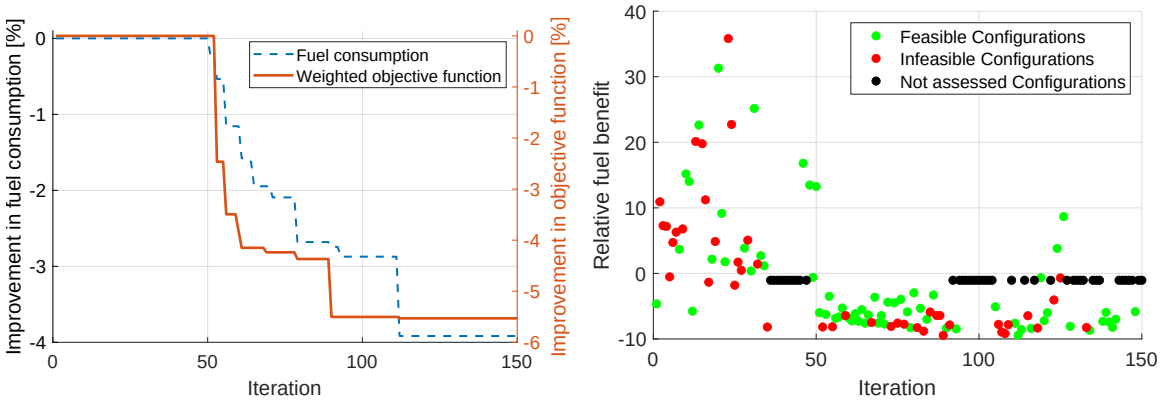

(a) Objective function convergence during optimization

(b) Fuel consumption for database samples

Figure 5.14: Iteration progress of the optimization for the SBW concept

As can be seen, the improvement for the objective and the fuel consumption are strongly correlated, as the weighting between the manufacturing and operational costs tends towards the latter objective. The convergence graph further displays the typical behaviour of SBO, where with the initial sampling and few additional infill samples the objective can be reduced significantly and jumps in the objective occur when promising areas are found. However, the restricted computational resources prohibit a more extensive exploration and exploitation process, as a balance needs to be found to identify areas of interest with the possible global optimum as well as local minima.

As the surrogate model contains uncertainty and is an estimator, not every proposed design is able to improve the objective or fulfill the constraints. Therefore, a number of samples is evaluated according to the scheme mentioned before, where some single assessments are not performed. Nevertheless, the obtained information about the performance is fed back into the meta modelling process to improve the corresponding models in such a way that for the next optimization iteration a new infill point based on the updated knowledge can be proposed. The optimization was terminated after 150 iterations, as the computational resources were depleted and no further improvement was seen in the later iterations.

The design variable distribution of the baseline and the optimized design is shown in Fig. 5.15. Additionally, other comparably good samples taken from the optimization process are shown. Those were samples with different AR where the surrogate optimizer was exploring regions of interest throughout the iterations. The second design variable is a scaling factor for the aspect ratio (see Table 5.9). This is the expected main driver for the fuel benefit and where the exploration of the design space is eminent. The structural design variables are the main driver for fulfilling the constraints and reducing the weight. Consequently, it reduces the fuel consumption and therefore improves both objectives. In a continued procedure, it is expected that those regions would be further exploited. What can be noticed from the design variables is a general

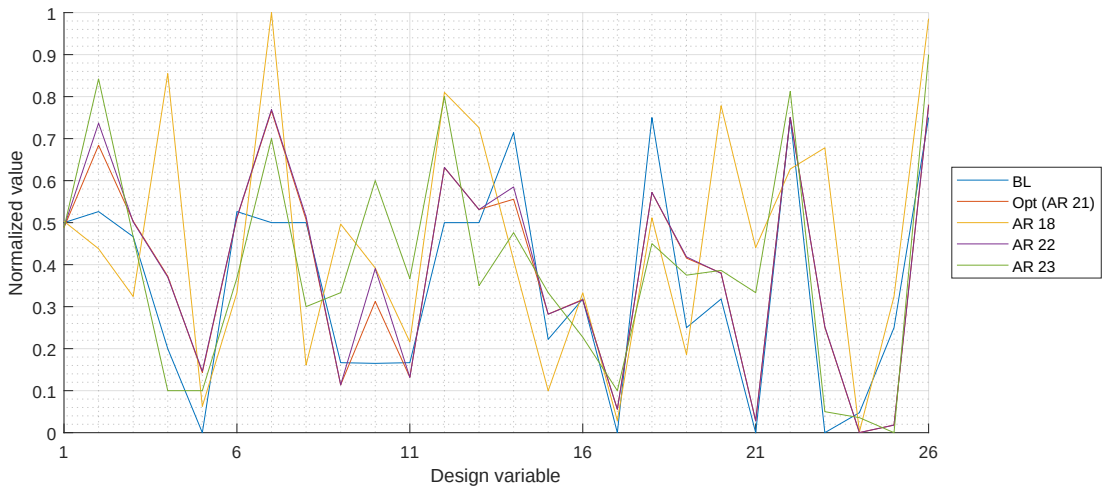

Figure 5.15: Design variables distribution for the baseline and optimized designs

trend for some of them in the global range and in dependency of the aspect ratio. For one, the area of the baseline configuration does not change significantly, displaying an already satisfying value to support the aircraft weight. Additional design variables

that are noticeably tending towards a small range of values are:

- x-position of the strut: a forward position is beneficial for the induced twist due to deformation as the load is reduced and shifted more inwards;
- thickness of spar and skin at the tip: the minimum value is related to manufacturing constraints (minimum thickness) and the lower load at the outer wing allows for a lighter structure;
- strut thickness: as the wing load is distributed between the cantilevered wing and the strut, the strut can have a lighter structure, allowing for a lower structural thickness Possible issues can be buckling and bending under negative load, which needs to be further investigated.

Furthermore, those results show that optimized design seems to follow a trend where feasible designs with a low objective are within a band of design limits. One could conclude that the limits initially set for the optimization can be contracted to limit the design space. Thus, with limited computational resources this may allow more goal oriented exploitation. However, this would oppose the initial objective to explore the designs space to get a broader picture.

Regarding the constraint functions, a comparison between the stress distribution of the baseline and the optimized configuration is made and shown in Fig. 5.16. The critical areas for both designs are the joints of the strut with the wing and the fuselage, as well as the wing root. While the baseline had the constraining stress located at the joint, the optimized design is close to the boundary for the three critical locations. The stress at the outer wing section, where it behaves like a cantilevered beam, has a distinct margin towards the constraint. As the structural thickness at the wing tip is already at the lower boundary (related to manufacturing limitations), no additional benefit can be gained there. However, a more elaborate thickness distribution may be chosen to further optimize this region. This would imply an increase in the number of design variables, which is not desirable at this point and therefore was not contemplated. It should be noted that the joints are stiff rather than pinned connections. Distribution of the reaction load towards the wing is beneficial for the strut design, since a lower thickness is possible and consequently the wetted area is reduced.

Another aspect of the optimization was an estimation of the flutter speed and to ensure a preliminary safe flutter margin. Considering the limited accuracy of

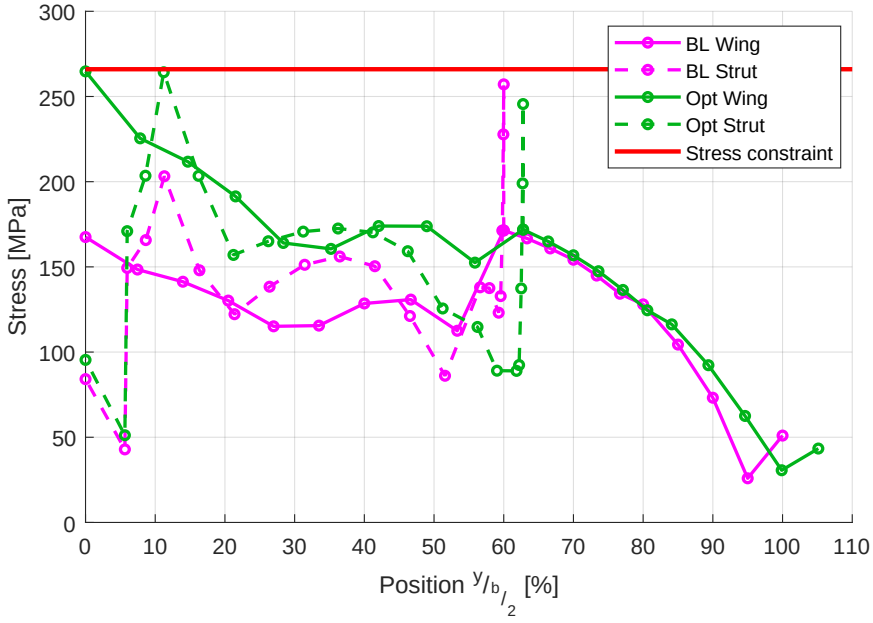

Figure 5.16: Stress distribution of the baseline and the optimized configuration for the SBW

the calculation at this design stage, the flutter boundary is rather an indicator to which extend a change happens with respect to the baseline configuration. A more comprehensive assessment is required in later design stages when detailed layouts are available. However, the mutual comparison gives an initial picture considering the difference between rigid and flexible considerations for the baseline and the final design.

Visualised in Fig. 5.17 is the flutter boundary together with the flight envelope. It can be seen that both designs have a comfortable margin towards the required minimum flutter speed. A difference can be noticed between the rigid and flexible structure, where with the displacements of the wing the aeroelastic response is changed towards the boundary. This is more significant for the baseline design. The visible spike in the baseline curve is related to a change in the responsible mode for the flutter mechanism. The active mode at higher speeds is close to the zero damping threshold and only surpasses it marginally but earlier than the second responsible mode at high speeds. Despite the change in mode at higher speeds and the shrinking of the margin for the flexible wing, there is a sufficient safety gap between the flight envelope and the flutter boundary. The expected influence of flexibility could be observed, but was not critical or constraining in this study.

Final key results are summarized in Table 5.11, showing the relative change to

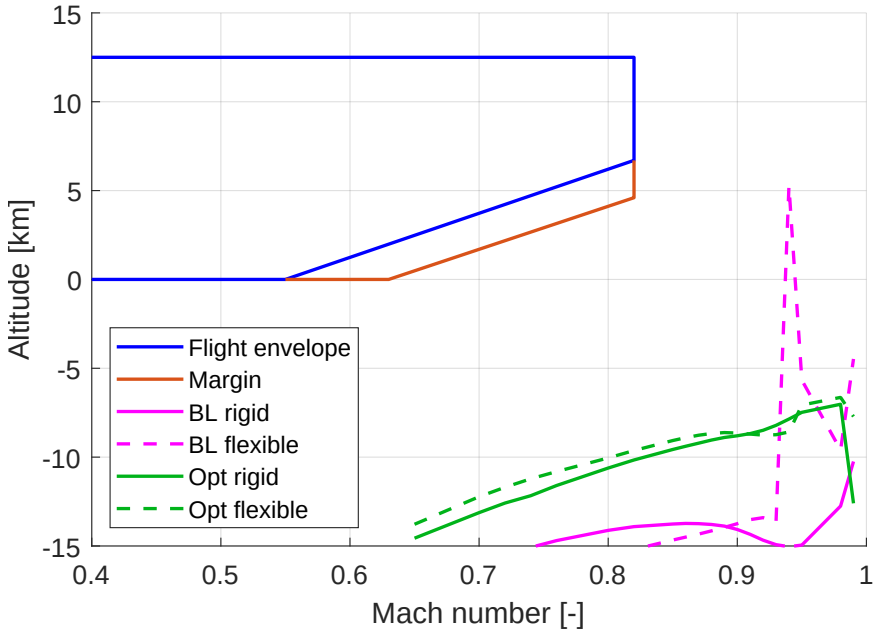

Figure 5.17: Flutter boundaries for baseline and optimized configurations considering rigid and flexible structures

the baseline. As initially stated, the SBW baseline is a derivation of a conventional aircraft. Therefore, the benefits towards this design are also included to show the overall performance benefit for novel aircraft. Comparing the outcome of the SBW optimization with the initial conventional design provides a fuel benefit of 9%, with an increase in wing weight from 2175kg to 3270kg (50%) and therefore an increase in MTOM of 3.5% (29890kg to 30940kg). This agrees with previous research [49; 50; 263; 264; 134; 57], where comparable procedures were performed, although a lower overall benefit was obtained in this work. This can be seen as the influence of the flexibility consideration, as above works focused either on undeformed structures or, if flexibility and even non-linearities were considered, lower fidelity models were used for the aerodynamic assessment and therefore a different magnitude of benefit can be obtained.

Considering the limited available resources, the obtained results are seen as satisfying, even though the found solution is not a rigorously defensible global optimum. With the utilization of different levels of fidelity for the evaluation of multiple disciplines, the obtained results can provide guidance towards global directions for novel aircraft designs. With higher computational power the described methodology can be utilized to increase the level of fidelity or include further design variables for a

Design spec	Baseline SBW	Optimized design SBW
Area $[m^2]$	66.9	66.5
AR [-]	19	21.2
Span $[m]$	35.7	37.6
MAC $[m]$	2.09	1.98
Taper ratio [-]	0.27	0.275
Wing mass $[kg]$	3,600	3,270
MTOM $[kg]$	31,270	30,940
L/D [-]	20.2	21.1
α_{trim} [deg]	1.95^o	2.42^o

Table 5.11: Comparison of the MDO SBW with the baseline SBW

refinement in design. Using the acquired outcome can be utilized as starting point for further optimization approaches that, opposing to surrogate based optimization, can focus more on a local improvement of a design. Here, the employment of adjoint method can prove feasible. However, it is expected that a higher number of infill points a further improved design would be obtained with the surrogate modelling approach, given the = number of design variables and the non-linear behaviour of the multi-disciplinary objective.

Chapter 6

Comparison of Novel Aircraft Configurations and Influence of geometric Non-Linearities

In the last chapter, the resulting optimized aircraft were analysed regarding their respective optimization outcome. In the following chapter, a short mutual comparison of the optimized aircraft is discussed. Further, the influence of geometric non-linearities is investigated, since it is expected to play a more significant role for novel configurations that utilize long and slender wings for aerodynamic performance improvement.

Modified excerpts from the articles "On the Multi-fidelity Approach in Surrogate-based MDO of HARW aircraft" [230] and "Optimization and Comparison of SBW and HARW with non-linear Aeroelasticity" [231] are partially used in this chapter. Situated in the thesis environment, the content is elaborated and put into context to suit the flow of this research.

6.1 Comparison of optimized Designs for a High Aspect Ratio Wing Aircraft and a Strut-braced Wing Aircraft

Following, the most important outcomes are summarized and afterwards both optimized configurations, the SBW and the HARW, are mutually compared. Both configurations were analyzed and optimized towards the same multi-objective goal. A

surrogate based optimization with an EGO approach was used to obtain the improved designs. While the number of design variables for the HARW was lower than for the SBW, 14 compared to the 26, they were used in a similar fashion to describe the geometric, structural and aerodynamic design.

The computational budget endorsed for both processes were 110 and 150 iterations for the HARW and the SBW, respectively. The decision for a higher number of iterations for the SBW stems from the higher number of design variables. Both did not achieve remarkable improvements in the latest iterations and the results were seen as satisfying, even though it was acknowledged that the found design was likely not a global optimal result given the computational resources employed.

The evaluations contained the assessment of the cruise flight performance for the objective, stress evaluations for the constraints and the estimation of the flutter boundary. Additionally, the HARW process included an assessment to which extend the constraints are likely to be active to reduce the computational costs further. For the SBW it was adopted and the constraints were reduced from the beginning towards the high load constraint.

A detailed overview of the data for the HARW and the SBW regarding their benefits compared to the baseline can be found in Table 6.1. Therefore, the differences

Design spec	Baseline HARW	Optimized HARW	Optimized SBW
Area $[m^2]$	57.0	62.2	66.5
AR [-]	12	14.1	21.2
Span $[m]$	26.1	29.7	37.6
MAC $[m]$	2.77	2.66	1.98
Taper ratio [-]	0.27	0.27	0.275
Wing mass $[kg]$	2,175	2,900	3,270
MTOM $[kg]$	29,890	30,700	30,940
L/D [-]	18	19.9	21.1
α_{trim} [deg]	2.71^o	2.90^o	2.42^o

Table 6.1: Comparison of the optimization results for the HARW and SBW with the baseline both design have as reference

between the optimized results are clearly visible. The HARW could improve the performance compared to the baseline configuration, with an increase in L/D of 10.6%, while the MTOW was increased by 2.7%. The SBW concept, derived on the same basis as the HARW could further improve the objective, a blend of the wing mass and the fuel mass. The L/D improved by 17.2% compared to the baseline and 6.0%

compared to the optimized HARW. However, as expected from a structural point of view, the SBW, while aerodynamically more beneficial than the HARW counterpart, has a higher wing mass due to the additional strut structure. Therefore, the MTOW compared to the baseline increased by 3.5%. Despite the possibility to decrease the mass of the inner wing, the added mass by the strut jeopardizes the total wing weight. It is therefore a compromise and balance to be found, what plays a more significant role in the design for a novel configuration, the structural mass, as metric for the manufacturing costs, or the fuel consumption, as metric for the operational costs.

Furthermore it needs to be acknowledged again that the obtained results are an outcome of an optimization with different levels of fidelity. The mixed use of high-and low-fidelity tools for computationally more expensive aerostructural evaluations accelerates the optimization process, but contains the computational time at a reasonable level. At the preliminary design stage this is seen as feasible approach to reduce the computational cost by allowing some uncertainty in the results but give a more detailed insight. The cautious use of high-fidelity methods at early design stages can provide insight and directives, however, a detailed analysis is scarcely possible. With a low number of design variables, yet those being carefully chosen to provide some global insight, the assessments and evaluations can be utilized to steer novel aircraft design.

6.2 Assessment of geometric Non-Linearities for flexible Designs with High Aspect Ratio Wings

With the increasing flexibility of slender wings, higher deformations are a consequence for all flight conditions. Those large displacements can lead to geometric non-linear effects. By considering those in the aeroelastic assessment, it is of interest to evaluate if the linear assessment is conservative and to identify possible further optimization potential. This was assessed in the last part of the project, where the former optimized aircraft designs were investigated regarding the influence of geometric non-linearities.

Due to possible changes in displacements for flexible structures, the expected benefit for the fuel consumption or the stress distribution might not be observed and thus a costly redesign in later stages might be needed. Likewise, if the aircraft is not able to meet the flutter margin requirements, further reiterations are necessary.

A comparison of the linear and non-linear structural model regarding the deforma-

tion differences and flight loads could be performed. The quantification of differences stemming from linear vs non-linear structural based FSI analyses is presented for both configurations, which including static (cruise performance) and dynamic (flutter speed boundary) aeroelastic calculations.

Since this procedure is related to high computational costs, only a limited number of calculations could be carried out and the acquired insight allows only confined conclusions. However, it provides an important initial insight and offers some essential deductions.

6.2.1 Utilized Models and Problem Description

The optimized HARW and the SBW are assessed regarding the influence of geometric non-linearities. The assessment includes the mid-flight cruise performance, the high-load case stress behaviour and the effect on the flutter boundary. The flight conditions are the same used in the optimization, which can be found in Table 5.8.

In order to better understand differences in performance and the influence of flexibility, additional designs were included in this final assessment. They were taken from the data pool of the optimization process and are distinguished as almost similar good examples as the optimization results but with a higher aspect ratio, again to qualify the influence of the slenderer wing structure regarding deformation and non-linear structural behaviour. The HARW was complemented by a design with an AR of 15.5 (HARW+), for the SBW the additional design has a considerably higher aspect ratio of 22 compared to 19 of the optimized result, while the multi-disciplinary objective is only slightly less than the best configurations.

When considering geometric non-linearities in the structural model, the stiffness of the structure becomes dependent on the displacement. The iterative process to obtain the equilibrium state of the structural model within the FSI procedure is implemented in the framework introduced in section 2.1.2. The computational cost for the non-linear assessment was significantly longer than for the linear one. For the conventional HARW this compares with 15 min to 120 min for the linear and non-linear cases, respectively. The SBW took even more time to converge, as the strut joints at the wing and fuselage pose additional computational challenges regarding force and displacement convergence, and took up to 24h for a single run.

6.2.2 On Cruise Performance

Table 6.2 summarizes the result of the cruise condition evaluation considering the linear and non-linear structural model for the HARW and the SBW concepts. Except from the non-linear treatment, both models are treated identical, with the same structural layout, with a FSI procedure and a subsequently drag assessment, using CFD methods. Both configurations show a penalty considering geometric non-linearities. They are slightly more distinct for the SBW concept. Despite the slenderer structure, the performance penalty for the designs with the higher aspect ratios is lower than for the lower aspect ratio configurations.

The following explanation is given for this result contrary to the expectations: The designs with the higher aspect ratios are taken from the pool of designs created during the optimization. While they show a good performance they are not as optimized as the chosen solution. Thus, from a performance point of view, the non-linear structural consideration is less influential. However, the penalties for all evaluated configurations indicate two aspects of the non-linear influence:

1. the neutralization of a portion of the benefit gained throughout an optimization leads to a lower improvement if the optimization is solely based on a linear structural model;

2. a margin is available for improving a configuration considering non-linearities.

	L/D Linear	L/D non-linear	Δ
HARW	19.9	19.9	0.0 %
HARW+	19.8	19.7	-0.5 %
SBW	21.5	21.1	-1.9 %
SBW+	20.6	20.5	-0.5 %

Table 6.2: Performance results for the trimmed 1g cruise flight condition

The differences of the performance originate from the slightly different behavior in the deformation. Fig. 6.1 shows the displacements for the optimized HARW and Fig. 6.2 for the SBW configuration, respectively. They include the vertical displacement (out-of-plane bending), horizontal displacement (in-plane elongation), sectional twist and dihedral behaviour. Whereas most of the differences are hardly distinguishable, they are already enough to affect the performance.

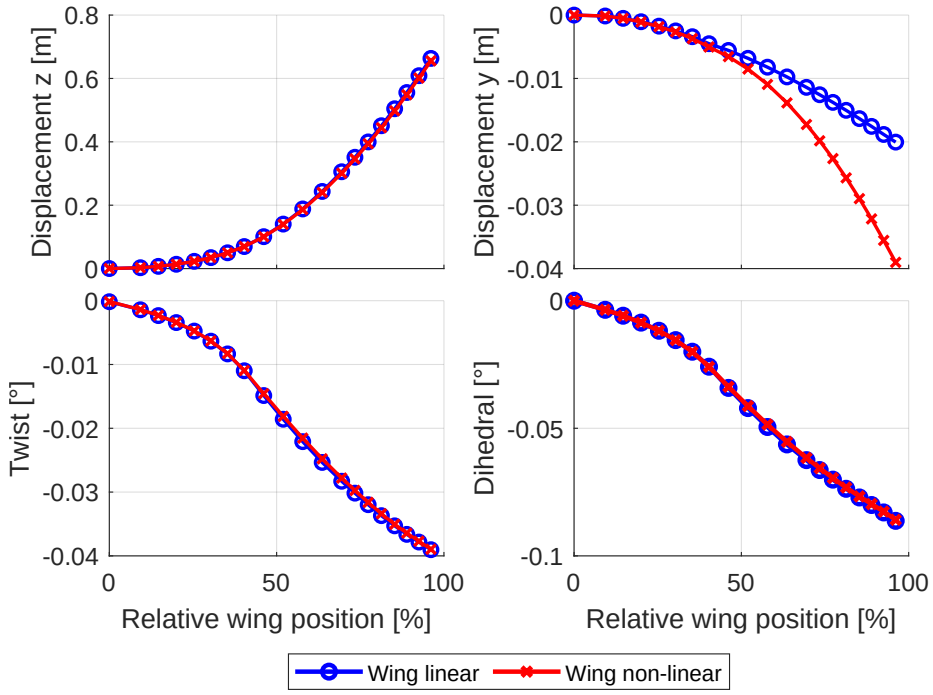

Figure 6.1: Deformation comparison in terms of displacements in z- and y-directions, twist and dihedral angles between linear and non-linear simulations for the HARW configuration

For the HARW the most visible difference is the displacement along the wing span. This is the wing shortening due to the non-linear behaviour and governs a slight change in the load distribution, as a higher AoA is required. While it is not as evident for the cruise case with low displacements, higher deformation influence the difference between the linear and non-linear displacement more and consequently the resulting performance.

Likewise, the displacements of the main wing of the SBW are not very obvious, except for the shortening, showing as a delta in y-displacement. However, a more distinct difference is seen for the strut behaviour. While the linear strut is arching under the load resulting in higher deformation for horizontal, vertical and dihedral directions, the non-linear strut does not show this behaviour. This is explained due to the structural layout, where deformation of the construction is more complex compared to a cantilevered wing. The geometric shortening effect of the strut interacts with the vertical displacement of the wing at the junction. While this movement compresses the strut, the geometric shortening relaxes this behaviour, which can be seen specifically in the dihedral and wingspan displacements for the strut. The twist is almost not

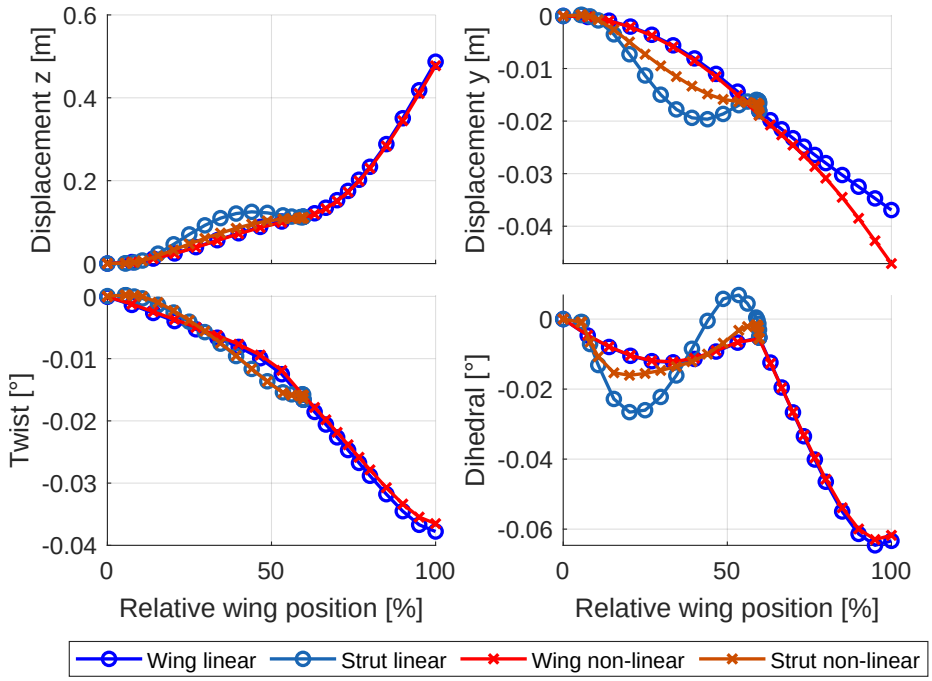

Figure 6.2: Deformation comparison in terms of displacements in z- and y-directions, twist and dihedral angles between linear and non-linear simulations for the SBW configuration

affected by the non-linearities for either the main wing or the strut.

Despite the influence of the geometric non-linearities on the performance does not seem to be too substantial, it is perceptible. Furthermore, even the low penalty of up to 2% if compared to a linearly optimized design can affect the overall design, as current benefits are in the range of 10% to 15% as mentioned before. This means that the expected benefit might be 15% to 20% lower than predicted.

6.2.3 On Stress Constraint

High displacements, emerging at high load conditions, can have a more distinct influence on geometric non-linear effects. Following the results for the stress constraint case are presented and discussed. Table 6.2 provides an overview of the comparison between the linear and non-linear assessments for the high load case. The maximum Von-Mises stress, independently where it appears, and the difference between the computation outcome are given. Further, the vertical wing tip displacement is shown with the percentage of its dissimilarity. More detailed information about the structural behaviour is given below in the discussion together with the visualization. However,

the results summarized in Table 6.2 give a notion about the differences between linear and non-linear assessments for the studied configurations.

	Maximum stress [MPa]		Δ [%]	Wing tip deformation [m]		Δ [%]
	Linear	non-linear		Linear	non-linear	
HARW	254.3	253.2	0.4	1.66	1.66	0.0
HARW+	252.8	251.2	0.6	1.86	1.83	1.6
SBW	260.8	247.3	5.2	0.86	0.85	1.2
SBW+	262.7	250.5	4.6	1.08	1.04	3.7

Table 6.3: Results for the constraint assessment for the non-linear consideration

For the conventional configuration with a HARW the differences of stress and displacements are below 2% for both designs. Since the linear assessment, using the low-fidelity model, provides a more conservative stress prediction for the HARW configurations, an additional safety margin exists. Therefore, if higher computational power was available for carrying out non-linear analyses in the MDO process, this safety margin might have resulted in a further optimized wing design.

For the SBW, the differences are more distinct with a 5% difference for the stress prediction. It is harder to claim a statement for the wing tip deformation, however, a reduction is obtained considering geometric non-linearities. As for the HARW configurations, the linear assessment provides more conservative values, thus a MDO process involving non-linear simulations might have allowed for a lower objective function value. A short note should be given here regarding the general lower vertical displacement of the SBW in respect to the HARW. Due to the stiffer inner part of the wing construction, most of the deformation stems from the outer wing region, which has a cantilevered like behaviour. As this part is shorter compared to a conventional cantilevered wing, the displacements are lower.

Fig. 6.3 shows the stress distribution including the boundary for the optimized HARW (6.3(a)) and SBW (6.3(b)) configurations as well as the displacement information for the designs under load (6.3(c), 6.3(d)) and a 3D view of both configurations (6.3(e) and 6.3(f)).

For the HARW one can notice that the overall trend is similar between the linear and non-linear simulations. However, towards the wing tip the non-linear case displays a lower stress level. Responsible aspects for this behaviour are the stress stiffening effects as well as a different deformation behaviour. The latter causes a change in load distribution, loading the inner wing part slightly more and therefore relaxing the

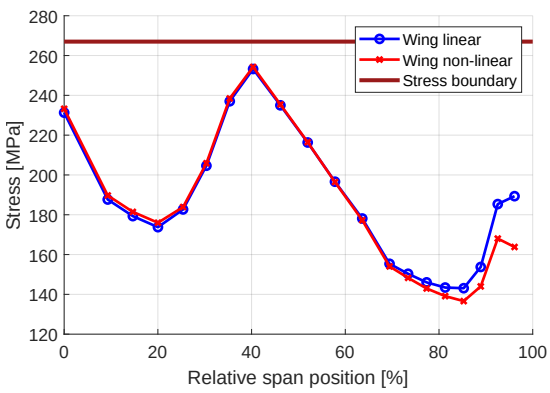

(a) Stress results for HARW

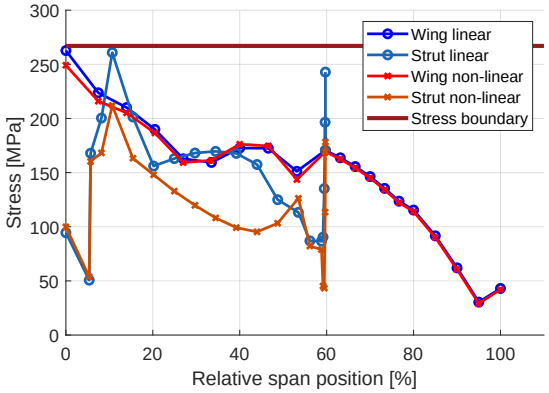

(b) Stress results for SBW

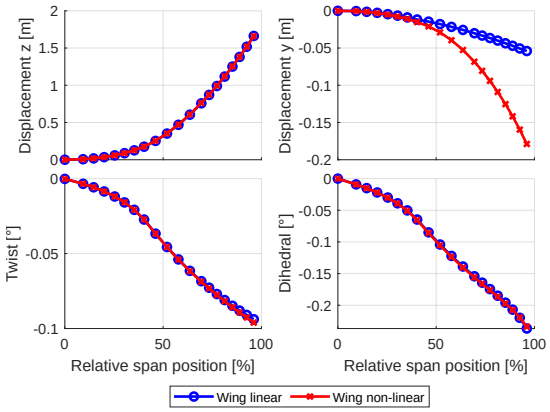

(c) Deformation results for HARW

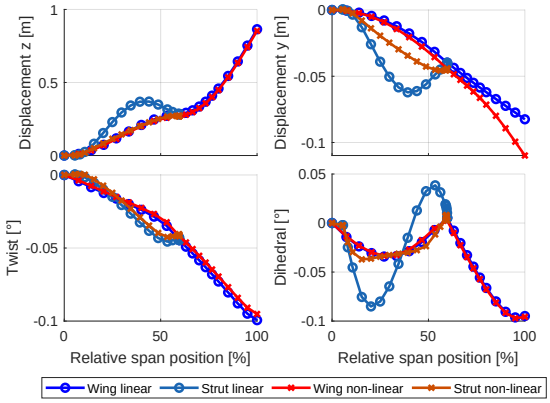

(d) Deformation results for SBW

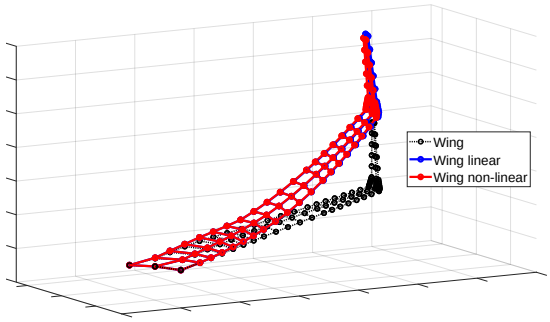

(e) 3D view for HARW

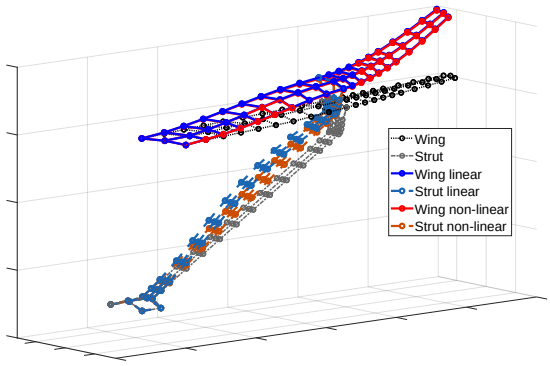

(f) 3D view for SBW

Figure 6.3: Comparison of Stress and displacement results for the linear and non-linear assessment of the HARW and the SBW under the high load flight condition

outer wing region. This load alleviation eases the load on the wing root, causing a lower maximum stress level.

Comparing the results for the SBW assessment (6.3(b) and 6.3(d)), some differences

can be observed. The stress level of the wing-strut joint is significantly lower in the non-linear case. That shows the dissimilarity between the linear and non-linear assessment, where for the SBW the kinematic interaction between the fixed strut and wing influences the stress distribution more significantly. Regarding the displacements, the strut behaviour already recognised for the cruise flight condition is more noticeable. The linear assessed structure arches in a significant fashion, as the joint, due to its stiffness, keeping the strut in the same orientation and imposing a strong dihedral deformation. The non-linear assessed structure does not show the same behaviour. The reason is seen in the geometric shortening of the strut structure in combination with the stiff connection of the wing-strut joint and the vertical displacement of the wing.

Yet again, the difference in twist along the span is less substantial. The non-linear structure has just slightly more twist deformation along the wing towards the tip compared to the linear evaluation. However, a significant difference is obtained in the angle of attack to carry the 2.5g load. While for the linear case the angle is 3.2^o, it is 3.0^o for the non-linear case to provide sufficient lift. Although a slight wing shortening is occurring, the less deformed strut seems to be the reason why the overall angle of attack is slightly smaller in the non-linear case.

Considering the non-linearities in the structural model shows a potential benefit for the stress distribution. While the stress level of wing root is similar, the reduction around the joint region can support a lighter structure, reducing the weight of the structure.

6.2.4 On Flutter Boundary

As previously shown, considering geometric non-linearities influences the displacement behaviour under load. This difference in deformation might also affect dynamic aeroelastic response, such as flutter [265]. The differently deformed designs were investigated regarding those changes and the results are discussed. All estimations were performed without transonic corrections as excessive additional computational time would be required to acquire the CFD solutions for calculating the corrections.

Examining the frequency results of the flutter estimation in Table 6.4 shows a shift in response for some of the mode shapes. The obtained frequencies are for the deformed wing, with the linear and non-linear structural model, respectively. For the HARW the deformed structure considering geometric non-linearities has higher

frequency values for the first mode shapes. On the other hand, the SBW has a significantly different frequency only for the first two modes, while modes of higher order seem to be less affected by the non-linear structure.

	HARW		SBW	
	Linear	non-linear	Linear	non-linear
Mode 1	3.01	3.08	2.88	3.71
Mode 2	8.24	8.44	4.66	4.15
Mode 3	9.66	9.91	6.00	6.02
Mode 4	18.78	19.36	8.94	8.53
Mode 5	24.07	25.10	11.84	11.80
Mode 6	29.90	30.95	15.37	15.40

Table 6.4: Differences for the eigenfrequencies of the deformed wing structures assessed with the linear and non-linear strutural model

Further, identifying the mode shapes for the HARW shows the expected behaviour, where the first and third mode is the first and second bending, the second mode is an in-plane mode shape and the fourth mode is a torsion mode. The flutter is caused by a classic torsion-bending mode.

The SBW has a more complex mode behaviour and the kind of mode shape is not as obvious to identify due to the wing-strut interaction. The first mode is a bending mode for the wing and strut, while the second mode is an in-plane bending for the wing with some bending and torsion influence due to a bending strut. The third mode can be interpreted as the second bending mode for the wing and strut, whereas for the fourth mode, the strut has a distinct bending component, while the wing has a strong torsion portion with some bending due to the strut interaction. For higher modes, the shapes are more complex and it is challenging to categorize them into the classical mode shapes.

Fig. 6.4 shows the flutter boundary for the flexible wing, with the linear and non-linear structural model. A change is visible for both configurations, the HARW and the SBW. The shift of the flutter boundary due to geometric non-linearieties is small for the HARW. While for the optimized configuration the non-linear structural model results in a configuration less prone to flutter, the design with the higher AR has a slight shift towards the allowed flutter margin.

For the SBW, both designs (SBW and SBW+) show a reduction in the flutter margin when considering the non-linear structural model. However, the flutter boundary has a distinct distance from the flight envelope and flutter is not a constraint driver.

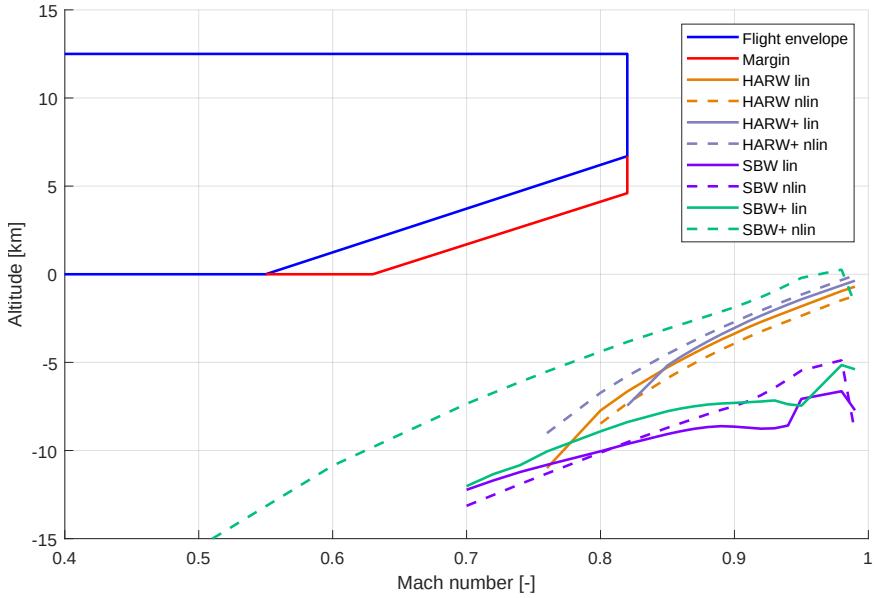

Figure 6.4: Flutter boundary comparison for the linear and non-linear cases

6.2.5 Conclusion

Novel aircraft with a high aspect ratio to increase their aerodynamic efficiency can be affected by geometric non-linear effects due to their flexibility. Therefore, optimized designs were assessed under the aspect of performance penalties considering geometric non-linearities.

It could be seen that despite small changes in displacements due to loads the benefit obtained throughout the optimizations was decreased. A reduction in cruise flight efficiency for both concepts was the consequence. Also, the behaviour under a pull-up maneuver changed slightly, resulting in a lower stress state, which would have allowed further fuel consumption and mass minimization if accounted for in the MDO process. However, it showed that evaluating the stress distribution with the linear model is more conservative and a good approximation for fast result acquisition.

Furthermore, estimating the flutter boundary showed an influence of the linear and non-linear deformed shapes. While for three out of the four evaluated cases the flutter boundary was less conservative, the boundary was still far from the flight envelope for all the designs.

In conclusion, the non-linear assessment required significantly higher computational time, which for a preliminary design study might not be beneficial, as the performance influence of the outcome is not deemed high enough to justify the cost. Still, based on

the obtained results, it can be of interest to consider non-linearities for more complex novel configurations, such as the SBW or other joined wing designs.

Chapter 7

Concluding Remarks and Future Work

In the following sections the thesis is concluded. Starting with a summary of the work in section 7.1, the novel aspects of the study are emphasized in section 1.6, including potentials and limitations. The conclusion closes with final remarks regarding the dissertation and possible future research to continue the studies in section 7.2.

7.1 Summary of Works

To meet the environmental goals of aviation for the future, novel aircraft are suggested for a leap in efficiency. Some promising concepts base their increase in efficiency on an increase in wing aspect ratio, to reduce the induced drag and therefore enhancing aerodynamic efficiency. This includes high aspect ratio wing aircraft and strut braced wing designs. The former, while rather conventional regarding the tube-wing layout, has slenderer wings than currently operating designs. The latter supports elongated wings with a strut structure to alleviate wing loading. However, with the longer and slenderer wings, influence of flexibility grows, effecting performance over the whole flight envelope and driving the design.

To assess the aeroelastic behaviour as mutual interaction between aerodynamics and structure, fluid-structure interaction in a multi-disciplinary design analysis and optimization environment is employed. A MDO methodology was developed for analyzing the mentioned novel aircraft configurations.

After introducing the utilized tools, the methodology is described in detail, with its

capability to employ low- and high-fidelity assessments. It includes a 3D panel method and RANS based CFD for evaluating aerodynamics. The structure is assessed via an equivalent beam model, where additional mass points can be linked to nodes. A flutter assessment is done with NASTRAN, where the aerodynamic influence coefficient matrix is obtained with a doublet lattice method.

In a multi-objective optimization, considering an operational and manufacturing cost metric, the designs are analyzed and improved towards the objective.

Due to the expensive assessments of objective and constraint function values, it is important to reduce the number of evaluations. As no adjoint solutions were accessible to efficiently obtain gradient information, a surrogate model based optimization is employed. With an efficient global optimization approach, new infill points for the models were searched in the optimization process and the models were updated iteratively.

The obtained designs could achieve an aerodynamic benefit, increasing their lift over drag ratio. However, this came with an increase in structural weight, which can be related to an increase in manufacturing cost. The rationality of this compromise depends on the weighting between operational and manufacturing cost in the objective. In the herein presented optimization, operational costs were favoured.

While both designs could increase the efficiency considerably, the optimization was able to improve the SBW design further compared to the HARW. Despite the added weight and the additional drag due to the strut, the increase in aspect ratio led to less induced drag and the inner wing part weight could be reduced compared to a cantilevered wing. The overall benefit for the HARW concluded with around 7% and the SBW design could achieve a 9% improvement in objective function. While other studies of novel concepts achieved comparable results, they were usually higher. Considering the influence of flexibility the optimization faces additional challenges, as aeroelastic effects affect the whole flight envelope.

The used method in the surrogate based optimization utilizes the prediction of constraint functions without considering any uncertainty present in the surrogate models. Therefore, to further improve the efficiency of constrained surrogate based optimization, this work additionally proposed new possibilities to account for the uncertainty.

In particular, two methods that use the probability of feasibility were developed and investigated for constrained surrogate-based optimization. The inclusion of uncertainty in surrogate models representing constraint functions improves the optimization process

by reducing the computational time to evaluate expensive functions. Mathematical test functions, ranging from low to high dimension, were utilized to scrutinize the methodology employing simple and complex nonlinear constraints. The procedure was compared with an established approach, and conclusions have been drawn regarding robustness and efficiency. It could be shown that the proposed method performed similarly well and could even outperform the established approach for the test cases.

An aerodynamic shape optimization of a 2D transonic airfoil demonstrated the practical application of the proposed methods. Here, the results were less conclusive and a concluding statement regarding performance benefit and efficiency could not be asserted. A convergence could not be reached for any of the methods within the given computational time. However, all approaches improved the baseline design significantly.

Employing the probability of feasibility in a Gaussian process optimization approach can accelerate the convergence for specific cases with robustness. Further investigations of the hyperparameter may possibly improve these methodologies to balance exploration and exploitation towards a faster result generation. Since the method is not matured yet, as could be seen in the engineering application, the MDO of the flexible wing aircraft was performed with a conventional approach.

7.2 Final Remarks and Future Work

The investigation and improvement of novel aircraft concepts is an ongoing topic. With an increase in computational power, significant aspects influencing the design, such as aeroelasticity and multi-disciplinary interaction, can be assessed. With increasing complexity to meet environmental goals and regulations, the necessity for the development and use multi-disciplinary tools and methodologies is an increasing topic.

Besides the investigated concepts of this work, aircraft with a high aspect ratio or strut-braced wing, can also offer efficiency benefits. Unconventional concepts, such as blended wing bodies or flying wings, are designs of interest for the future of aviation, that incorporate a multitude of disciplines and require advanced assessment tools. This aspects blends with the presented methodology, which can be further extended to integrate more disciplines and levels of fidelity in the process.

The surrogate characteristic of the employed methodology could to some extend provide some acceleration of the process. Still, possible improvements are seen to

further enhance capabilities. This includes the use of multi-fidelity surrogate models, where not only for each fidelity surrogates are built, but the information of different fidelity levels is fused to accelerate the process. Moreover, the increasing implemented capabilities for high-fidelity assessment tools of using adjoint methods can be employed and exploited to be utilized in the surrogate generation, using sensitivity information to built more accurate models with few known designs. Approaches in surrogate modelling to reduce the computational burden, such as mixture of experts and partial least square methods, can support increasing numbers of design variables, and therefore design freedom, to obtain improved designs and design space knowledge within shorter time. Another considerably beneficial aspect is the increasing computational power of personal computers, allowing for more costly computations available a small scaled working machines. This promotes the vaster exploration and exploitation of designs, enabling again more insights and improvements with more accurate computational tools.

Lastly, the proposed methodology to efficiently obtain designs of interest in a given design space could show its capability. However, further possible improvements are sought of, including the use of adaptive parameters in its formulation, the employment in multi-fidelity approaches, but also further investigation about its potential for engineering applications.

Bibliography

[1] ES van der Sman, B Peerlings, J Kos, R Lieshout, and T Boonekamp. Destination 2050: A roadmap to net zero European aviation. `https://www.destination2050.eu/wp-content/uploads/2021/02/Destination2050_Report.pdf`, 2020. Accessed: 2021-09-02.

[2] Axel Krein and Gareth Williams. Flightpath 2050: Europe's vision for aeronautics. *Innovation for Sustainable Aviation in a Global Environment: Proceedings of the Sixth European Aeronautics Days, Madrid*, 30, 2012. doi:10.2777/50266.

[3] International Air Transport Association. IATA Vision 2050. `https://www.iata.org/contentassets/bccae1c5a24e43759607a5fd8f44770b/vision-2050.pdf`, 2011. Accessed: 2021-09-02.

[4] David K Hall, Arthur C Huang, Alejandra Uranga, Edward M Greitzer, Mark Drela, and Sho Sato. Boundary Layer Ingestion Propulsion Benefit for Transport Aircraft. *Journal of Propulsion and Power*, 33(5):1118–1129, 2017. doi:10.2514/1.B36321.

[5] Tomasz P Stankowski, David G MacManus, Matthew Robinson, and Christopher T Sheaf. Aerodynamic Effects of Propulsion Integration for High Bypass Ratio Engines. *Journal of Aircraft*, 54(6):2270–2284, 2017. doi:10.2514/1.C034150.

[6] Alejandra Uranga, Mark Drela, David K Hall, and Edward M Greitzer. Analysis of the Aerodynamic Benefit from Boundary Layer Ingestion for Transport Aircraft. *AIAA journal*, 56(11):4271–4281, 2018. doi:10.2514/1.J056781.

[7] Reynard de Vries, Nando van Arnhem, Tomas Sinnige, Roelof Vos, and Leo LM Veldhuis. Aerodynamic interaction between propellers of a distributed-propulsion system in forward flight. *Aerospace Science and Technology*, 118:107009, 2021. doi:10.1016/j.ast.2021.107009.

[8] Xiaolong Zhang, Cheryl L Bowman, Tim C O'Connell, and Kiruba S Haran. Large electric machines for aircraft electric propulsion. *IET Electric Power Applications*, 12(6):767–779, 2018. doi:10.1049/iet-epa.2017.0639.

[9] Amir S Gohardani, Georgios Doulgeris, and Riti Singh. Challenges of future aircraft propulsion: A review of distributed propulsion technology and its potential application for the all electric commercial aircraft. *Progress in Aerospace Sciences*, 47(5):369–391, 2011. doi:10.1016/j.paerosci.2010.09.001.

[10] Andrew T Wick, John R Hooker, and Cale H Zeune. Integrated Aerodynamic Benefits of Distributed Propulsion. In *53rd AIAA Aerospace Sciences Meeting*, page 1500, 2015. doi:10.2514/6.2015-1500.

[11] Dan Lev, Roger M Myers, Kristina M Lemmer, Jonathan Kolbeck, Hiroyuki Koizumi, and Kurt Polzin. The technological and commercial expansion of electric propulsion. *Acta Astronautica*, 159:213–227, 2019. doi:10.1016/j.actaastro.2019.03.058.

[12] Karthik Gopalakrishnan and Hamsa Balakrishnan. Control and Optimization of Air Traffic Networks. *Annual Review of Control, Robotics, and Autonomous Systems*, 4:397–424, 2021. doi:10.1146/annurev-control-070720-080844.

[13] Peter Schmollgruber, Nathalie Bartoli, Judicael Bedouet, Emmanuel Benard, and Yves Gourinat. Improvement of the Aircraft Design process for Air Traffic Management evaluations. In *2018 AIAA Aerospace Sciences Meeting*, page 0283, 2018. doi:10.2514/6.2018-0283.

[14] Rhea P. Liem, Charles A. Mader, and Joaquim R. R. A. Martins. Surrogate models and mixtures of experts in aerodynamic performance prediction for aircraft mission analysis. *Aerospace Science and Technology*, 43:126–151, 2015. doi:10.1016/j.ast.2015.02.019.

[15] Alessandro Gardi, Roberto Sabatini, and Subramanian Ramasamy. Multi-objective optimisation of aircraft flight trajectories in the ATM and avionics context. *Progress in Aerospace Sciences*, 83:1–36, 2016. doi:10.1016/j.paerosci.2015.11.006.

[16] Xiongwen Qian, Jianfeng Mao, Chun-Hsien Chen, Songlin Chen, and Changpeng Yang. Coordinated multi-aircraft 4D trajectories planning considering

buffer safety distance and fuel consumption optimization via pure-strategy game. *Transportation Research Part C: Emerging Technologies*, 81:18–35, 2017. doi:10.1016/j.trc.2017.05.008.

[17] Michael Schmidt, Annika Paul, Mara Cole, and Kay Olaf Ploetner. Challenges for ground operations arising from aircraft concepts using alternative energy. *Journal of Air Transport Management*, 56:107 – 117, 2016. doi:10.1016/j.jairtraman.2016.04.023. Growing airline networks -Selected papers from the 18th ATRS World Conference, Bordeaux, France, 2014.

[18] Michael Schmidt. A review of aircraft turnaround operations and simulations. *Progress in Aerospace Sciences*, 92:25–38, 2017. doi:10.1016/j.paerosci.2017.05.002.

[19] Andrew J. Timmis, Alma Hodzic, Lenny Koh, Michael Bonner, Constantinos Soutis, Andreas W. Schäfer, and Lynnette Dray. Environmental impact assessment of aviation emission reduction through the implementation of composite materials. *The International Journal of Life Cycle Assessment*, 20(2):233–243, 2015. ISSN 0948-3349, 1614-7502. doi:10.1007/s11367-014-0824-0.

[20] Xuesong Zhang, Yongjun Chen, and Junling Hu. Recent advances in the development of aerospace materials. *Progress in Aerospace Sciences*, 97:22–34, 2018. doi:10.1016/j.paerosci.2018.01.001.

[21] Carlo E.D. Riboldi, Lorenzo Trainelli, and Fabio Biondani. Structural Batteries in Aviation: A Preliminary Sizing Methodology. *Journal of Aerospace Engineering*, 33(4):04020031, 2020. doi:10.1061/(ASCE)AS.1943-5525.0001144.

[22] A. Abbas, J. de Vicente, and E. Valero. Aerodynamic technologies to improve aircraft performance. *Aerospace Science and Technology*, 28(1):100 – 132, 2013. doi:10.1016/j.ast.2012.10.008.

[23] Joaquim RRA Martins. Perspectives on aerodynamic design optimization. In *AIAA Scitech 2020 Forum*, Orlando, Florida, USA, January 2020. doi:10.2514/6.2020-0043.

[24] Justin S. Gray and Joaquim R. R. A. Martins. Coupled aeropropulsive design optimisation of a boundary-layer ingestion propulsor. *The Aeronautical Journal*, 123(1259):121–137, 2019. doi:10.1017/aer.2018.120.

[25] Silvestro Barbarino, Onur Bilgen, Rafic M Ajaj, Michael I Friswell, and Daniel J Inman. A Review of Morphing Aircraft. *Journal of intelligent material systems and structures*, 22(9):823–877, 2011. doi:10.1177/1045389X11414084.

[26] David A Burdette and Joaquim RRA Martins. Design of a transonic wing with an adaptive morphing trailing edge via aerostructural optimization. *Aerospace Science and Technology*, 81:192–203, 2018. doi:10.1016/j.ast.2018.08.004.

[27] K.S.G. Krishnan, O. Bertram, and O. Seibel. Review of hybrid laminar flow control systems. *Progress in Aerospace Sciences*, 93:24 – 52, 2017. doi:10.1016/j.paerosci.2017.05.005.

[28] Carlos Cesnik and Weihua Su. Nonlinear Aeroelastic Modeling and Analysis of Fully flexible Aircraft. In *46th AIAA/ASME/ASCE/AHS/ASC Structures, Structural Dynamics and Materials Conference*, page 2169, 2005. doi:10.2514/6.2005-2169.

[29] Carlos ES Cesnik, Rafael Palacios, and Eric Y Reichenbach. Reexamined Structural Design Procedures for Very Flexible Aircraft. *Journal of Aircraft*, 51 (5):1580–1591, 2014. doi:10.2514/1.C032464.

[30] Joaquim R. R. A. Martins and Andrew B. Lambe. Multidisciplinary design optimization: A survey of architectures. *AIAA Journal*, 51(9):2049–2075, 2013. doi:10.2514/1.J051895.

[31] John David Anderson Jr. *Fundamentals of Aerodynamics*. Tata McGraw-Hill Education, 6th edition, 2017.

[32] Mayuresh J Patil, Dewey H Hodges, and Carlos ES Cesnik. Nonlinear Aeroelasticity and Flight Dynamics of High-Altitude Long-Endurance Aircraft. *Journal of Aircraft*, 38(1):88–94, 2001. doi:10.2514/2.2738.

[33] Christopher M Shearer and Carlos ES Cesnik. Nonlinear Flight Dynamics of Very Flexible Aircraft. *Journal of Aircraft*, 44(5):1528–1545, 2007. doi:10.2514/1.27606.

[34] Frederico Afonso, José Vale, Éder Oliveira, Fernando Lau, and Afzal Suleman. A review on non-linear aeroelasticity of high aspect-ratio wings. *Progress in Aerospace Sciences*, 89:40 – 57, 2017. doi:10.1016/j.paerosci.2016.12.004.

[35] Alasdair C Gray and Joaquim RRA Martins. Geometrically Nonlinear High-fidelity Aerostructural Optimization for Highly Flexible Wings. In *AIAA Scitech 2021 Forum*, page 0283, 2021. doi:10.2514/6.2021-0283.

[36] Zhoujie Lyu, Gaetan K Kenway, and Joaquim RRA Martins. RANS-based aerodynamic shape optimization investigations of the common research model wing. In *52nd Aerospace Sciences Meeting*, page 0567, 2014. doi:10.2514/6.2014-0567.

[37] Gaetan KW Kenway and Joaquim RRA Martins. Multipoint High-Fidelity Aerostructural Optimization of a Transport Aircraft Configuration. *Journal of Aircraft*, 51(1):144–160, 2014. doi:10.2514/1.C032150.

[38] Bret Stanford and Philip Beran. Direct flutter and limit cycle computations of highly flexible wings for efficient analysis and optimization. *Journal of Fluids and Structures*, 36:111–123, 2013. doi:10.1016/j.jfluidstructs.2012.08.008.

[39] Yinan Wang, Andrew Wynn, and Rafael Palacios. Nonlinear Modal Aeroservoelastic Analysis Framework for Flexible Aircraft. *AIAA Journal*, 54(10): 3075–3090, 2016. doi:10.2514/1.J054537.

[40] Cristina Riso, Fausto G Di Vincenzo, Markus Ritter, Carlos ES Cesnik, and Franco Mastroddi. Nonlinear Aeroelastic Trim of Very Flexible Aircraft Described by Detailed Models. *Journal of Aircraft*, 55(6):2338–2346, 2018. doi:10.2514/1.C034787.

[41] Chuanqiang Gao and Weiwei Zhang. Transonic aeroelasticity: A new perspective from the fluid mode. *Progress in Aerospace Sciences*, 113:100596, 2020. doi:10.1016/j.paerosci.2019.100596.

[42] Eirikur Jonsson, Cristina Riso, Christopher A. Lupp, Carlos E.S. Cesnik, Joaquim R.R.A. Martins, and Bogdan I. Epureanu. Flutter and post-flutter constraints in aircraft design optimization. *Progress in Aerospace Sciences*, 109: 100537, 2019. doi:10.1016/j.paerosci.2019.04.001.

[43] Andrea Castrichini, Vijaya Hodigere Siddaramaiah, DE Calderon, Jonathan E Cooper, Thomas Wilson, and Yves Lemmens. Nonlinear Folding Wing Tips for Gust Loads Alleviation. *Journal of Aircraft*, 53(5):1391–1399, 2016. doi:10.2514/1.C033887.

[44] Ronald CM Cheung, Djamel Rezgui, Jonathan E Cooper, and Thomas Wilson. Testing of a Hinged Wingtip Device for Gust Loads Alleviation. *Journal of Aircraft*, 55(5):2050–2067, 2018. doi:10.2514/1.C034811.

[45] Ronald CM Cheung, Djamel Rezgui, Jonathan E Cooper, and Thomas Wilson. Testing of Folding Wingtip for Gust Load Alleviation of Flexible High-Aspect-Ratio Wing. *Journal of Aircraft*, 57(5):876–888, 2020. doi:10.2514/1.C035732.

[46] Rauno Cavallaro and Luciano Demasi. Challenges, ideas, and innovations of joined-wing configurations: A concept from the past, an opportunity for the future. *Progress in Aerospace Sciences*, 87:1 – 93, 2016. doi:10.1016/j.paerosci.2016.07.002.

[47] W. Pfenninger. Design Considerations of Large Subsonic Long Range Transport Airplanes with Low Drag Boundary Layer Suction. Technical Report NAI-54-800 (BLC-67), Northrop Aircraft, Inc., 1954.

[48] W. Pfenninger. Long-range lfc transport. Technical Report 90-12508, NASA, 1987.

[49] John F Gundlach IV, Philippe-Andre Tetrault, Frank H Gern, Amir H Nagshineh-Pour, Andy Ko, Joseph A Schetz, William H Mason, Rakesh K Kapania, William H Mason, Bernard Grossman, and P.-A. Tétrault. Conceptual Design Studies of a Strut-Braced Wing Transonic Transport. *Journal of aircraft*, 37(6): 976–983, 2000. doi:10.2514/2.2724.

[50] Frank H Gern, Andy Ko, Erwin Sulaeman, John F Gundlach, Rakesh K Kapania, and Raphael T Haftka. Multidisciplinary Design Optimization of a Transonic Commercial Transport with Strut-Braced Wing. *Journal of aircraft*, 38(6): 1006–1014, 2001. doi:10.2514/2.2887.

[51] Marty K Bradley and Christopher K Droney. *Subsonic Ultra Green Aircraft Research: Phase I Final Report*. National Aeronautics and Space Administration, Langley Research Center, 2011.

[52] Marty K Bradley, Timothy J Allen, and Christopher Droney. Subsonic Ultra Green Aircraft Research: Phase II-Volume III; Truss Braced Wing Aeroelastic Test Report. Technical report, Tech. rep., NASA, CR-2015-218704, 2014.

[53] Marty K Bradley, Christopher K Droney, and Timothy J Allen. *Subsonic Ultra Green Aircraft Research. Phase II-Volume I; Truss Braced Wing Design Exploration*. National Aeronautics and Space Administration, Langley Research Center, 2015.

[54] Ohad Gur, Manav Bhatia, Joseph A Schetz, William H Mason, Rakesh K Kapania, and Dimitri N Mavris. Design Optimization of a Truss-Braced-Wing Transonic Transport Aircraft. *Journal of aircraft*, 47(6):1907–1917, 2010. doi:10.2514/1.47546.

[55] Ohad Gur, Manav Bhatia, William H Mason, Joseph A Schetz, Rakesh K Kapania, and Taewoo Nam. Development of a framework for truss-braced wing conceptual MDO. *Structural and Multidisciplinary optimization*, 44(2):277–298, 2011. doi:10.1007/s00158-010-0612-9.

[56] Timothy Chau and David W Zingg. Aerodynamic Design Optimization of a Transonic Strut-Braced-Wing Regional Aircraft. *Journal of Aircraft*, pages 1–19, 2021. doi:10.2514/1.C036389.

[57] Ney R. Secco and Joaquim R. R. A. Martins. RANS-Based Aerodynamic Shape Optimization of a Strut-Braced Wing with Overset Meshes. *Journal of Aircraft*, 56(1):217–227, 2019. doi:10.2514/1.C034934.

[58] Juntao Xiong, Jason Fugate, and Nhan T. Nguyen. Investigation of Truss-Braced Wing Aircraft Transonic Wing-Strut Interference Effects Using FUN3D. In *AIAA Aviation 2019 Forum*, Dallas, Texas, USA, June 2019. American Institute of Aeronautics and Astronautics. doi:10.2514/6.2019-3026.

[59] Jason Fugate, Nhan T. Nguyen, and Juntao Xiong. Aero-Structural Modeling of the Truss-Braced Wing Aircraft Using Potential Method with Correction Methods for Transonic Viscous Flow and Wing-Strut Interference Aerodynamics. In *AIAA Aviation 2019 Forum*, Dallas, Texas, USA, June 2019. American Institute of Aeronautics and Astronautics. doi:10.2514/6.2019-3028.

[60] Nhan T. Nguyen, Jason Fugate, Upender K. Kaul, and Juntao Xiong. Flutter Analysis of the Transonic Truss-Braced Wing Aircraft Using Transonic Correction. In *AIAA Scitech 2019 Forum*, San Diego, California, USA, January 2019. American Institute of Aeronautics and Astronautics. doi:10.2514/6.2019-0217.

[61] Robert E. Bartels, Christie J. Funk, and Robert C. Scott. Limit-Cycle Oscillation of the Subsonic Ultra-Green Aircraft Research Truss-Braced Wing Aeroelastic Model. *Journal of Aircraft*, 54(5):1605–1613, 2017. doi:10.2514/1.C034064.

[62] Eric Ting, Daniel Chaparro, and Nhan T. Nguyen. Development of an Integrated Nonlinear Aeroservoelastic Flight Dynamic Model of the Truss-Braced Wing Aircraft. In *58th AIAA/ASCE/AHS/ASC Structures, Structural Dynamics, and Materials Conference*, Grapevine, Texas, USA, January 2017. American Institute of Aeronautics and Astronautics. doi:10.2514/6.2017-1815.

[63] C. P. Szczyglowski, C. Howcroft, S. A. Neild, B. Titurus, J. Z. Jiang, J. E. Cooper, and E. Coetzee. Strut-Braced Wing Modelling with a Reduced Order Beam Model. In *5th Aircraft Structural Design Conference*. Royal Aeronautical Society, 2016.

[64] J. H. McMasters and I. M. Kroo. Advanced confgurations for very large transport airplanes. *Aircraft Design*, 1(4):217–242, 1998. doi:10.1016/S1369-8869(98)00018-4.

[65] I. Kroo. Nonplanar wing concepts for increased aircraft efficiency. In *Innovative Configurations and Advanced Concepts for Future Civil Aircraft, VKI Lecture Series*, Rhode-Saint-Genèse, Belgium, June 2005. von Karman Institute for Fluid Dynamics.

[66] JE Cooper, Imene Chekkal, RCM Cheung, Christopher Wales, NJ Allen, S Lawson, AJ Peace, R Cook, P Standen, SD Hancock, et al. Design of a Morphing Wingtip. *Journal of Aircraft*, 52(5):1394–1403, 2015. doi:10.2514/1.C032861.

[67] Rauno Cavallaro, Rocco Bombardieri, Luciano Demasi, and Andrea Iannelli. Prandtlplane Joined Wing: Body freedom flutter, limit cycle oscillation and freeplay studies. *Journal of Fluids and Structures*, 59:57–84, 2015. doi:10.1016/j.jfluidstructs.2015.08.016.

[68] Robert H Liebeck. Design of the Blended Wing Body Subsonic Transport. *Journal of aircraft*, 41(1):10–25, 2004. doi:10.2514/1.9084.

[69] Melissa Carter, Dan Vicroy, and Dharmendra Patel. Blended-Wing-Body Transonic Aerodynamics: Summary of Ground Tests and Sample Results. In *47th*

AIAA aerospace sciences meeting including the new horizons forum and aerospace exposition, page 935, 2009. doi:10.2514/6.2009-935.

[70] A Velicki and P Thrash. Blended wing body structural concept development. *The Aeronautical Journal*, 114(1158):513–519, 2010.

[71] Pritesh Mody, Sho Sato, David Hall, Elena De la Rosa Blanco, James Hileman, and Ed Wen. Conceptual Design of an N+3 Hybrid Wing Body Subsonic Transport. In *28th AIAA Applied Aerodynamics Conference*, Chicago, Illinois, USA, 2010. American Institute of Aeronautics and Astronautics. doi:10.2514/6.2010-4812.

[72] Craig Nickol. Hybrid Wing Body Configuration Scaling Study. In *50th AIAA Aerospace Sciences Meeting including the New Horizons Forum and Aerospace Exposition*, Nashville, Tennessee, USA, 2012. American Institute of Aeronautics and Astronautics. doi:10.2514/6.2012-337.

[73] Frank H. Gern. Conceptual design and structural analysis of an open rotor hybrid wing body aircraft. In *54th AIAA/ASME/ASCE/AHS/ASC Structures, Structural Dynamics, and Materials Conference*, Boston, Massachusetts, USA, April 2013. American Institute of Aeronautics and Astronautics. doi:10.2514/6.2013-1688.

[74] John R. Hooker. Design of a hybrid wing body for fuel efficient air mobility operations at transonic flight conditions. In *52nd Aerospace Sciences Meeting*, National Harbor, Maryland, USA, 2014. American Institute of Aeronautics and Astronautics. doi:10.2514/6.2014-1285.

[75] Ryan W. Plumley and Cale Zeune. Revolutionary configurations: Technology convergence point. In *55th AIAA Aerospace Sciences Meeting*, Grapevine, Texas, USA, January 2017. doi:10.2514/6.2017-0097.

[76] Gregory Gatlin, Dan Vicroy, and Melissa Carter. Experimental Investigation of the Low-Speed Aerodynamic Characteristics of a 5.8-Percent Scale Hybrid Wing Body Configuration. In *30th AIAA Applied Aerodynamics Conference*. American Institute of Aeronautics and Astronautics, 2012. doi:10.2514/6.2012-2669.

[77] J. E. Action and V. Johnson. Structural layout of a hybrid wing body transport. In *55th AIAA Aerospace Sciences Meeting*, Grapevine, Texas, USA, January 2017. doi:10.2514/6.2017-0101.

[78] Barrett D. Flansburg. Structural loads analysis of a hybrid wing body transport. In *58th AIAA/ASCE/AHS/ASC Structures, Structural Dynamics, and Materials Conference*, Grapevine, Texas, USA, January 2017. doi:10.2514/6.2017-0205.

[79] Wensheng Zhu, Zhouwei Fan, and Xiongqing Yu. Structural mass prediction in conceptual design of blended-wing-body aircraft. *Chinese Journal of Aeronautics*, 32(11):2455–2465, 2019. doi:10.1016/j.cja.2019.08.003.

[80] Jeff D. Flamm, Kevin James, and John T. Bonet. Overview of era integrated technology demonstration (itd) 51a ultra-high bypass (uhb) integration for hybrid wing body (hwb) (invited). In *54th AIAA Aerospace Sciences Meeting*, San Diego, California, USA, January 2016. doi:10.2514/6.2016-0007.

[81] Andrew T Wick, John R Hooker, Casie M Clark, Ryan Plumley, and Cale Zeune. Powered low speed testing of the hybrid wing body. In *55th AIAA Aerospace Sciences Meeting*, Grapevine, Texas, USA, January 2017. doi:10.2514/6.2017-0100.

[82] Andrew T. Wick, John R. Hooker, Jimmy Walker, David T. Chan, Ryan Plumley, and Cale Zeune. Hybrid wing body performance validation at the national transonic facility. In *55th AIAA Aerospace Sciences Meeting*, Grapevine, Texas, USA, January 2017. doi:10.2514/6.2017-0099.

[83] M. A. Page, E. J. Smetak, and S. L. Yang. Single-aisle airliner disruption with a single-deck blended wing-body. In *31st Congress of the International Council of the Aeronautical Sciences*, Belo Horizonte, Brazil, 2018.

[84] Yaolong Liu, Ali Elham, Peter Horst, and Martin Hepperle. Exploring vehicle level benefits of revolutionary technology progress via aircraft design and optimization. *Energies*, 11(1):166, 2018. doi:10.3390/en11010166.

[85] Paul Okonkwo and Howard Smith. Review of evolving trends in blended wing body aircraft design. *Progress in Aerospace Sciences*, 82:1 – 23, 2016. doi:10.1016/j.paerosci.2015.12.002.

[86] Zhenli Chen, Minghui Zhang, Yingchun Chen, Weimin Sang, Zhaoguang Tan, Dong Li, and Binqian Zhang. Assessment on critical technologies for conceptual design of blended-wing-body civil aircraft. *Chinese Journal of Aeronautics*, 32 (8):1797 – 1827, 2019. doi:10.1016/j.cja.2019.06.006.

[87] Mark Drela. Development of the d8 transport configuration. In *29th AIAA Applied Aerodynamics Conference*, Honolulu, Hawaii, USA, June 2011. doi:10.2514/6.2011-3970.

[88] Francesco Faggiano, Roelof Vos, Max Baan, and Reinier Van Dijk. Aerodynamic design of a flying v aircraft. In *17th AIAA Aviation Technology, Integration, and Operations Conference*, Denver, Colorado, USA, June 2017. doi:10.2514/6.2017-3589.

[89] E. M. Greitzer, P. A. Bonnefoy, D. K. Hall, R. J. Hansman, J. I. Hileman, R. H. Liebeck, J. Lovegren, P. Mody, J. A. Pertuze, S. Sato, Z. S. Spakovszky, C. S. Tan, J. S. Hollman, J. E. Duda, N. Fitzgerald, J. Houghton, J. L. Kerrebrock, G. F. Kiwada, D. Kordonowy, J. C. Parrish, J. Tylko, and E. A. Wen. N+3 aircraft concept designs and trade studies, final report. Technical Report CR—2010-216794, NASA, Hampton, VA, USA, 2010.

[90] Brian M. Yutko, Neil Titchener, Christopher Courtin, Michael Lieu, Larry Wirsing, John Tylko, Jeffrey T. Chambers, Thomas W. Roberts, and Clinton S. Church. Conceptual design of a d8 commercial aircraft. In *17th AIAA Aviation Technology, Integration, and Operations Conference*, Denver, Colorado, USA, June 2017. doi:10.2514/6.2017-3590.

[91] Jeffrey T. Chambers, Neil Titchener, Larry M. Wirsing, Deborah R. Hoffman, and Adam J. Treager. Propulsion-airframe structural integration for a subscale d8 demonstration vehicle. In *AIAA Scitech 2019 Forum*, San Diego, California, USA, January 2019. doi:10.2514/6.2019-2101.

[92] Ian Clark, Russell H. Thomas, and Yueping Guo. Aircraft system noise assessment of the nasa d8 subsonic transport concept. In *2018 AIAA/CEAS Aeroacoustics Conference*, Atlanta, Georgia, USA, June 2018. doi:10.2514/6.2018-3124.

[93] M. M. Opgenoord, M. Drela, and K. E. Willcox. Influence of transonic flutter on the conceptual design of next-generation transport aircraft. *AIAA Journal*, 57:1973–1987, 2018. doi:10.2514/6.2018-0948.

[94] Marco Palermo and Roelof Vos. Experimental aerodynamic analysis of a 4.6%-scale flying-v subsonic transport. In *AIAA Scitech 2020 Forum*, Orlando, Florida, USA, January 2020. American Institute of Aeronautics and Astronautics. doi:10.2514/6.2020-2228.

[95] Berta Rubio Pascual and Roelof Vos. The Effect of Engine Location on the Aerodynamic Efficiency of a Flying-V Aircraft. In *AIAA Scitech 2020 Forum*, Orlando, Florida, USA, January 2020. American Institute of Aeronautics and Astronautics. doi:10.2514/6.2020-1954.

[96] Alberto Ruiz Garcia, Roelof Vos, and de Coen Visser. Aerodynamic Model Identification of the Flying V from Wind Tunnel Data. In *AIAA Scitech 2020 Forum*, Orlando, Florida, USA, January 2020. American Institute of Aeronautics and Astronautics. doi:10.2514/6.2020-2739.

[97] Raymond L Bisplinghoff, Holt Ashley, and Robert L Halfman. *Aeroelasticity*. Addison-Wesley, Cambridge, 1955.

[98] Dewey H Hodges and G Alvin Pierce. *Introduction to Structural Dynamics and Aeroelasticity*, volume 15. cambridge university press, 2 edition, 2011. doi:10.1017/CBO9780511997112.

[99] Earl H Dowell, Howard C Curtiss, Robert H Scanlan, and Fernando Sisto. *A Modern Course in Aeroelasticity*, volume 120. Springer, 5 edition, 2015. doi:10.1007/978-3-319-09453-3.

[100] Jan Robert Wright and Jonathan Edward Cooper. *Introduction to Aircraft Aeroelasticity and Loads*, volume 20. John Wiley & Sons, 2 edition, 2008. doi:10.1002/9781118700440.

[101] Grigorios Dimitriadis. *Introduction to Nonlinear Aeroelasticity*. John Wiley & Sons, 2017. doi:10.1002/9781118756478.

[102] BHK Lee. Self-sustained shock oscillations on airfoils at transonic speeds. *Progress in Aerospace Sciences*, 37(2):147–196, 2001. doi:10.1016/j.jfluidstructs.2010.10.001.

[103] JD Crouch, A Garbaruk, D Magidov, and A Travin. Origin of transonic buffet on aerofoils. *Journal of fluid mechanics*, 628:357–369, 2009. doi:10.1017/S0022112009006673.

[104] Fulvio Sartor, Clément Mettot, and Denis Sipp. Stability, Receptivity, and Sensitivity Analyses of Buffeting Transonic Flow over a Profile. *AIAA Journal*, 53(7):1980–1993, 2015. doi:10.2514/1.J053588.

[105] Weiwei Zhang, Bobin Wang, Zhengyin Ye, and Jingge Quan. Efficient Method for Limit Cycle Flutter Analysis Based on Nonlinear Aerodynamic Reduced-Order Models. *AIAA journal*, 50(5):1019–1028, 2012. doi:10.2514/1.J050581.

[106] Xavier Amandolese, Sébastien Michelin, and M Choquel. Low speed flutter and limit cycle oscillations of a two-degree-of-freedom flat plate in a wind tunnel. *Journal of Fluids and Structures*, 43:244–255, 2013. doi:10.1016/j.jfluidstructs.2013.09.002.

[107] Daniel Green and William G Unruh. The failure of the Tacoma Bridge: A physical model. *American journal of physics*, 74(8):706–716, 2006. doi:10.1119/1.2201854.

[108] Thomas E Noll, John M Brown, Marla E Perez-Davis, Stephen D Ishmael, Geary C Tiffany, and Matthew Gaier. Investigation of the Helios Prototype Aircraft Mishap Volume I Mishap Report. *Downloaded on*, 9:2004, 2004.

[109] Eli Livne. Aircraft Active Flutter Suppression: State of the Art and Technology Maturation Needs. *Journal of Aircraft*, 55(1):410–452, 2018. doi:10.2514/1.C034442.

[110] Alexandre N Marques, Max MJ Opgenoord, Remi R Lam, Anirban Chaudhuri, and Karen E Willcox. Multifidelity Method for Locating Aeroelastic Flutter Boundaries. *AIAA Journal*, 58(4):1772–1784, 2020. doi:10.2514/1.J058663.

[111] Mayuresh J Patil and Dewey H Hodges. On the importance of aerodynamic and structural geometrical nonlinearities in aeroelastic behavior of high-aspect-ratio wings. *Journal of Fluids and Structures*, 19(7):905–915, 2004. doi:10.1016/j.jfluidstructs.2004.04.012.

[112] MJ de C Henshaw, Ken J Badcock, GA Vio, CB Allen, J Chamberlain, I Kaynes, Grigorios Dimitriadis, JE Cooper, MA Woodgate, Abdul M Rampurawala, et al. Non-linear aeroelastic prediction for aircraft applications. *Progress in Aerospace Sciences*, 43(4-6):65–137, 2007. doi:10.1016/j.paerosci.2007.05.002.

[113] Earl Dowell, John Edwards, and Thomas Strganac. Nonlinear Aeroelasticity. *Journal of Aircraft*, 40(5):857–874, 2003. doi:10.2514/2.6876.

[114] Earl H Dowell and Kenneth C Hall. Modeling of Fluid-Structure Interaction. *Annual review of fluid mechanics*, 33(1):445–490, 2001. doi:10.1146/annurev.fluid.33.1.445.

[115] Freddie D Witherden and Antony Jameson. Aerodynamics. *Encyclopedia of Computational Mechanics Second Edition*, pages 1–107, 2018. doi:10.1002/9781119176817.ecm2062.

[116] Warren F Phillips and DO Snyder. Modern Adaptation of Prandtl's Classic Lifting-Line Theory. *Journal of Aircraft*, 37(4):662–670, 2000. doi:10.2514/2.2649.

[117] Joseph Katz and Allen Plotkin. *Low-Speed Aerodynamics*. Cambridge Aerospace Series. Cambridge University Press, 2 edition, 2001. doi:10.1017/CBO9780511810329.

[118] John David Anderson and J Wendt. *Computational Fluid Dynamics*, volume 206. Springer, 3 edition, 1995. doi:10.1007/978-3-540-85056-4.

[119] A Suleman, F Afonso, J Vale, É Oliveira, and F Lau. Non-linear aeroelastic analysis in the time domain of high-aspect-ratio wings: Effect of chord and taper-ratio variation. *The Aeronautical Journal*, 121(1235):21–53, 2017. doi:10.1017/aer.2016.94.

[120] F Afonso, J Vale, É Oliveira, F Lau, and A Suleman. Non-linear aeroelastic response of high aspect-ratio wings in the frequency domain. *The Aeronautical Journal*, 121(1240):858–876, 2017. doi:10.1017/aer.2017.29.

[121] Hermann J Hassig. An Approximate True Damping Solution of the Flutter Equation by Determinant Iteration. *Journal of Aircraft*, 8(11):885–889, 1971. doi:10.2514/3.44311.

[122] Richard H MacNeal. *The NASTRAN Theoretical Manual*, volume 221. Scientific and Technical Information Office, National Aeronautics and Space Agency, 1970.

[123] PC Chen, D Sarhaddi, and DD Liu. Transonic-Aerodynamic-Influence-Coefficient Approach for Aeroelastic and MDO Applications. *Journal of Aircraft*, 37(1): 85–94, 2000. doi:10.2514/2.2565.

[124] Jaroslaw Sobieszczanski-Sobieski and Raphael T Haftka. Multidisciplinary aerospace design optimization: survey of recent developments. *Structural optimization*, 14(1):1–23, 1997.

[125] Juan J. Alonso and Michael R. Colonno. Multidisciplinary Optimization with Applications to Sonic-Boom Minimization. *Annual Review of Fluid Mechanics*, 44(1):505–526, 2012. doi:10.1146/annurev-fluid-120710-101133.

[126] Joaquim R. R. A. Martins and John T. Hwang. Review and Unification of Methods for Computing Derivatives of Multidisciplinary Computational Models. *AIAA Journal*, 51(11):2582–2599, 2013. doi:10.2514/1.J052184.

[127] Athanasios Papageorgiou, Mehdi Tarkian, Kristian Amadori, and Johan Ölvander. Multidisciplinary design optimization of aerial vehicles: A review of recent advancements. *International Journal of Aerospace Engineering*, 2018: 1–21, 2018. doi:10.1155/2018/4258020.

[128] R. T. Haftka, J. Sobieszczanski-Sobieski, and S. L. Padula. On options for interdisciplinary analysis and design optimization. *Structural Optimization*, 4 (2):65–74, 1992. doi:10.1007/BF01759919.

[129] R Timothy Marler and Jasbir S Arora. Survey of multi-objective optimization methods for engineering. *Structural and multidisciplinary optimization*, 26(6): 369–395, 2004. doi:10.1007/s00158-003-0368-6.

[130] Graeme Kennedy and Joaquiem R R A Martins. A parallel aerostructural optimization framework for aircraft design studies. *Structural and Multidisciplinary Optimization*, 50:1079–1101, 2014. doi:10.1007/s00158-014-1108-9.

[131] Kai A. James, Graeme J. Kennedy, and Joaquim R.R.A. Martins. Concurrent aerostructural topology optimization of a wing box. *Computers & Structures*, 134:1–17, 2014. doi:10.1016/j.compstruc.2013.12.007.

[132] Timothy R. Brooks, Joaquim R.R.A. Martins, and Graeme J. Kennedy. High-fidelity aerostructural optimization of tow-steered composite wings. *Journal of Fluids and Structures*, 88:122–147, 2019. doi:10.1016/j.jfluidstructs.2019.04.005.

[133] Karthik Mani and Dimitri J. Mavriplis. Adjoint-Based Sensitivity Formulation for Fully Coupled Unsteady Aeroelasticity Problems. *AIAA Journal*, 47(8): 1902–1915, 2009. doi:10.2514/1.40582.

[134] Wrik Mallik, Rakesh K. Kapania, and Joseph A. Schetz. Effect of Flutter on the Multidisciplinary Design Optimization of Truss-Braced-Wing Aircraft. *Journal of Aircraft*, 52(6):1858–1872, 2015. doi:10.2514/1.C033096.

[135] P. C. Chen, Zhichao Zhang, and Eli Livne. Design-Oriented Computational Fluid Dynamics-Based Unsteady Aerodynamics for Flight-Vehicle Aeroelastic Shape Optimization. *AIAA Journal*, 53(12):3603–3619, 2015. doi:10.2514/1.J054024.

[136] Zhichao Zhang, P. C. Chen, Shuchi Yang, Zhicun Wang, and Qiqi Wang. Unsteady Aerostructure Coupled Adjoint Method for Flutter Suppression. *AIAA Journal*, 53(8):2121–2129, 2015. doi:10.2514/1.J053495.

[137] Anil Variyar, Thomas D. Economon, and Juan J. Alonso. Design and Optimization of Unconventional Aircraft Configurations with Aeroelastic Constraints. In *55th AIAA Aerospace Sciences Meeting*, Grapevine, TX, USA, January 2017. doi:10.2514/6.2017-0463.

[138] Manav Bhatia and Philip Beran. Design of Thermally Stressed Panels Subject to Transonic Flutter Constraints. *Journal of Aircraft*, 54(6):2340–2349, 2017. doi:10.2514/1.C034301.

[139] Robert E. Bartels and Bret K. Stanford. Aeroelastic Optimization with an Economical Transonic Flutter Constraint Using Navier–Stokes Aerodynamics. *Journal of Aircraft*, 55(4):1522–1530, 2018. doi:10.2514/1.C034675.

[140] Christopher A. Lupp and Carlos E. Cesnik. A Gradient-Based Flutter Constraint Including Geometrically Nonlinear Deformations. In *AIAA Scitech 2019 Forum*, San Diego, CA, USA, January 2019. doi:10.2514/6.2019-1212.

[141] Jinwu Xiang, Yongju Yan, and Daochun Li. Recent advance in nonlinear aeroelastic analysis and control of the aircraft. *Chinese journal of aeronautics*, 27(1):12–22, 2014. doi:10.1016/j.cja.2013.12.009.

[142] Didier Casner, Rémy Houssin, Jean Renaud, and Dominique Knittel. An Optimization-Based Embodiment Design Approach for Mechatronic Product Development. *The open automation and control systems journal*, 9(1), 2017. doi:10.2174/1874444301709010027.

[143] Gang Lei, Jianguo Zhu, Youguang Guo, Chengcheng Liu, and Bo Ma. A Review of Design Optimization Methods for Electrical Machines. *Energies*, 10(12):1962, 2017. doi:10.3390/en10121962.

[144] Junchen Yan, Osvaldo A Broesicke, Xin Tong, Dong Wang, Duo Li, and John C Crittenden. Multidisciplinary design optimization of distributed energy generation systems: The trade-offs between life cycle environmental and economic impacts. *Applied Energy*, 284:116197, 2021. doi:10.3390/en10121962.

[145] Philipp Geyer. Component-oriented decomposition for multidisciplinary design optimization in building design. *Advanced Engineering Informatics*, 23(1):12–31, 2009. doi:10.1016/j.aei.2008.06.008.

[146] Do-Hyoung Kim, Hyun-Gyung Kim, and Hak-Sung Kim. Design optimization and manufacture of hybrid glass/carbon fiber reinforced composite bumper beam for automobile vehicle. *Composite Structures*, 131:742–752, 2015. doi:10.1016/j.compstruct.2015.06.028.

[147] Saeed Azad and Michael J Alexander-Ramos. Robust Combined Design and Control Optimization of Hybrid-Electric Vehicles Using MDSDO. *IEEE Transactions on Vehicular Technology*, 2021. doi:10.1109/TVT.2021.3071863.

[148] Christian Pavese, Carlo Tibaldi, Frederik Zahle, and Taeseong Kim. Aeroelastic multidisciplinary design optimization of a swept wind turbine blade. *Wind Energy*, 20(12):1941–1953, 2017. doi:10.1002/we.2131.

[149] Michael K McWilliam, Thanasis K Barlas, Helge A Madsen, and Frederik Zahle. Aero-elastic wind turbine design with active flaps for AEP maximization. *Wind Energy Science*, 3(1):231–241, 2018. doi:10.5194/wes-3-231-2018.

[150] Justin S Gray, Charles A Mader, Gaetan KW Kenway, and Joaquim RRA Martins. Coupled Aeropropulsive Optimization of a Three-Dimensional Boundary-Layer Ingestion Propulsor Considering Inlet Distortion. *Journal of Aircraft*, 57 (6):1014–1025, 2020. doi:10.2514/1.C035845.

[151] Alessandro Sgueglia, Peter Schmollgruber, Nathalie Bartoli, Emmanuel Benard, Joseph Morlier, John Jasa, Joaquim R. R. A. Martins, John T. Hwang, and Justin S. Gray. Multidisciplinary design optimization framework with coupled

derivative computation for hybrid aircraft. *Journal of Aircraft*, 57(4):715–729, 2020.

[152] Guodong Chen and Krzysztof J. Fidkowski. Variable-fidelity multipoint aerodynamic shape optimization with output-based adapted meshes. *Aerospace Science and Technology*, 105:24, 2020. doi:10.1016/j.ast.2020.106004.

[153] Anand Amrit, Leifur Leifsson, and Slawomir Koziel. Fast Multi-Objective Aerodynamic Optimization Using Sequential Domain Patching and Multifidelity Models. *Journal of Aircraft*, 57(3):388–398, 2020. doi:10.2514/1.C035500.

[154] Odeh Dababneh and Timoleon Kipouros. Influence of high fidelity structural models on the predicted mass of aircraft wing using design optimization. *Aerospace Science and Technology*, 79:164–173, 2018. doi:10.1016/j.ast.2018.05.043.

[155] Raul Yondo, Esther Andrés, and Eusebio Valero. A review on design of experiments and surrogate models in aircraft real-time and many-query aerodynamic analyses. *Progress in Aerospace Sciences*, 96:23 – 61, 2018. doi:10.1016/j.paerosci.2017.11.003.

[156] Justin S. Gray, John T. Hwang, Joaquim R. R. A. Martins, Kenneth T. Moore, and Bret A. Naylor. OpenMDAO: an open-source framework for multidisciplinary design, analysis, and optimization. *Structural and Multidisciplinary Optimization*, 59(4):1075–1104, 2019. doi:10.1007/s00158-019-02211-z.

[157] Gaetan K. W. Kenway, Charles A. Mader, Ping He, and Joaquim R. R. A. Martins. Effective adjoint approaches for computational fluid dynamics. *Progress in Aerospace Sciences*, 110:100542, 2019. doi:10.1016/j.paerosci.2019.05.002.

[158] Songqing Shan and G Gary Wang. Survey of modeling and optimization strategies to solve high-dimensional design problems with computationally-expensive black-box functions. *Structural and multidisciplinary optimization*, 41(2):219–241, 2010. doi:10.1007/s00158-009-0420-2.

[159] Emiliano Iuliano and Esther Andrés Pérez. *Application of Surrogate-based Global Optimization to Aerodynamic Design*. Springer International Publishing, 2016. doi:10.1007/978-3-319-21506-8.

[160] Raphael T. Haftka, Diane Villanueva, and Anirban Chaudhuri. Parallel surrogate-assisted global optimization with expensive functions – a survey. *Structural and Multidisciplinary Optimization*, 54(1):3–13, 2016. doi:10.1007/s00158-016-1432-3.

[161] Nestor V. Queipo, Raphael T. Haftka, Wei Shyy, Tushar Goel, Rajkumar Vaidyanathan, and P. Kevin Tucker. Surrogate-based analysis and optimization. *Progress in Aerospace Sciences*, 41(1):1–28, 2005. ISSN 0376-0421. doi:10.1016/j.paerosci.2005.02.001.

[162] Alexander I. J. Forrester, András Sóbester, and Andy J. Keane. *Engineering Design via Surrogate Modelling*. John Wiley & Sons, Ltd, 2008. doi:10.1002/9780470770801.

[163] S. Ashwin Renganathan, Romit Maulik, and Jai Ahuja. Enhanced data efficiency using deep neural networks and Gaussian processes for aerodynamic design optimization. *Aerospace Science and Technology*, 111:106522, 2021. doi:10.1016/j.ast.2021.106522.

[164] Alexander I. J. Forrester and Andy J. Keane. Recent advances in surrogate-based optimization. *Progress in Aerospace Sciences*, 45(1):50–79, 2009. doi:10.1016/j.paerosci.2008.11.001.

[165] J. Laurenceau, M. Meaux, M. Montagnac, and P. Sagaut. Comparison of Gradient-Based and Gradient-Enhanced Response-Surface-Based Optimizers. *AIAA Journal*, 48(5):981–994, 2010. doi:10.2514/1.45331.

[166] Slawomir Koziel and Leifur Leifsson. Surrogate-based aerodynamic shape optimization by variable-resolution models. *AIAA Journal*, 51(1):94–106, 2013. doi:10.2514/1.J051583.

[167] Vishal Raul and Leifur Leifsson. Surrogate-based aerodynamic shape optimization for delaying airfoil dynamic stall using Kriging regression and infill criteria. *Aerospace Science and Technology*, 111:106555, 2021. doi:10.1016/j.ast.2021.106555.

[168] T. J. Mackman, C. B. Allen, M. Ghoreyshi, and K. J. Badcock. Comparison of Adaptive Sampling Methods for Generation of Surrogate Aerodynamic Models. *AIAA Journal*, 51(4):797–808, 2013. doi:10.2514/1.J051607.

[169] András Sóbester, Alexander I. J. Forrester, David J. J. Toal, Es Tresidder, and Simon Tucker. Engineering design applications of surrogate-assisted optimization techniques. *Optimization and Engineering*, 15:243–265, 2014. doi:10.1007/s11081-012-9199-x.

[170] J. Liu, W.-P. Song, Z.-H. Han, and Y. Zhang. Efficient aerodynamic shape optimization of transonic wings using a parallel infilling strategy and surrogate models. *Structural and Multidisciplinary Optimization*, 55:925–943, 2017. doi:10.1007/s00158-016-1546-7.

[171] Shawn E Gano, John E Renaud, Jay D Martin, and Timothy W Simpson. Update strategies for kriging models used in variable fidelity optimization. *Structural and Multidisciplinary Optimization*, 32(4):287–298, 2006. doi:10.1007/s00158-006-0025-y.

[172] Mohamed Amine Bouhlel, Nathalie Bartoli, Rommel G Regis, Abdelkader Otsmane, and Joseph Morlier. Efficient global optimization for high-dimensional constrained problems by using the Kriging models combined with the partial least squares method. *Engineering Optimization*, 50(12):2038–2053, 2018. doi:10.1080/0305215X.2017.1419344.

[173] T. Lefebvre, N. Bartoli, S. Dubreuil, M. Panzeri, R. Lombardi, P. Della Vecchia, L. Stingo, F. Nicolosi, A. De Marco, P.D. Ciampa, K. Anisimov, A. Savelyev, A. Mirzoyan, and A. Isyanov. Enhancing optimization capabilities using the AGILE collaborative MDO framework with application to wing and nacelle design. *Progress in Aerospace Sciences*, 119:100649, 2020. doi:10.1016/j.paerosci.2020.100649.

[174] Raymond H Myers, Douglas C Montgomery, and Christine M Anderson-Cook. *Response Surface Methodology: Process and Product Optimization using Designed Experiments*. John Wiley & Sons, 4 edition, 2016.

[175] M. D. Mckay, R. J. Beckman, and W. J. Conover. A Comparison of Three Methods for Selecting Values of Input Variables in the Analysis of Output From a Computer Code. *Technometrics*, 21(2):239–245, 1979. doi:10.1080/00401706.2000.10485979.

[176] Douglas C Montgomery. *Design and Analysis of Experiments*. John wiley & sons, 10 edition, 2017.

[177] Marco Evangelos Biancolini. *Fast Radial Basis Functions for Engineering Applications*. Springer, 2018. doi:10.1007/978-3-319-75011-8.

[178] TCS Rendall and CB Allen. Multi-dimensional aircraft surface pressure interpolation using radial basis functions. *Proceedings of the Institution of Mechanical Engineers, Part G: Journal of Aerospace Engineering*, 222(4):483–495, 2008. doi:10.1243/09544100JAERO263.

[179] Chunhua Sheng and Christian B Allen. Efficient Mesh Deformation using Radial Basis Functions on Unstructured Meshes. *AIAA journal*, 51(3):707–720, 2013. doi:10.2514/1.J052126.

[180] Marco Evangelos Biancolini, Andrea Chiappa, Ubaldo Cella, Emiliano Costa, Corrado Groth, and Stefano Porziani. Radial Basis Functions Mesh Morphing. In *International Conference on Computational Science*, pages 294–308. Springer, 2020. doi:10.1007/978-3-030-50433-5_23.

[181] Georges Matheron. Principles of Geostatistics. *Economic geology*, 58(8):1246–1266, 1963. doi:10.2113/gsecongeo.58.8.1246.

[182] Jerome Sacks, William J. Welch, Toby J. Mitchell, and Henry P. Wynn. Design and Analysis of Computer Experiments. *Statistical Science*, 4(4):409–423, 1989.

[183] Donald R Jones and Matthias Schonlau. Efficient Global Optimization of Expensive Black-Box Functions. *Journal of Global Optimization*, 13:455–492, 1998. doi:10.1023/A:1008306431147.

[184] Donald R Jones. A Taxonomy of Global Optimization Methods Based on Response Surfaces. *Journal of global optimization*, 21(4):345–383, 2001. doi:10.1023/A:1012771025575.

[185] Selvakumar Ulaganathan, Ivo Couckuyt, Tom Dhaene, Joris Degroote, and Eric Laermans. Performance study of gradient-enhanced Kriging. *Engineering with computers*, 32(1):15–34, 2016. doi:10.1007/s00366-015-0397-y.

[186] Mohamed A Bouhlel and Joaquim RRA Martins. Gradient-enhanced kriging for high-dimensional problems. *Engineering with Computers*, 35(1):157–173, 2019. doi:10.1007/s00366-018-0590-x.

[187] Tomislav Hengl, Gerard BM Heuvelink, and David G Rossiter. About regression-kriging: From equations to case studies. *Computers & geosciences*, 33(10): 1301–1315, 2007. doi:10.1016/j.cageo.2007.05.001.

[188] Mohamed Amine Bouhlel, Nathalie Bartoli, Abdelkader Otsmane, and Joseph Morlier. Improving kriging surrogates of high-dimensional design models by Partial Least Squares dimension reduction. *Structural and Multidisciplinary Optimization*, 53(5):935–952, 2016. doi:10.1007/s00158-015-1395-9.

[189] N. Bartoli, T. Lefebvre, S. Dubreuil, R. Olivanti, R. Priem, N. Bons, J. R. R. A. Martins, and J. Morlier. Adaptive modeling strategy for constrained global optimization with application to aerodynamic wing design. *Aerospace Science and Technology*, 90:85–102, 2019. doi:10.1016/j.ast.2019.03.041.

[190] S Timme, Simao Marques, and KJ Badcock. Transonic aeroelastic stability analysis using a Kriging-based Schur complement formulation. *AIAA journal*, 49(6):1202–1213, 2011. doi:10.2514/1.J050975.

[191] Markus P. Rumpfkeil and Philip Beran. Multi-fidelity surrogate models for flutter database generation. *Computers and Fluids*, 197:104372, 2020. doi:10.1016/j.compfluid.2019.104372.

[192] Sylvain Dubreuil, Nathalie Bartoli, Thierry Lefebvre, and Christian Gogu. Efficient global multidisciplinary optimization based on surrogate models. In *2018 multidisciplinary analysis and optimization conference*, page 3745, 2018. doi:10.2514/6.2018-3745.

[193] Florian Vesting, Rickard Gustafsson, and Rickard E Bensow. Development and application of optimisation algorithms for propeller design. *Ship Technology Research*, 63(1):50–69, 2016. doi:10.1080/09377255.2016.1145916.

[194] Vladimir Vapnik. *The Nature of Statistical Learning Theory*. Springer Verlag, 1995.

[195] Vladimir Vapnik. *Statistical Learning Theory*. John Wiley & Sons, 1998.

[196] Qing Wang, Weiqi Qian, and Kaifeng He. Unsteady aerodynamic modeling at high angles of attack using support vector machines. *Chinese Journal of Aeronautics*, 28(3):659–668, 2015. doi:10.1016/j.cja.2015.03.010.

[197] Esther Andrés-Pérez, Daniel González-Juárez, Mario J Martin-Burgos, Leopoldo Carro-Calvo, and Sancho Salcedo-Sanz. Influence of the number and location of design parameters in the aerodynamic shape optimization of a transonic aerofoil and a wing through evolutionary algorithms and support vector machines. *Engineering Optimization*, 49(2):181–198, 2017. doi:10.1080/0305215X.2016.1165568.

[198] Gang Chen, Yingtao Zuo, Jian Sun, and Yueming Li. Support-Vector-Machine-Based Reduced-Order Model for Limit Cycle Oscillation Prediction of Nonlinear Aeroelastic System. *Mathematical problems in engineering*, 2012, 2012. doi:10.1155/2012/152123.

[199] Keshi Zhang and Zhonghua Han. Support Vector Regression-based Multidisciplinary Design Optimization in Aircraft Conceptual Design. In *51st AIAA Aerospace Sciences Meeting including the New Horizons Forum and Aerospace Exposition*, page 1160, 2013. doi:10.2514/6.2013-1160.

[200] Mohamed Amine Bouhlel, Sicheng He, and Joaquim R. R. A. Martins. Scalable gradient–enhanced artificial neural networks for airfoil shape design in the subsonic and transonic regimes. *Structural and Multidisciplinary Optimization*, 61:1363–1376, 2020. doi:10.1007/s00158-020-02488-5.

[201] Xinshuai Zhang, Fangfang Xie, Tingwei Ji, Zaoxu Zhu, and Yao Zheng. Multi-fidelity deep neural network surrogate model for aerodynamic shape optimization. *Computer Methods in Applied Mechanics and Engineering*, 373:113485, 2021. doi:10.1016/j.cma.2020.113485.

[202] Wei Chen, Kevin Chiu, and Mark D. Fuge. Airfoil Design Parameterization and Optimization Using Bézier Generative Adversarial Networks. *AIAA Journal*, 58 (11):4723–4735, 2020. doi:10.2514/1.J059317.

[203] Jichao Li and Mengqi Zhang. On deep-learning-based geometric filtering in aerodynamic shape optimization. *Aerospace Science and Technology*, 112:106603, 2021. ISSN 1270-9638. doi:10.1016/j.ast.2021.106603.

[204] Xiaosong Du, Ping He, and Joaquim R.R.A. Martins. Rapid airfoil design optimization via neural networks-based parameterization and surrogate modeling. *Aerospace Science and Technology*, 113:106701, 2021. doi:10.1016/j.ast.2021.106701.

[205] Jun Tao and Gang Sun. Application of deep learning based multi-fidelity surrogate model to robust aerodynamic design optimization. *Aerospace Science and Technology*, 92:722–737, 2019. doi:10.1016/j.ast.2019.07.002.

[206] Douglas Allaire and Karen Willcox. A Mathematical and Computational Framework for Multifidelity Design and Analysis with Computer Models. *International Journal for Uncertainty Quantification*, 4(1), 2014. doi:10.1615/Int.J.UncertaintyQuantification.2013004121.

[207] M Giselle Fernández-Godino, Chanyoung Park, Nam-Ho Kim, and Raphael T Haftka. Review of multi-fidelity models. *arXiv preprint arXiv:1609.07196*, 2016. doi:10.2514/1.J057750.

[208] Leo WT Ng and Karen E Willcox. Multifidelity approaches for optimization under uncertainty. *International Journal for numerical methods in Engineering*, 100(10):746–772, 2014. doi:10.1002/nme.4761.

[209] Leifur Leifsson and Slawomir Koziel. Aerodynamic shape optimization by variable-fidelity computational fluid dynamics models: A review of recent progress. *Journal of Computational Science*, 10:45–54, 2015. doi:10.1016/j.jocs.2015.01.003.

[210] Spyridon G. Kontogiannis, Jean Demange, A. Mark Savill, and Timoleon Kipouros. A comparison study of two multifidelity methods for aerodynamic optimization. *Aerospace Science and Technology*, 97:105592, 2020. doi:10.1016/j.ast.2019.105592.

[211] Mengmeng Zhang, Nathalie Bartoli, Aidan Jungo, Wim Lammen, Erik Baalbergen, and Mark Voskuijl. Enhancing the handling qualities analysis by collaborative aerodynamics surrogate modelling and aero-data fusion. *Progress in Aerospace Sciences*, 119:100647, 2020. doi:10.1016/j.paerosci.2020.100647.

[212] Steven L. Brunton, Bernd R. Noack, and Petros Koumoutsakos. Machine learning for fluid mechanics. *Annual Review of Fluid Mechanics*, 52(1):477–508, 2020. doi:10.1146/annurev-fluid-010719-060214.

[213] Donald E Myers. Matrix Formulation of Co-Kriging. *Journal of the International Association for Mathematical Geology*, 14(3):249–257, 1982. doi:10.1007/BF01032887.

[214] A. J. Booker, P. D. Frank J. E. Dennis Jr., D. B. Serafini, V. Torczon, and M. W. Trosset. A rigorous framework for optimization of expensive functions by surrogates. *Structural and Multidisciplinary Optimization*, 17:1–13, 1999. doi:10.1007/BF01197708.

[215] Bobak Shahriari, Kevin Swersky, Ziyu Wang, Ryan P Adams, and Nando De Freitas. Taking the human out of the loop: A review of Bayesian optimization. *Proceedings of the IEEE*, 104(1):148–175, 2015. doi:10.1109/JPROC.2015.2494218.

[216] Alan G Watson and Randal J Barnes. Infill Sampling Criteria to Locate Extremes. *Mathematical Geology*, 27(5):589–608, 1995. doi:10.1007/BF02093902.

[217] Michael J. Sasena, Panos Papalambros, and Pierre Goovaerts. Exploration of Metamodeling Sampling Criteria for Constrained Global Optimization. *Engineering Optimization*, 34(3):263–278, 2002. doi:10.1080/03052150211751. Number: 3.

[218] András Sóbester, Stephen J. Leary, and Andy J. Keane. On the Design of Optimization Strategies Based on Global Response Surface Approximation Models. *Journal of Global Optimization*, 33(1):31–59, 2005. doi:10.1007/s10898-004-6733-1.

[219] Shishi Chen, Zhen Jiang, Shuxing Yang, and Wei Chen. Multimodel Fusion Based Sequential Optimization. *AIAA Journal*, 55(1):241–254, 2017. doi:10.2514/1.J054729.

[220] Andrea Da Ronch, Marco Panzeri, M Anas Abd Bari, Roberto d'Ippolito, and Matteo Franciolini. Adaptive design of experiments for efficient and accurate estimation of aerodynamic loads. *Aircraft Engineering and Aerospace Technology*, 2017. doi:10.1108/AEAT-10-2016-0173.

[221] M. T.N. Emmerich, K. C. Giannakoglou, and B. Naujoks. Single- and Multiobjective Evolutionary Optimization Assisted by Gaussian Random Field Metamodels. *IEEE Transactions on Evolutionary Computation*, 10(4):421–439, 2006. doi:10.1109/TEVC.2005.859463.

[222] Xiaojun Wang, Bowen Ni, Linxi Zeng, and Yisi Liu. An adaptive sampling strategy for construction of surrogate aerodynamic model. *Aerospace Science and Technology*, 112:106594, 2021. doi:10.1016/j.ast.2021.106594.

[223] Anirban Chaudhuri and Raphael T Haftka. Effectiveness Indicators for Stopping Criteria Based on Minimum Required Improvement. In *56th AIAA/ASCE/AHS/ASC Structures, Structural Dynamics, and Materials Conference*, page 0901, 2015. doi:10.2514/6.2015-0901.

[224] Charles Audet, J. Denni, Douglas Moore, Andrew Booker, and Paul Frank. A Surrogate-Model-Based Method for Constrained Optimization. In *8th Symposium on Multidisciplinary Analysis and Optimization*. American Institute of Aeronautics and Astronautics, 2000. doi:10.2514/6.2000-4891.

[225] Jesús Martínez-Frutos and David Herrero-Pérez. Kriging-based infill sampling criterion for constraint handling in multi-objective optimization. *Journal of Global Optimization*, 64(1):97–115, 2016. doi:10.1007/s10898-015-0370-8.

[226] Rémy Priem, Nathalie Bartoli, and Youssef Diouane. On the use of upper trust bounds in constrained Bayesian optimization infill criteria. In *AIAA aviation 2019 forum*, page 2986, 2019. doi:10.2514/6.2019-2986.

[227] R. Priem, N. Bartoli, Y. Diouane, and A. Sgueglia. Upper trust bound feasibility criterion for mixed constrained Bayesian optimization with application to aircraft design. *Aerospace Science and Technology*, 105:105980, 2020. doi:10.1016/j.ast.2020.105980.

[228] Shixin Cheng, Hao Zhan, Zhaoxin Shu, Huayu Fan, and Ban Wang. Effective optimization on Bump inlet using meta-model multi-objective particle swarm assisted by expected hyper-volume improvement. *Aerospace Science and Technology*, 87:431–447, 2019. doi:10.1016/j.ast.2019.02.039.

[229] Martin Sohst, Frederico Afonso, and Afzal Suleman. Surrogate-based optimization based on the probability of feasibility. *Structural and Multidisciplinary Optimization*, 65(1):1–17, 2022. doi:10.1007/s00158-021-03134-4.

[230] José Lobo do Vale, Martin Sohst, Curran Crawford, Afzal Suleman, Graham Potter, and Sid Banerjee. On the Multi-fidelity Approach in Surrogate-based MDO of HARW aircraft. *Aeronautical Journal*, 2021. *under revision*.

[231] M Sohst, J Lobo do Vale, F Afonso, and A Suleman. Optimization and comparison of strut-braced and high aspect ratio wing aircraft configurations including

flutter analysis with geometric non-linearities. *Aerospace Science and Technology*, 2022. submitted.

[232] Tiago Jesus, Martin Sohst, José Lobo do Vale, and Afzal Suleman. Surrogate based MDO of a canard configuration aircraft. *Structural and Multidisciplinary Optimization*, pages 1–25, 2021. doi:10.1007/s00158-021-03051-6.

[233] C. Ribeiro, F. Afonso, M. Sohst, and A. Suleman. Surrogate-based Multidisciplinary Design Optimization on an UAM-VTOL Aircraft for Energy Minimization. In André C. Marta and Afzal Suleman, editors, *Proceedings of the International Conference on Multidisciplinary Design Optimization of Aerospace Systems (AEROBEST 2021)*, pages 1–758, Instituto Superior Técnico, Universidade de Lisboa, Portugal, July 2021. IDMEC. ISBN:978-989-99424-8-6.

[234] Martin Sohst, Jose Vale, Curran Crawford, Graham Potter, and Sid Banerjee. A framework for multi-fidelity multi-disciplinary kriging-based surrogate model optimization of novel aircraft configurations. In *NATO STO AVT 324 - Meeting Proceedings Paper*, 2020.

[235] D. E. Calderon, J. E. Cooper, M. Lowenberg, S. A. Neild, and E. B. Coetzee. Sizing High-Aspect-Ratio Wings with a Geometrically Nonlinear Beam Model. *Journal of Aircraft*, 56(4):1455–1470, 2019. doi:10.2514/1.C035296. URL `https://doi.org/10.2514/1.C035296`.

[236] Junuthula Narasimha Reddy. *Introduction to the Finite Element Method*. McGraw-Hill Education, 4 edition, 2019.

[237] Sang Truong Ha, Long Cu Ngo, Muhammad Saeed, Byoung Jin Jeon, and Hyounggwon Choi. A comparative study between partitioned and monolithic methods for the problems with 3D fluid-structure interaction of blood vessels. *Journal of Mechanical Science and Technology*, 31(1):281–287, 2017. doi:10.1007/s12206-016-1230-2.

[238] Siemens Digital Industries Software. Simcenter STAR-CCM+, version 12.02.011 R8, 2012.

[239] T.D. Economon, F. Palacios, S.R. Copeland, T.W. Lukaczyk, and J.J. Alonso. Su2: an open-source suite for multiphysics simulation and design. *AIAA Journal*, 54(3):828–846, 2016. doi:10.2514/1.J053813.

[240] Florian R Menter. Two-Equation Eddy-Viscosity Turbulence Models for Engineering Applications. *AIAA journal*, 32(8):1598–1605, 1994. doi:10.2514/3.12149.

[241] Edward Albano and William P Rodden. A Doublet-Lattice Method for Calculating Lift Distributions on Oscillating Surfaces in Subsonic Flows. *AIAA journal*, 7(2):279–285, 1969. doi:10.2514/3.5086.

[242] AGARD. Experimental data base for computer program assessment. Technical Report 9283513231, North Atlantic Treaty Organization, 1979.

[243] Eligius MT Hendrix, G Boglárka, et al. *Introduction to Nonlinear and Global Optimization*, volume 37. Springer, 2010. doi:10.1007/978-0-387-88670-1.

[244] Søren Nymand Lophaven, Hans Bruun Nielsen, and Jacob Søndergaard. *Aspects of The MATLAB Toolbox DACE*. Informatics and Mathematical Modelling, Technical University of Denmark, DTU, 2002.

[245] Mohamed Amine Bouhlel, John T Hwang, Nathalie Bartoli, Rémi Lafage, Joseph Morlier, and Joaquim RRA Martins. A Python surrogate modeling framework with derivatives. *Advances in Engineering Software*, 135:102662, 2019. doi:10.1016/j.advengsoft.2019.03.005.

[246] Jay D Martin and Timothy W Simpson. Use of Kriging Models to Approximate Deterministic Computer Models. *AIAA journal*, 43(4):853–863, 2005. doi:10.2514/1.8650.

[247] Benjamin Rosenbaum and Volker Schulz. Comparing sampling strategies for aerodynamic Kriging surrogate models, 2012.

[248] Henri Theil. *Principles of Econometrics*. John Wiley, New York, 1971.

[249] Michael J. Sasena. *Flexibility and Efficiency Enhancements for Constrained Global Design Optimization with Kriging Approximations*. Phd thesis, University of Michigan, 2002.

[250] James M Parr, Andy J Keane, Alexander IJ Forrester, and Carren ME Holden. Infill sampling criteria for surrogate-based optimization with constraint handling. *Engineering Optimization*, 44(10):1147–1166, 2012. doi:10.1080/0305215X.2011.637556.

[251] Rémi Lam, Douglas L Allaire, and Karen E Willcox. Multifidelity Optimization using Statistical Surrogate Modeling for Non-Hierarchical Information Sources. In *56th AIAA/ASCE/AHS/ASC Structures, Structural Dynamics, and Materials Conference*, page 0143, 2015. doi:10.2514/6.2015-0143.

[252] Robert Hooke and Terry A Jeeves. "Direct Search" Solution of Numerical and Statistical Problems. *Journal of the ACM (JACM)*, 8(2):212–229, 1961. doi:10.1145/321062.321069.

[253] Richard H Byrd, Mary E Hribar, and Jorge Nocedal. An Interior Point Algorithm for Large-Scale Nonlinear Programming. *SIAM Journal on Optimization*, 9(4): 877–900, 1999. doi:10.1137/S1052623497325107.

[254] Richard H Byrd, Jean Charles Gilbert, and Jorge Nocedal. A trust region method based on interior point techniques for nonlinear programming. *Mathematical programming*, 89(1):149–185, 2000. doi:10.1007/PL00011391.

[255] David E Goldberg. *Genetic Algorithms in Search, Optimization, and Machine Learning*. Addison-Wesley, 1989.

[256] P. B. Thanedar and G. N. Vanderplaats. Survey of Discrete Variable Optimization for Structural Design. *Journal of Structural Engineering*, 121(2):301–306, 1995. doi:10.1061/(ASCE)0733-9445(1995)121:2(301).

[257] Huachao Dong, Baowei Song, Zuomin Dong, and Peng Wang. SCGOSR: Surrogate-based constrained global optimization using space reduction. *Applied Soft Computing*, 65:462–477, 2018. doi:10.1016/j.asoc.2018.01.041.

[258] Isaac Gibert Martínez, Frederico Afonso, Simão Rodrigues, and Fernando Lau. A Sequential Approach for Aerodynamic Shape Optimization with Topology Optimization of Airfoils. *Mathematical and Computational Applications*, 26(2): 34, 2021. doi:10.3390/mca26020034.

[259] H. Lomax, Thomas H. Pulliam, and David W. Zingg. *Fundamentals of Computational Fluid Dynamics*. Springer-Verlag Berlin Heidelberg, 2001. doi:10.1007/978-3-662-04654-8.

[260] Brenda Kulfan and John Bussoletti. "Fundamental" Parameteric Geometry Representations for Aircraft Component Shapes. In *11th AIAA/ISSMO Multi-*

disciplinary Analysis and Optimization Conference, Portsmouth, Virginia, USA, September 2006. doi:10.2514/6.2006-6948.

[261] Brenda M. Kulfan. Universal Parametric Geometry Representation Method. *Journal of Aircraft*, 45(1):142–158, 2008. doi:10.2514/1.29958.

[262] P Piperni, M Abdo, F Kafyeke, and Askin T Isikveren. Preliminary Aerostructural Optimization of a Large Business Jet. *Journal of Aircraft*, 44(5):1422–1438, 2007. doi:10.2514/1.26989.

[263] Nicholas A Meadows, Joseph A Schetz, Rakesh K Kapania, Manav Bhatia, and Guclu Seber. Multidisciplinary Design Optimization of Medium-Range Transonic Truss-Braced Wing Transport Aircraft. *Journal of Aircraft*, 49(6): 1844–1856, 2012. doi:10.2514/1.C031695.

[264] Rikin Gupta, Wrik Mallik, Rakesh K Kapania, and Joseph A Schetz. Multidisciplinary Design Optimization of Subsonic Strut-Braced Wing Aircraft. In *52nd Aerospace Sciences Meeting*, page 0186, 2014. doi:10.2514/6.2014-0186.

[265] Norberto Goizueta, Ariel Drachinsky, Andrew Wynn, Daniella E Raveh, and Rafael Palacios. Flutter predictions for very flexible wing wind tunnel test. In *AIAA Scitech 2021 Forum*, page 1711, 2021. doi:10.2514/6.2021-1711.